STENTED ARTERY BIOMECHANICS: A COMPUTATIONAL AND IN VIVO ANALYSIS OF STENT DESIGN AND PATHOBIOLOGICAL RESPONSE

A Dissertation

by

LUCAS HOWARD TIMMINS

Submitted to the Office of Graduate Studies of
Texas A&M University
in partial fulfillment of the requirements for the degree of

DOCTOR OF PHILOSOPHY

May 2010

Major Subject: Biomedical Engineering

STENTED ARTERY BIOMECHANICS: A COMPUTATIONAL AND IN VIVO ANALYSIS OF STENT DESIGN AND PATHOBIOLOGICAL RESPONSE

A Dissertation

by

LUCAS HOWARD TIMMINS

Submitted to the Office of Graduate Studies of
Texas A&M University
in partial fulfillment of the requirements for the degree of

DOCTOR OF PHILOSOPHY

Approved by:

Chair of Committee,	James E. Moore, Jr.
Committee Members,	Fred J. Clubb, Jr.
	Stephen E. Greenwald
	Jay D. Humphrey
	Duncan J. Maitland
	Matthew W. Miller
Head of Department,	Gerard L. Coté

May 2010

Major Subject: Biomedical Engineering

ABSTRACT

Stented Artery Biomechanics: A Computational and In Vivo Analysis of Stent Design and Pathobiological Response. (May 2010)

Lucas Howard Timmins, B.S., Texas A&M University

Chair of Advisory Committee: Dr. James E. Moore, Jr.

Vascular stents have become a standard for treating atherosclerosis due to distinct advantages in trauma and cost with other surgical techniques. Unfortunately, the therapy is hindered by the risk of a new blockage (termed restenosis) developing in the treated artery. Clinical studies have indicated that stent design is a major risk factor for restenosis, with failure rates varying from 20 to 40% for bare metal stents. Subsequently, there has been a significant effort devoted to reducing failure rates by covering stents in polymer coatings in which anti-proliferative drugs are embedded, however complications have arisen (e.g. incomplete endothelization, lack of success in peripheral arteries, lack of long-term follow-up studies) that have limited the success of this technology. It has been thought that restenosis is directly related to the mechanical conditions that vascular stents create. Moreover, it has been hypothesized that stents that induce higher non-physiologic stresses result in a more aggressive pathobiological response that can lead to restenosis development.

In this study, a combination of computational modeling and in vivo analysis were conducted to investigate the artery stent-induced wall stresses, and subsequent biological

inflammatory response. In particular, variations in stent design were investigated as a means of examining specific stent design criteria that minimize the mechanical impact of stenting. Collectively, these data indicate that stent designs that subject the artery wall to higher stress values result in significantly more neointimal tissue proliferation, therefore, confirming the aforementioned hypothesis. Moreover, this work provides valuable insight into the role that biomechanics can play in improving the success rate of this percutaneous therapy and overall patient care.

DEDICATION

To my late Grandfather, William H. Hall, who instilled in me the diligence required to complete this work.

ACKNOWLEDGEMENTS

First, and foremost, I would like to thank my family for the continued support, encouragement, and understanding they have provided me the past years as I pursued degrees in high education. I would especially like to thank my sister, Lindsey, for the inspiration and example she set in obtaining a post-graduate degree.

It is with great pleasure that I acknowledge my advisor, scientific mentor, and dear friend, Dr. James E. Moore, Jr. The professional guidance, endless wisdom, relentless commitment, and continual drive he provided have allowed me to grow both professionally and personally. He consistently entrusted me with my scientific development, and without so, the work presented herein would not have been possible. It was an honor and privilege to work for and with Dr. Moore. I also owe a special thank you to his wife, Peggy, for allowing me to be a part of her "extended family" during my time in College Station.

I also owe my sincerest thanks to my "surrogate" advisor, scientific mentor, and great friend Professor Stephen E. Greenwald at Barts and The London Medical School. He allowed me to work in his laboratory, learning valuable skills and techniques that will have lasting effects on my future research endeavors. Above all, he taught me the true fundamentals of experimental research. It was a true pleasure to have the opportunity to not only train under, but also work alongside a scientist of Prof. Greenwald's caliber.

I want to thank and acknowledge each of my committee members (Dr. Fred J. Clubb, Jr., Dr. Jay D. Humphrey, Dr. Duncan J. Maitland, and Dr. Matthew W. Miller) for their guidance, support, and critical insight on the work present herein. In particular, I would like to acknowledge the significant contributions of Dr. Clubb towards my understanding of cardiovascular pathology. It was a pleasure to have the opportunity to train under him, and I have an immense amount of respect for his commitment to motivate, educate, and mentor students of all disciplines.

I would like to recognize several of my collaborators and manuscript co-authors that have provided assistance in my research endeavors, thoughtful insight, and continual understanding of the field. I would like to thank Dr. John C. Criscione who first introduced me to cardiovascular mechanics and continues to expand my knowledge and appreciation of nonlinear solid mechanics. Also, I would like to acknowledge Professor Alexander Rachev at the Georgia Institute of Technology for his intriguing and enlightening discussions of solid mechanics, and for his role in introducing Drs. Moore and Greenwald. I also owe a great deal of appreciation to Dr. Alvin T. Yeh for educating me on the theory and application of nonlinear optical microscopy. Also, I would like to acknowledge Dr. Qiaofeng ("Chow-fung") Wu for his technical assistance and numerous discussions about nonlinear optical microscopy. Finally, I owe a tremendous amount of gratitude to Dr. Michael R. Moreno as a mentor, former lab mate, and great friend, who continues to inspire and instruct me in the diverse areas of research, philosophy, music, and, most importantly, life.

I am also indebted to my past and current peers that I have had the great pleasure of working/collaborating with, learning from, and continually distracting during my graduate work. These people include: Julian Bedoya, Christopher Evagora, Dr. Andrew Hubball, Dr. Clark Meyer, Dr. Daisuke Mori, Andrew Peters, Dr. João Silva Soares, Elaheh Rahbar, William Richardson, and Shiva Yazdani-Beioky.

Finally, I would like to thank those who have accompanied, mentored, and/or inspired me in the art of music these past years. In no particular order: Jimmy M., Mike M., Chris B., Eric C., Jason H., Clark M., Caroline C., Jimi H., Ryan P., Holly G., Brian G., Eric J., Louie M., Joel B., Alan E., Stevie R.V., Clark H., Danny B., and Joe S.

TABLE OF CONTENTS

CHAPTER Page

LIST OF FIGURES

FIGURE Page

LIST OF TABLES

CHAPTER I

INTRODUCTION: ATHEROSCLEROSIS AND A HISTORICAL REVIEW OF INTERVENTIONAL CARDIOLOGY

Atherosclerosis

Atherosclerosis is a specific form of arteriosclerosis that results in pathologic thickening of the intimal layer. While most commonly treated in the coronary arteries, atherosclerosis occurs in other, very specific large and medium sized arteries of the vasculature (e.g. abdominal aorta, renal, iliac, and carotid arteries). It is characterized by a complex interaction of cells both in the blood and artery wall and molecular messengers, that ultimately leads to reduction in blood flow to tissues distal to the occlusion.

Generally speaking, atherosclerosis is an inflammatory disease that affects the arterial walls. It can begin as early as childhood with the formation of "fatty-streaks"; however, it does not usually show clinical manifestations until well into adulthood. The formation of an atherosclerotic lesion results from disruption of the normal function of the endothelium. This alteration is largely governed by the local hemodynamics, and in particular low and oscillatory wall shear stress. Such flow disturbances result in increased levels of adhesive molecules [e.g. vascular-cell adhesion molecule-1, intercellular adhesion molecule-1, E-selectin; [1]], increased vascular permeability [2], and possible exposure of underlying,

---

This dissertation follows the style of ASME Journal of Biomechanical Engineering.

highly thrombogenic vascular constituents to the flowing blood. Collectively, these endothelial modifications can result in the adhesion and transmigration of blood borne monocytes and T lymphocytes, modification and infiltration of low-density lipoproteins (LDL) into the arterial wall, and platelet aggregation and mural thrombus formation, respectively, all of which are ubiquitous in the progression to advanced of atherosclerosis. Together, these cellular and molecular events lead to the migration and proliferation of macrophages and vascular smooth muscle cells, and the formation of the advanced lesion.

Atherosclerotic lesions are considered advanced by histological standards when large accumulations of cells, lipids, extracellular matrix proteins, and possibly minerals are present, there is disruption in the organizational and structural integrity of the arterial wall, and, most notably, there is local thickening of the intimal layer. Lesions are classified based on characteristic components and pathogenic mechanisms. The Committee on Vascular Lesions of the American Heart Association's Council on Arteriosclerosis has denoted six classifications [types I-VI; [3, 4]]. Types I – III are focal, relatively small lesions that represent the precursors of the more advanced, clinically significant plaques. Type I lesions consist of isolated groups of macrophages, some of which contain small intracellular lipid droplets, that may not be visible to the unaided eye. As these lesions further develop as a result of additional macrophage aggregation, yellow or "fatty" streaks may form that are comprised of lipid-laden macrophages (termed foam cells) and small numbers of vascular smooth muscles cells (VSMC) containing lipid vesicles. Such lesions are classified as type II and can either further progress (type IIa) or can become progression resistant (type IIb). The deciding factor in the fate of type II lesions is thought to be the local hemodynamics [3].

Type III lesions are the transition lesion, both chemically and morphologically, between clinically insignificant lesions and advanced atherosclerotic plaques. In particular, type III lesions are characterized by focal adaptive intimal thickening, and most notably under histological evaluation, extracellular pools of lipid-laden material among VSMC layers.

Advanced atherosclerotic lesions (types IV – VI) differ from the smaller lesions, in that they are characterized by extreme disorganization of the intimal layer leading to negative remodeling (i.e. a reduction in lumen size) and clinical complications. Type IV lesions, known as atheromas, are characterized by an eccentric aggregation of extracellular lipid pools to form the lipid core. These lipids are derived from the localization of plasma lipids in atherosclerotic-prone regions, and the migration of these lipids through the, now, highly permeable endothelial cell layer. On the periphery of the lipid core are dense concentrations of macrophages, foam cells, and lymphocyte, as well as small neovascular buds. As the lipid core further develops, an increase of fibrous tissue (largely collagen) will cover the surface (fibrous cap), and this lesion will be labeled as a type V. The lesion are labeled fibrous plaques (type Va) or, if calcification occurs, are classified as type Vb. Regardless of the subtype, type V lesions are multi-layered and are rich in collagen and VSMC, have microhemorrhages present, and show a substantial intrusion into the luminal space. Type VI lesions are largely catastrophic, and are classified by disruption of the fibrous cap leading to hematoma formation and/ or thrombotic deposits. While each of the lesion discussed (types I – VI) are identifiable under various histological techniques, the fact that some lesions show no clinical symptoms or that some lesser developed lesions can be fatal

while more advanced lesions may never be symptomatic, has led to the development of noninvasive markers to better diagnosis the presence and progression of the disease.

Each year, the American Heart Association publishes their annual statistical report on cardiovascular diseases (CVD), and continually atherosclerosis ranks as one of, if not the leading cause of deaths each year. In 2009, it was reported that CVD accounted for approximately 34% of all death in the United States [~830,000; [5]]. Specifically coronary heart disease (CHD) accounted for approximately 52% of all CVD deaths, stroke 17%, and other diseases of the arteries (e.g. aneurysms) 4%; all of these diseases are largely a result of atherosclerosis. Furthermore, health care cost for CHD alone in 2009, were estimated at approximately $165 billion. Nevertheless, there is a still pressing need for the continual development and improvement of treatment modalities to improve patient outcomes.

The History of Cardiac Catheterization, Angioplasty, and Vascular Stenting

The treatment of cardiovascular diseases, in particular flow-limiting forms, has been revolutionized by development and advancement of catheter-based interventions. These techniques have not only allowed for accurate diagnosis and effective treatment for essentially all CVD, but also a better physiological understanding of the cardiovascular system. While catheterizations are reported to have been performed by the Egyptians (3000 B.C.), the first documented catheterization of the cardiovascular system was performed by Stephen Hales in 1711 [6]. Hale conducted the direct catheterization as a means of examining the ventricular pressures in a horse. His experimental set-up included brass pipes that were inserted into the right and left ventricles through catheterization of the venous and

arterial system, respectively, that were then attached to long glass tubes via the flexible trachea of geese. The advent and development of cardiac catheterization has led to numerous fundamental findings and advancements; however, in terms of treating CVD, it has led to the development of angioplasty.

Charles T. Dotter, a vascular radiologist at the University of Oregon, serendipitously discovered angioplasty during a routine abdominal aortagram [7]. During retrograde access via a femoral cutdown, Dotter inadvertently recanalized an occluded right iliac by essentially forcing a guide wire through the atherosclerotic plaque. Realizing the potential of this technique, Dotter soon developed balloon-mounted dilating catheters and perfected his technique on cadavers. It was in January 1964 that Dotter along with his resident, Melvin P. Judkins, performed the first interventional angioplasty (termed the "Dotter technique") on a patient who had an occluded left popliteal artery [8]. In contrast to the current balloon inflation angioplasty technique, Dotter and Judkins passed a 0.05" OD guide-wire under fluoroscopy transversely across the occlusion, and subsequently passed a 0.1" OD, followed by a 0.2" OD, Teflon catheter across the lesion site. Dotter, however, saw the need for a more sophisticated technique, as the application of large shear forces to bore through the plaque could cause unnecessary injury. It is interesting to note that Dotter and Judkins envisioned the need for a "lumen-to-lumen transathermatous" bridge or "endovascular splint" to treat occlusion peripheral artery disease. While Dotter did not receive recognition for his work for nearly 15 years due to his nonconventional persona, he was considerably well ahead of his time and his development of interventional cardiology and significant contributions to the field have saved millions of lives.

Following Dotter's pioneering work in the development of angioplasty in the peripheral arteries, application of the technique to the coronary vasculature was of pressing need. While the first arteriogram was performed in 1919 by the Argentine radiologist Carlos Heuser [9], the need for a technique to properly image the coronary arteries was not developed for almost four decades. It was not until 1958 that the pediatric cardiologist F. Mason Sones performed the first human cineangiography of the coronary arteries. Like Dotter's discovery, it was by accident, during a routine left ventriculogram. This seminal technique led to the development of numerous catheter systems, including the common *J*-shaped safety guide-wire, to better access the coronary ostia, thus allowing for the advancements of catheter-based coronary interventional techniques.

Andreas Grüntzig, a young German trained in epidemiology, social medicine, and internal medicine, learned the "Dotter technique" in 1969, while spending time as a guest fellow in the radiology department at the Aggertaclinic in Engelskirchen, Germany [7]. Following a relocation to University Hospital in Zurich, Switzerland and numerous recanalizations using Dotter's methods, Grüntzig began constructing his own prototype balloons and attaching them to the ends of Dotter catheters. In contrast to previous angioplasty balloons-catheter systems, Grüntzig made the balloons out of polyvinyl chloride, a much tougher material that could withstand the high inflation pressures, and he eventually developed a double-lumen catheter. The second lumen allowed for injection of contrast media, in addition to pressure monitoring to ensure adequate dilation of the stenosis. After numerous successful animal and cadaver studies [7], Grüntzig and Richard K. Myler performed the first human coronary angioplasty in May 1977 at St. Mary's Hospital in San

Francisco, CA [10]. The procedure, however, was performed intraoperatively during coronary bypass surgery via arteriotomy of the left anterior descending (LAD) coronary artery. Within months, Grüntzig returned to Zurich and had performed the first coronary angioplasty in an awake human on September 1977 [11]. The procedure was performed on a 37 year old male, who had an obstruction of his proximal LAD. It is interesting to note that this patient was examined 10 years later, with no reoccurrence of a new blockage [7].

Clinicians soon recognized the mechanical implications of angioplasty. It was first thought that that technique was a gentle, controlled procedure that involved a uniform compression of the soft and compressible plaque constituents. However, Kurt Amplatz and colleagues [12] promptly noted that angioplasty was a "violent, somewhat unpredictable assault" on the occluded artery that included plaque splitting, intimal dissection, and excessive arterial stretching. Such findings explained the complications that were soon observed following the widespread use of coronary angioplasty. In particular, the abrupt closure following the intervention as a result of the elastic recoil of the artery, and, still to this day, unwarranted proliferation of neointimal tissue leading to the development of a new blockage (termed restenosis). As Dotter and Judkins had suggested [8], there was a need for an endovascular prosthesis that remained expanded and in place to ensure arterial patency following deflation and retraction of the balloon catheter.

It was not long after the Dotter and Judkins pioneering work in angioplasty that the development of what would become the modern version of vascular stenting was reported. In fact, Dotter himself published the first experimental findings of the placement and long-term patency of "prosthetic grafts" in the peripheral arteries of canines [13]. The cylindrical

scaffolds were constructed of polyethylene, polyamide, Silastic, Teflon, or stainless steel. Following arterial access through the carotid arteries, these scaffolds were inserted using the method that Dotter developed for angioplasty in healthy femoral or popliteal arteries. Mixed results were noted, as immediate thrombosis development most often occurred; however, administration of anticoagulants (Heparin) and insertion of stainless steel coiled springs showed patency for longer than two years. As with the development and progression of angioplasty, Dotter discussed the potential of this interventional technique, noting it as a means of "freedom from the trauma usually associated with surgical vascular reconstruction."

Experimental work with endovascular devices to treat atherosclerotic lesions continued for over two decades, however results were still plagued by acute thrombosis and stent migration. Furthermore, the technique, at least during prior to Grüntzig's work, was not widely accepted by vascular surgeons [14]. Early prototype devices included Dotter's experimental placement of nitinol coils in 1983 [15], spiral and double-helix stainless steel springs implanted by D. Maass and colleagues [16], self-expanding metallic stents by Cesare Gianturco's group [17, 18],and balloon expandable stainless steel stent by Julio Palmaz and colleagues [19], and a modified version of the Palmaz stent by Schatz et al. [20].

It was not until March 1986 that Ulrich Sigwart and Jacques Puel implanted the first human coronary vascular stent [21]. This implant was followed by a series of 24 coronary procedures in 19 patients; all received a self-expanding stainless steel version of the commercially available Wallstent [Medinvent SA, Lausanne, Switzerland; now owned by Boston Scientific, Maple Grove, MN, USA; [22]]. While deployments were successful,

complications did arise in 3 patients as a result of stent thrombosis; however, the preliminary findings and 9-month follow-up did indicate the success of endovascular stenting as a treating for coronary artery disease. Following the pioneering work with self-expanding stents, the next generation of stents, and the first that were approved by the Federal Food and Drug Administration, were balloon expandable (Palmaz-Schatz, Johnson & Johnson, Warren, NJ; Flex-Stent, Cook Medical, Inc., Bloomington, IN). The Palmaz-Schatz stent design was employed in some of the first randomized trials to directly compare vascular stenting to balloon angioplasty in patients with de novo lesions. The initial multicenter study to ensure safety and efficacy of the device [94% success; [23]], and was followed by randomized trials that directly compared the Palmaz-Schatz stent to balloon angioplasty. The Stent Restenosis Trial (STRESS) examined approximately 407 patients that either received a stent (n = 205) or balloon angioplasty alone (n = 202). Six-month angiographic data indicated that restenosis, defined as approximately 50% stenosis under angiography, was approximately 10% lower in the patient group that received the stent [24]. The Belgian-Netherlands Stent Study (BENESTENT; 259 patients in stent group, 257 patient in balloon group) confirmed these results, as one-year follow up data indicated restenosis rates were 11% lower in the patients that received the Palmaz-Schatz stent [25]. These two initial comparative studies were the first to report the benefits of elective native coronary artery stenting in reducing the need for repeat vascular intervention, however it should be noted that restenosis rates in the stent groups were still high (STRESS: 31.6%, BENESTENT: 10%).

Since the first clinical findings exhibiting the efficacy and advantages of vascular stenting, numerous strategies and technologies have greatly advanced this revolutionary medical treatment. These strategies have improved all aspects of this percutaneous procedure from deployment to long-term outcomes. However, neointimal hyperplasia and the development of restenosis still remains a persistent, although decreasing, problem. Thus, as this procedure is a standard for the treatment of atherosclerosis, it is imperative that research efforts be devoted to increasing the success rate of this therapy.

Dissertation Synopsis

The dissertation presented herein is a collection of two independent projects, both of which constitute efforts in the field of cardiovascular biomechanics. The first section (Chapters II – V) presents work that discusses the solid biomechanical implications of implanting vascular stents that vary in the geometric design. In particular, the development of an optimization algorithm to reconcile three competing and physiologically relevant solid mechanical factors (Chapter II), the examination of stents deployed in tapered arteries (Chapter III), the effects of altering stent design and atherosclerotic plaque mechanical properties (Chapter IV), and the investigation of the pathobiological response to stent-induced variations in artery wall stress (Chapter V) are presented. Collectively, these works offer insight into the role of solid biomechanics and stent design on failure rates of these interventional devices. The second section (Chapter VI) investigates the microstructural organization of vascular tissue using novel nonlinear optical microscopy techniques. Specifically, the work examines collagen and elastin fiber orientation in the sub-endothelial

region of arterial tissue, and how the application of mechanical loads alters their alignment. Moreover, the work presented provides structural information of vascular tissue that can then be incorporated into computational modeling techniques, as presented in Chapters II – V, for the evaluation of medical devices.

CHAPTER II

STENTED ARTERY BIOMECHANICS AND DEVICE DESIGN OPTIMIZATION*

Overview

The deployment of a vascular stent aims to increase lumen diameter for the restoration of blood flow, but the accompanied alterations in the mechanical environment possibly affects the long-term patency of these devices. The primary aim of this investigation was to develop an algorithm to optimize stent design, allowing for consideration of competing solid mechanical concerns (wall stress, lumen gain, and cyclic deflection). Finite element modeling (FEM) was used to estimate artery wall stress and systolic/diastolic geometries, from which single parameter outputs were derived expressing stress, lumen gain, and cyclic artery wall deflection. An optimization scheme was developed using Lagrangian interpolation elements that sought to minimize the sum of these outputs, with weighting coefficients. Varying the weighting coefficients results in stent designs that prioritize one output over another. The accuracy of the algorithm was confirmed by evaluating the resulting outputs of the optimized geometries using FEM. The capacity of the optimization algorithm to identify optimal geometries and their resulting mechanical measures was retained over a wide range of weighting coefficients. The variety of stent designs identified provides general guidelines that have potential clinical use (i.e. lesion-specific stenting).

---

* With kind permission from Springer Science+Business Media: Medical and Biological Engineering and Computing, Vol. 45, 2007, pp. 505-513, L.H. Timmins, M.R. Moreno, C.A. Meyer, J.C. Criscione, A. Rachev, J.E. Moore, Jr.

Introduction

Cardiovascular diseases (CVD) have been the principal cause of death in the United States for the past century, with total direct and indirect costs estimated to reach $403.1 billion USD in 2006 [26]. Atherosclerosis is one of the most serious forms of CVD and is characterized by an accumulation of atheromatous lesions in focal regions of the vasculature, leading to a reduction in blood flow. Treatment options include bypass grafting, balloon angioplasty and stent placement, with the latter two gaining popularity due to their less invasive nature. Vascular stents are essentially scaffolds designed to prop open diseased arteries. Beginning with the first human implantation of a balloon expandable stent in 1986 [22], technological advances in stent design, deliverability, and drug-coatings have expanded the application and success rate of the procedure. Presently, the primary concern with this procedure is restenosis, or the development of a new blockage in the stented artery.

Restenosis is a multi-stage process characterized by thrombus deposition, inflammation, proliferation, and arterial wall remodeling, leading to neointimal thickening [27]. In the early days of stent implantation, approximately one-third of patients suffered from restenosis within 6 months of stent deployment [28]. Subsequently, there has been a significant effort devoted to reducing the clinical failures due to restenosis. With advances in stent design, restenosis rates after stent implantation in coronary arteries fell to around 20%, with some variation depending on the design of the stent [29]. Further success in reducing restenosis rates has been achieved with the advancement of drug-eluting stent technology. This technology involves covering stents with thin biodegradable polymer coatings in which anti-proliferative drugs designed to minimize smooth muscle cell proliferation are

embedded. While drug-eluting stents have decreased restenosis rates in coronary arteries to near 10% [30], incomplete endothelization of stent struts, lack of demonstrated success in peripheral arteries, and the lack of extensive long-term follow-up studies still limit this technology [31-33]. Thus, there is still cause to improve stent design for the minimization of restenosis. Improving the biomechanical interaction of the stent and artery wall is one strategy for accomplishing this goal.

The placement of a stent inside an artery has profound implications on the stresses in the artery wall. The changes in artery wall stress are long-term, lasting far beyond the acute injuries associated with deployment issues such as dog-boning and twisting due to balloon folding [34]. Stent oversizing can lead to strut-imposed vascular injury after stent deployment, which has been shown to dictate the extent of intimal thickening in animal models [35]. The presence of a highly rigid stent can subject the artery to extremely high, non-physiologic stress concentrations [36], and large stress gradients at the artery–stent junction [37]. Arterial straightening is another concern after stent deployment. The rigid stent prevents the artery from undergoing cyclic flexure due to the pulsatile nature of the vascular system, and can lessen the degree to which vascular cells express potentially beneficial substances [38]. Moreover, re-endothelialization can also be hindered by stent-induced reductions in cyclic stretch [39, 40]. In addition, stent implantation affects the flow patterns within an artery as both computational and experimental studies have shown [41-43]. An important challenge to stent design optimization arises from the fact that design properties mediate these concerns and while a particular design characteristic may minimize the effects of one concern, it may exacerbate another. For example, a stent high in radial

stiffness will achieve greater lumen gain, but will also induce higher stresses in the artery wall and perhaps limit the degree of cyclic stretch. Therefore, optimization of stent technology will require compromise, balance between competing interests, and an understanding of the impact that varying a given design characteristic may have on arterial wall reaction and restenosis formation.

The finite element method (FEM) is a widely used computational modeling technique that has been employed to investigate the mechanical implications of vascular stenting. Evidence suggests that restenosis rates vary with stent design [29]. Consequently, numerous studies have employed FEM to look at various stent geometries and determine the patterns of arterial wall stress that they induce. These studies have examined commercially available stents [44, 45] and generic designs [36]. Presently, only one study has attempted to evaluate the influence of specific stent design parameters on the stress field induced in a healthy artery wall [36]. The stents were defined by three geometric parameters: strut spacing (h), radius of curvature (ρ), and axial amplitude (f), illustrated in Fig. 2.2. This study found that stent designs characterized by large strut spacing, a non-zero radius of curvature, and large amplitude induced lower stresses on the vessel. Conversely, designs employing tight strut spacing, a zero radius of curvature, and low amplitude induced higher stresses on the artery. The stent designs that induced higher stresses also distended the artery to a greater degree, although the differences in final minimum diameter relative to the low stress stents in the healthy artery models were small (within 90 μm).

Herein we aim to extend the work of Bedoya et al. [36] and refine the stent strut configuration, via varying specific design parameters, to optimize stent performance. The

results from the aforementioned investigation, demonstrated that differences in circumferential stress, radial displacement (indicative of lumen gain), and cyclic radial deflection (change in radial position from diastolic to systolic pressure) were strongly affected by stent strut geometry. Circumferential stress is the most likely culprit in disrupting artery wall structure, so this measure was chosen over others (e.g., von Mises) as a more direct representation of the deleterious effects of stents. While one would like to minimize circumferential stress to reduce trauma induced on the artery wall, from a clinical standpoint a stent must displace the artery to a diameter that will restore blood flow to distal tissues. It is also desirable to allow the artery wall to experience and respond to pulse pressure with as much natural deflection as possible. Herein, we propose an optimization algorithm that considers these three competing solid mechanical concerns after vascular stenting. The algorithm was designed to refine the strut configuration in the middle portion of the stent and identify a unique set of stent geometric parameters that maximizes lumen gain and cyclic radial deflection, while simultaneously minimizing wall stress. Using FEM, we evaluated the accuracy of our algorithm by testing the optimized designs in a non-diseased, three-dimensional, thick-walled, nonlinear model of a stented artery. Our objective in this investigation was to develop an algorithm to process the data obtained from existing computational models that allowed for the generation of optimized stent designs based on reconciling three competing and physiologically relevant solid mechanical factors (circumferential stress, lumen gain, and cyclic radial deflection) of a stented artery.

Methods

With the abundance of competing solid mechanical concerns following stent implantation and the need to reconcile these concerns via some form of systematic compromise in stent design considerations, we have developed an algorithm that refines the strut configuration in the middle portion of the stent to provide an optimal mechanical environment. The accuracy of the optimization method was confirmed by evaluating the biomechanical impact of the optimized geometries in computational models of stented arteries.

Optimization Algorithm. Data obtained from previous computational models that analyzed distinct variations in stent geometrical parameters [36] were fit with an optimization function for which a minimum value was sought. Nodal values of tensile circumferential (hoop) stress at diastolic pressure, the pressure at which the stent induces the highest stresses, and radial displacement, at systolic and diastolic pressures, were taken from the inner surface of the middle quadrants of the stented model, defined as the region of interest herein. Behavior at the ends of the stent, in the region of compliance mismatch between the relatively rigid stent and the artery wall, was not considered. For each of the eight stent designs evaluated in Bedoya et al. [36] three values were extracted from the region of interest: percentage of the artery inner surface subjected to Class II critical hoop stresses (greater than 510 kPa) as defined in Bedoya et al. [36], minimum luminal gain (*LG*), i.e.,

$$LG = \frac{A_{post} - A_{pre}}{A_{pre}} \tag{2.1}$$

where A_{pre} is the cross-sectional area of the lumen before stent deployment, A_{post} is the cross-sectional area after stent deployment, and maximum cyclic radial deflection. The values were normalized from 0 to 1 for the eight FEM models. High radial displacement is preferred following stent implantation, therefore the model corresponding to maximum lumen gain was given a value of 0. Cyclic radial deflection should be maximized following stent deployment, thus the model corresponding to the least deviation from the cyclic radial deflection of a normal, healthy artery was given a value of 0. One could also imagine a definition of cyclic radial deflection based on cyclic circumferential stretch. In these models, the local circumferential stretch is nearly directly proportional to radial deflection, so the results would be approximately the same. Conversely, wall stress should deviate as little as possible from that which is present in a normal healthy artery wall to prevent any adverse biological response following stent deployment; therefore the model corresponding to the smallest deviation in circumferential stress from a healthy artery was given a value of 0. A minimal value for the optimization equation given by

$$G(h,\rho,f) = \alpha G_{\sigma}(h,\rho,f)^2 + \beta G_{LG}(h,\rho,f)^2 + (1-\alpha-\beta)G_{D}(h,\rho,f)^2 \tag{2.2}$$

where h, ρ, and f are the design parameters—strut spacing, radius of curvature, and axial amplitude, respectively—defined in the aforementioned investigation, was sought.

$G_\sigma(h,\rho,f)$ was defined as the normalized fraction of the intimal surface subjected to Class II critical stresses (>510 kPa). This threshold value provides an acceptable degree of sensitivity for our model parameters (diameter, wall thickness, artery wall properties, etc.). $G_{LG}(h, \rho, f)$ and $G_D(h, \rho, f)$ were defined as the normalized values of minimum luminal gain and maximum cyclic radial deflection within the region of interest, respectively, after stent deployment. The weighting coefficients, α and β, represent the relative importance of the circumferential wall stress, lumen gain, and cyclic radial deflection.

Multi-dimensional linear Lagrange interpolation was implemented to approximate the values of the specific normalized outcomes (G_σ, G_{LG}, G_D) in the region bounded by the limits of the stent design parameters, defined as the design space herein, modeled in Bedoya et al. [36], with ranges (h: 1.2–2.4, ρ: 0–0.3, f: 0.6–1.8). This parameter range is representative of the commercially available designs, which must incorporate design criteria such as expand- ability and fatigue behavior. The interpolation method is precisely analogous to that used by the 8-node 3D element [46]; yet rather than nodes in 3-space, our nodes are the eight simulations with the values of the design coordinates (h, ρ, f) as follows: (1.2, 0, 0.6), (1.2, 0.15, 0.6), (1.2, 0.3, 0.6), (1.2, 0.3, 1.2), (2.4, 0.3, 1.2), (2.4, 0, 1.8), (2.4, 0.15, 1.8), (2.4, 0.3, 1.8). The specific normalized outcome values were determined by

$$\begin{aligned} G_x = {} & G_x^1(1-h)(1-\rho)(1-f) + G_x^2(1-h)(\rho)(1-f) + G_x^3(h)(\rho)(1-f) + \\ & G_x^4(h)(1-\rho)(1-f) + G_x^5(1-h)(1-\rho)(f) + G_x^6(1-h)(\rho)(1-f) + \\ & G_x^7(h)(\rho)(f) + G_x^8(h)(1-\rho)(f) \end{aligned} \tag{2.3}$$

where x corresponds to one of the specific normalized outcomes, G_x^n (N = 1...8) corresponds to the value of one of the specific normalized outcomes at each of the eight computational models, and h, ρ, and f are incremental positions within the design space. Similarly, the location of G_x^n is given by

$$\begin{aligned} L_x = {} & L_x^1(1-h)(1-\rho)(1-f) + L_x^2(1-h)(\rho)(1-f) + L_x^3(h)(\rho)(1-f) + \\ & L_x^4(h)(1-\rho)(1-f) + L_x^5(1-h)(1-\rho)(f) + L_x^6(1-h)(\rho)(1-f) + \\ & L_x^7(h)(\rho)(f) + L_x^8(h)(1-\rho)(f) \end{aligned} \tag{2.4}$$

where x corresponds to either the h, ρ, or f location and L_x^n (N = 1...8) corresponds to the location of one of the eight designs evaluated by Bedoya et al. [36]. Substitution of the values of the specific normalized outcomes at each specific incremental location within the design space into Eq. 2.4, along with predetermined weighting coefficients returns a value for the composite normalized outcome $G(h, \rho, f)$. Figure 2.1 is a representation of the interpolated data for specified weighting coefficients ($\alpha = 0.25$ and $\beta = 0.55$) within the design space. The geometric stent design parameters (h, ρ, f) corresponding to the minimum $G(h, \rho, f)$ were determined as the optimum design parameters (i.e., the outputs of the optimization algorithm).

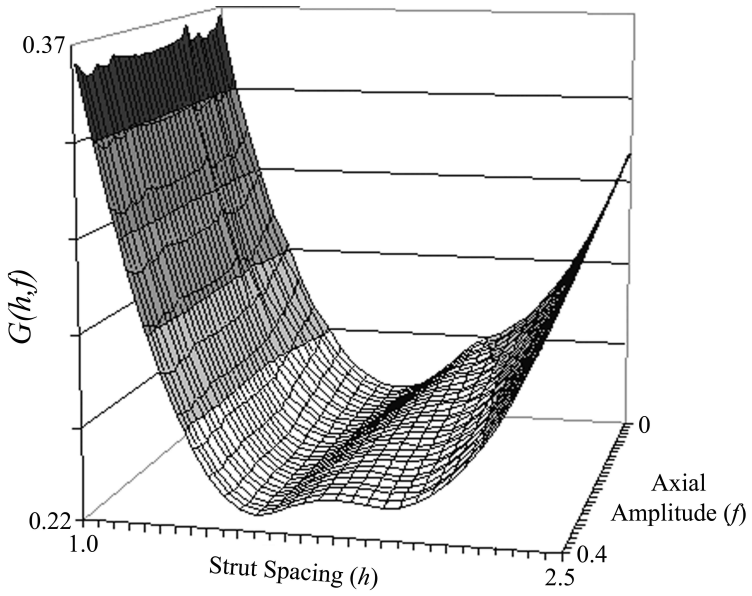

Figure 2.1: Interpolated Data Within the Design Space for Specified Weighting Coefficients ($\alpha = 0.25$ and $\beta = 0.55$). Note that this figure illustrates a case where the radius of curvature (ρ) was held constant and *G(h,f)* was plotted against the strut spacing (*h*) and axial amplitude (*f*). The optimization algorithm locates the global minimum varying all three design parameters.

Finite Element Modeling. The methods used to construct and model the stent geometries obtained from the optimization scheme have been previously reported in Bedoya et al. [36]. Briefly, a Matlab (MathWorks, Natick, MA, USA) subroutine was written to generate stent designs based on the parameters identified in the optimization algorithm. A separate program was created to automate the generation of three- dimensional stents in MSC.Patran (MSC Software, Santa Ana, CA, USA). Stent designs had an expanded outer radius of 1.2375 mm, which was 10% larger than the systolic radius measured at the inner surface and is consistent with manufacturers' recommendations and common stenting practice [47]. Because of the repeating nature of the successive rings in this stent design and the fact that any effects from the edges of the stent have dissipated within the first ring

segment, the mechanical environment in the middle section of the stent model (the space between the two inner rings) is equivalent to the mechanical environment of any two inner rings of a full length stent [36]. Thus, it is only necessary to model a portion of the full length stent, as seen in Fig. 2.2. Stent struts had a constant thickness of 100 μm and the stent material was modeled as 316L stainless steel (E = 200 GPa, ν = 0.3).

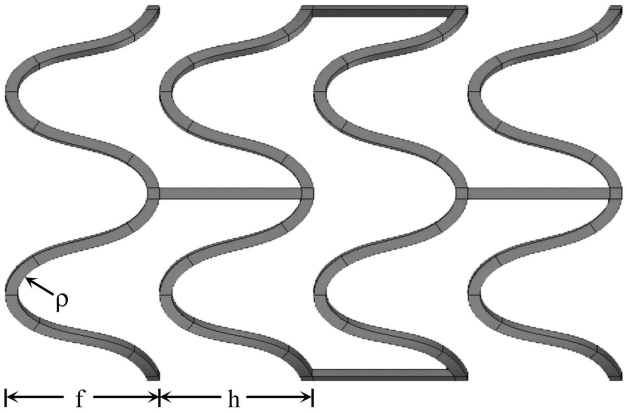

Figure 2.2: Design Parameters. Generic stent showing the three parameters identified by the optimization algorithm: strut spacing (*h*), radius of curvature (ρ) and axial amplitude (*f*). The resulting stent geometries were then modeled to determine the accuracy of the algorithm.

The artery material properties utilized have been previously described [36]. Briefly, mechanical testing of porcine common carotid arteries was conducted using a modified version of the Computer Aided Vascular Experimentation (CAVE) device described by Humphrey et al. [48]. The acquired data were used to determine the constants for the constitutive model, which took the form given by Eq. 2.5

$$W = C_{10} \cdot (I_1 - 3) + C_{01} \cdot (I_2 - 3) + C_{11} \cdot (I_1 - 3) \cdot (I_2 - 3) + C_{20} \cdot (I_1 - 3)^2 + C_{30} \cdot (I_1 - 3)^3 \quad (2.5)$$

where C_{10} = 25,466 Pa, C_{01} = –11,577 Pa, C_{11} = –506 Pa, C_{20} = 1,703 Pa, and C_{30} = 1,650 Pa. The artery model employed herein was characterized as a straight homogenous circular cylinder with isotropic nonlinear hyperelastic mechanical properties.

The finite element method was employed using MSC.Patran with MSC.Marc as the nonlinear solver (MSC Software, Santa Ana, CA, USA). The boundary conditions applied were the same as those utilized by Bedoya et al. [36]. Briefly, boundary conditions were applied in multiple steps. The quarter vessel model was stretched 59%, simulating the in vivo axial tethering that was measured during vessel harvesting. The vessel was then inflated by applying a pressure of 225 mm Hg, dilating the vessel to a radius greater than the outer radius of the 10% oversized stent. The stent was then translated in the axial direction from its original position outside of the vessel until the stent and vessel midpoints coincided. The pressure was then reduced to systolic and subsequently diastolic. Symmetry displacement boundary conditions were applied to both the stent and vessel to only allow in-plane deformations. An analytical contact boundary condition was applied restricting the future motion of contacting bodies to be only in the normal direction. Mesh independence was determined by convergence of radial displacement (<<1%) and circumferential wall stress (<4.5%) along the length of the stented model at systolic pressure.

Results

Results from our optimization algorithm suggest that unique sets of geometric parameters that correspond to global minima in $G(h, \rho, f)$ can be identified over a wide range of optimization weighting coefficients. Post-optimization FEM results indicate that the algorithm accurately predicted $G(h, \rho, f)$, for all stented artery models, in addition to values for percent area subjected to Class II hoop stresses (>510 kPa), minimal lumen gain, and maximum cyclic radial deflection. For example, the optimization algorithm predicted a value of $G(h, \rho, f) = 0.201$ for $\alpha = 0.33$ and $\beta = 0.33$, compared to the actual value of 0.211 calculated for the stent with the resulting optimized geometry. Furthermore, the algorithm predicted values for percent area subjected to Class II hoop stresses, minimal lumen gain, and maximum cyclic radial deflection of 24%, 0.87, and 0.027 mm, respectively, whereas evaluation of finite element data returned values of 21%, 0.86, and 0.029 mm. In this case, the resulting optimal geometry had a strut spacing (h) of 2.28 mm, radius of curvature (ρ) of 0.3 mm, and axial amplitude (f) of 1.14 mm (Table 2.1).

Table 2.1: Values of the objective function *G(h,ρ,f)* and its components as predicted by the optimization algorithm, and as actually calculated using FEM data from the resulting geometries (shown at left). CRD = cyclic radial deflection.

$\alpha = 0.33$, $\beta = 0.33$ (Equal weighting)			Optimization algorithm	FEM results
	h = 2.28 mm	$G(h, \rho, f)$	0.201	0.211
	ρ = 0.3 mm	% Class II	24%	21%
	f = 1.14 mm	Lumen gain	0.87	0.86
		CRD	0.027	0.029
$\alpha = 0.75$, $\beta = 0.125$ (Emphasize stress)			Optimization algorithm	FEM results
	h = 2.28 mm	$G(h, \rho, f)$	0.091	0.084
	ρ = 0.135 mm	% Class II	10%	1.2%
	f = 1.68 mm	Lumen gain	0.84	0.84
		CRD	0.032	0.032
$\alpha = 0.125$, $\beta = 0.75$ (Emphasize lumen gain)			Optimization algorithm	FEM results
	h = 1.44 mm	$G(h,\rho,f)$	0.172	0.182
	ρ = 0.192 mm	% Class II	63%	73%
	f = 1.128 mm	Lumen gain	0.96	0.98
		CRD	0.016	0.013
$\alpha = 0.125$, $\beta = 0.125$ (Emphasize CRD)			Optimization algorithm	FEM results
	h = 2.4 mm	$G(h, \rho, f)$	0.107	0.109
	ρ = 0.135 mm	% Class II	3.5%	1.1%
	f = 1.8 mm	Lumen gain	0.83	0.82
		CRD	0.034	0.035

The ability of the optimization procedure to identify optimal geometries and their resulting mechanical measures was retained over a wide range of weighting coefficients (Table 2.1). Emphasizing circumferential stress ($\alpha = 0.75$, $\beta = 0.125$) resulted in predicted and actual $G(h, \rho, f)$ values of 0.091 and 0.084, respectively. Moreover, lumen gain and cyclic radial deflection differed by <1 and <<1%, respectively, between the predicted and FEM modeled values. Increasing the importance of lumen gain ($\alpha = 0.125$, $\beta = 0.75$) exhibited similar findings, with only a 6% difference in $G(h, \rho, f)$ values between the optimization algorithm and post-optimization FEM result, with values of 0.172 and 0.182, respectively. Values of $G(h, \rho, f)$ deviated by <2% when emphasis was placed on cyclic radial deflection ($\alpha = 0.125$, $\beta = 0.125$). The optimization algorithm predicted a $G(h, \rho, f)$ value of 0.107, compared to the actual value of 0.109 calculated from the post-FEM results of the optimized geometry. Table 2.1 summarizes the aforementioned results from the optimization algorithm and finite element modeling for all stent designs investigated. Figure 2.3 shows the plots of the circumferential stress distribution for the four optimized geometries from the FE results.

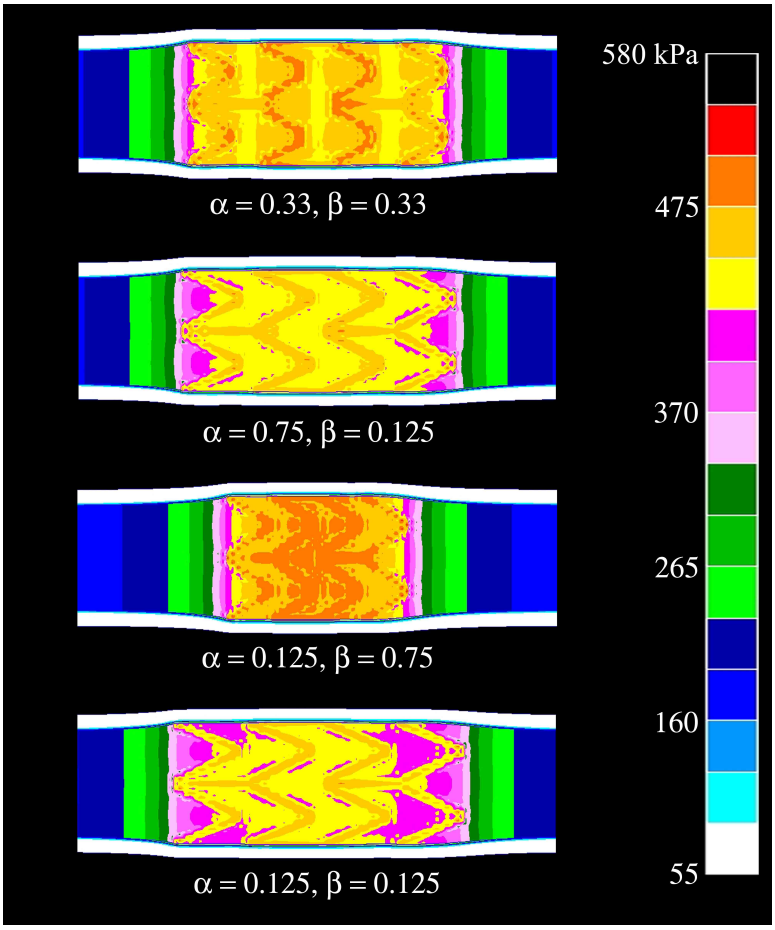

Figure 2.3: Circumferential Stress Distribution in the Four Optimized Designs.

Noticeable trends in stent geometric parameters were observed between stent designs when emphasis was placed on any of the three mechanical measures (circumferential stress, lumen gain, cyclic radial deflection). For example, increasing the weight on hoop stress ($\alpha = 0.75$, $\beta = 0.125$) resulted in a trend where strut spacing (h) and axial amplitude (f) increased, while radius of curvature (ρ) decreased. In comparing the geometric parameters resulting from $\alpha = 0.125$, $\beta = 0.75$ (emphasize lumen gain) with the optimized parameters resulting from the emphasis on circumferential stress, it is seen that h increases from 1.44 to 2.28 mm,

ρ decreases from 0.192 to 0.135 mm, and *f* in- creases from 1.128 to 1.68 mm. Emphasizing cyclic deflection resulted in an identical shift in geometric parameters, i.e., *h* and *f* increased, ρ decreased. These adjustments make the stent more compliant, and thus more likely to deflect with the artery wall. Examination of the designs resulting from $\alpha = 0.33$, $\beta = 0.33$ (equal weighting) and $\alpha = 0.125$, $\beta = 0.125$ (emphasize cyclic radial deflection) shows that *h* increases from 2.28 to 2.4 mm, ρ decreases from 0.3 to 0.135 mm, and *f* increases from 1.14 to 1.8 mm. Furthermore, emphasizing lumen gain also resulted in an apparent shift in optimized geometric parameters. Consider the comparison between the designs that result from $\alpha = 0.75$, $\beta = 0.125$ (emphasize hoop stress) and $\alpha = 0.125$, $\beta = 0.75$ (emphasize lumen gain). In this comparison, the increase in weight of lumen gain results in a decrease in *h* from 2.28 to 1.44 mm, an increase in ρ from 0.135 to 0.192 mm, and a decrease in *f* from 1.68 to 1.128 mm. In general, when either a reduction in circumferential stress of an increase in cyclic radial deflection was emphasized, strut spacing (*h*) and axial amplitude (*f*) increased, while radius of curvature (ρ) decreased. Conversely, increasing the weight of lumen gain leads to a decrease in strut spacing (*h*) and axial amplitude (*f*), while radius of curvature (ρ) increased.

Discussion and Conclusions

This study demonstrates that medical device design optimization is feasible under complex circumstances. For this specific case of stent design for improved biomechanics, the models are based on geometrically and materially non- linear modeling techniques and output parameters that depend in complex ways on the input (design) parameters. Still, the

optimization techniques produced results that were confirmed by modeling the specific optimized geometries. The differences between the predictions of the optimization and the actual mechanical parameters shown in Table 2.1 are due to curve-fitting non-linear data, and not significant enough to detract from the success of the optimization scheme. Using these techniques, design guidelines for other medical devices may be achieved that incorporate considerations for long-term clinical failure modes. In this case, it was possible, for example, to arrive at stent designs that minimize artery wall stress, which is presumably important for development of restenosis [36, 37, 44]. Optimized geometries in other cases with more or less emphasis on minimum lumen gain or cyclic radial deflection were also identified, indicating that the optimization scheme is reliable over a wide range of desired outputs. While it is possible to cover the entire parameter space with a large number of computational models, this is not feasible in cases such as stented arteries, each of which takes at least several days to converge. The optimization scheme identifies optimal geometries in a more efficient manner.

The effects of the stent geometric parameters on the artery wall mechanical parameters (circumferential stress, lumen gain, and cyclic radial deflection) are due to a combination of factors. First, the design parameters affect the radial rigidity of the stent, independent of the artery, as determined by the degree of radial displacement. It is evident that the stiffer the stent, the greater the lumen gain and zones of high stress, and the lesser degree of cyclic flexure. Second, the design parameters determine the unique geometry of the ‘‘panels’’ of artery wall material between the struts, which in turn lead to variations in stress values and radial displacements. If stent struts were perfectly rigid, larger panels (high strut spacing)

would induce higher stresses in the panels as compared to shorter stent panels. However, larger strut spacing also leads to a more compliant stent, which reduces the distending force on the artery wall, and thus the stress. The degree of cyclic radial deflection experienced by the artery wall is also affected by the additional effective stiffness of the panel provided by the distension due to the stent. A greater degree of artery wall stretching in either the axial or circumferential direction (which depends on strut configuration) will make the artery less likely to deform in response to changing pressure. While our optimization study only calculates the collective effects of all mechanisms and not the particular influences on each mechanism, these individual mechanisms provide insight into the sensitivity of the biomechanical environment after stent implantation. There are, of course, other considerations for stent design beyond the scope of this study, such as optimal radiopacity, fatigue behavior, foreshortening, trackability and deliverability. While these are important issues, stent designers are already familiar with the methods to improve them.

It is important to note the limitations associated with the models on which this optimization was based. As pointed out in Bedoya et al. [36], the artery wall is assumed to be a homogeneous, isotropic, hyperelastic cylinder. Features such as stenoses, curvature, etc., were not included. The inclusion of such complicating factors would greatly increase the number of variables required to perform the optimization scheme, such as the stenosis shape and mechanical properties, and the degree of curvature. More importantly, the inclusion of these features would not change the relative rankings of the stents, and thus the optimization results would be largely unchanged. In other words, a stent that minimizes stress in a healthy artery model would also minimize stress in a diseased or curved artery model. This study is

also limited to the solid mechanical interaction of the stent and artery wall, and does not include the effects of flow-induced wall shear stress. The effects of these same design parameters on blood flow patterns has been previously investigated [42], wherein it was found that adjusting the parameters such that the struts are aligned with the flow direction provides the least flow disturbance.

There are additional stent design parameters that could be varied to achieve optimized designs, such as stent material (implying changes in material properties) and strut thickness. The influence of these parameters is not difficult to predict. Increasing either the material stiffness or strut thickness would result in higher artery wall stress, higher lumen gain and less cyclic radial deflection. Since these monotonic effects are likely to be preserved despite changes in the parameters varied here, they were kept constant. There is also the additional concern that increasing the number of variables in this kind of an optimization problem could hinder the ability to arrive at an optimal design. The degree and locations of plastic deformation during expansion of the stent (which certainly are related to material properties and strut thickness) may influence the stent/artery wall interaction, but these effects were not included here. It is likely that the variations in geometric parameters dominate over such effects, although this remains to be proven. The relative rankings of the stents for the purposes of optimization are not likely to be affected.

This study is also limited to the changes in artery wall stress induced by the stent, and does not address cellular responses to the additional harmful effects of acute vascular injuries associated with balloon expansion of the artery [49]. Histological studies implicate the disruption of the internal and external elastic laminae in an increased risk for restenosis

[35]. The additional artery wall strain associated with balloon pressurization beyond that predicted in our models (also known as stent recoil) is typically just a few percent [50], but could result in additional laminae disruption. The non-uniform expansion of the stent by the balloon (dog-boning) and stent twisting induced by the expansion of folded balloons are examples of stent deployment phenomena that could induce additional acute injury in the artery wall. Axial strain components induced by dog-boning could add to laminae disruption, as could shearing due to stent twisting. The relative importance of these particular injuries on restenosis is unknown. Further investigation of the importance of these acute phenomena relative to the acute and long- term stress from the stent is warranted. In particular, the potential for additional injury at the ends of the stent, where stresses are already high, should be of interest. The present study only included the middle portions of the stented segments. However, it is important to note that the designs that minimized stress in the middle sections also minimized stress at the end segments due to the higher degree of stent compliance [36].

The variety of stent designs identified in this study (Table 2.1) provides general guidelines for stent design that can be used clinically to treat different disease states (i.e., lesion specific stenting). Atherosclerotic lesions are comprised of a variety of heterogeneously distributed constituents (e.g., soft lipid pool, fibrotic tissue, calcified plaque, etc.) each with unique mechanical properties. Consequently, the overall mechanical behavior of atherosclerotic lesions varies widely across the patient populations. It would be potentially detrimental to implant a stent that can cause unnecessary trauma to the artery wall or not provide sufficient scaffolding to diseased tissue; with due consideration of the effects of given design parameters these unfavorable outcomes can be avoided. For example, if

confronted with a relatively stiff, perhaps calcified atherosclerotic plaque, the clinician can choose a design that optimizes minimum luminal gain (maximizing radial displacement), realizing that the minimum requirement of restoring blood flow should be met at the expense of potentially high stresses on the artery wall. Our results indicate that a smaller strut spacing and smaller amplitude would be more appropriate in these cases. On the other hand, if a target lesion is relatively rich in soft lipid content, a design that minimizes artery wall stress could be preferable. Our results indicate that stents with relatively high strut spacing would be more suitable. It should be noted that strut spacing is the limiting factor for axial spacing, thus there are limitations in parameter configurations to ensure that stent designs can be manufactured in the collapsed configuration. These design guidelines, while arrived at using a generic stent design, are generally applicable to any commercially available stent design. The optimization methodology demonstrated here could also be applied specifically to other design schemes that lend themselves to parameterization. Lastly, the importance of artery wall stress in relation to other phenomena that could be involved in the restenotic process should be determined through carefully designed in vivo studies, or perhaps in vitro studies with stents implanted in isolated, perfused arteries.

CHAPTER III

MECHANICAL MODELING OF STENTS DEPLOYED IN TAPERED ARTERIES*

Overview

The biomechanical interaction of stents and the arteries into which they are deployed is a potentially important consideration for long-term success. Adverse arterial reactions to excessive stress and the resulting damage have been linked to the development of restenosis. Complex geometric features often encountered in these procedures can confound treatment. In some cases, it is desirable to deploy a stent across a region in which the diameter decreases significantly over the length of the stent. This study aimed to assess the final arterial diameter and circumferential stress in tapered arteries into which two different stents were deployed (one stiff and one less stiff). The artery wall was assumed to be made of a strain stiffening material subjected to large deformations, with a 10% decrease in diameter over the length of the stent. A commercially available finite element code was employed to solve the contact problem between the two elastic bodies. The stiffer stent dominated over arterial taper, resulting in a nearly constant final diameter along the length of the stent, and very high stresses, particularly at the distal end. The less stiff stent followed more closely the tapered contour of the artery, resulting in lower artery wall stresses. More compliant stents should be considered for tapered artery applications, perhaps even to the exclusion of tapered stents.

---

* With kind permission from Springer Science+Business Media: Annals of Biomedical Engineering, Vol. 36(12), 2008, pp. 2042-2050, L.H. Timmins, C.A. Meyer, M.R. Moreno, J.E. Moore, Jr., Mechanical Modeling of Stents Deployed in Tapered Arteries.

Introduction

Cardiovascular disease is the leading cause of death in developed countries. In the U.S. it has been estimated that costs associated with this disease will be in excess of $430 billion in 2007 [51]. Atherosclerosis, one of the more common and serious forms of this disease, is characterized by focal accumulation of material within an artery that restricts blood flow. Spatial variations in mechanical factors such as blood flow patterns and artery wall stresses have been implicated in atherogenesis. Treatment options (e.g. stenting, balloon angioplasty, etc.) for arteries occluded by atheromatous lesions typically alter the local mechanical environment. Given the influence of mechanical factors in disease development, this is a consequence that must be considered when attempting to determine the efficacy of a given therapeutic option.

Vascular stenting has proven to be an effective treatment option for most patients with atherosclerosis; though complications such as restenosis, or the development of neointimal hyperplasia within the stented region following implantation, can result in the ultimate failure of the procedure. Stents are essentially tubular scaffolds comprised of a metallic mesh deployed inside the artery in order to prop the diseased region open and restore blood flow. To function properly and remain in place, stents are designed to be larger in diameter than the healthy artery – this characteristic of the therapy is referred to as “stent over-sizing”. As the artery is distended beyond normal physiologic limits, pathologic stresses are induced in the artery wall and the artery may be irreversibly damaged. Even in cases wherein acute tissue damage is minimal, cellular response to the new stress environment created by the stent can be problematic.

The mechanical mismatch is a particular concern for situations in which arterial diameter changes to a significant degree over the length of a stent. Such diameter changes can be encountered due to tapering or the need to deploy a stent from a parent vessel into a branch. This significant diameter change is sometimes the case in carotid artery stenting, but can also occur in femoral arteries. The clinician must then decide which diameter on which to base the stent sizing decision. A large diameter mismatch at the distal end of the stent could lead to excessive damage in the artery wall and increased risk for clinical failure. While there are tapered stents available in some markets, the geometric variations require more careful consideration of stent choice [52].

Modeling stent/artery interactions has mainly focused on applications in which arterial tapering is not a factor, either through simplifying assumptions or by modeling specific, non-tapered arteries. Rogers et al. [53] used two-dimensional linear elastic models to investigate balloon expansion with stent and artery contact. It was determined that high inflation pressures, wide stent-strut spacings, and more compliant balloon materials cause markedly larger surface-contact areas and contact stresses between stent struts. Consequently, it was concluded that stent design and deployment protocols play an important role in stenting outcomes. The stress fields induced by stents are as unique as the stents themselves. Consistent with these concepts, evidence suggests restenosis rates vary by stent design [29]. It is hypothesized that stent-induced stresses mediate processes conducive to the development of restenosis [54]. Therefore characterization of the stress field induced by a given stent design or “design parameter” is of particular interest to efforts to reduce restenosis rates in stent therapy.

Finite element modeling is commonly employed to investigate stresses and strains in stents and stented arteries. The quality of information gained is typically limited by challenges associated with establishing an appropriate constitutive models and the need to impose simplifications. Holzapfel et al. [55] modeled balloon expansion of a full 3-dimensional anisotropic diseased artery. It was proposed that the work provided tools with the potential to improve procedural protocols and the design of interventional instruments. Moreover, the techniques employed could be used as an aid in predicting post-angioplasty mechanical environments, which could subsequently be correlated with restenosis responses. Later, in works that presently constitute the most ambitious efforts to model diseased arteries, anisotropic plaque properties were characterized and a model of 3-dimensional stent artery interaction (incorporating parameterized commercially available stents) in a severely diseased iliac artery with 8 different components was developed [44]. Given evidence that regions near the ends of a stent are particularly susceptible to restenosis, Berry et al. [37] examined stresses in the artery wall in these locations. It was determined that high stress concentrations are imposed in these regions of compliance mismatch between the artery and the stent. Prendergast and colleagues [45] modeled the stent-artery interaction of commercially available stents (NIR – Boston Scientific; S7 – Medtronic AVE) on an idealized stenosed artery. They proposed the testing methodology as a pre-clinical testing tool, which could be used to compare and contrast existing stent designs as well as aid in developing novel stent designs. The mechanical properties of stents have been investigated by Migliavacca and colleagues. In a study of the influence of geometry on the stent behavior, they determined that a stent with a low metal-to-artery surface ratio has higher radial and

longitudinal recoil, but lower “dogboning” [34]. It was concluded that the strut thickness influences the stent performance in terms of foreshortening, longitudinal recoil and dogboning.

Bedoya et al. [36] investigated the effects of varying specific design parameters. Using a cylindrical scaffold constructed with sinusoidal rings joined by axially oriented connector bars, finite element models of generic stents were constructed by varying three design parameters - the strut spacing (h), the radius of curvature (ρ), and the axial amplitude (f) (Figure 3.1).

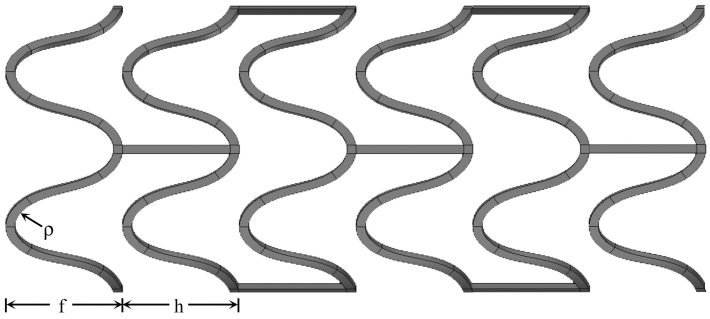

Figure 3.1: Stent Design Parameters. Illustrations of the stent designs employed, showing the three parameters used in their construction: h is connector bar length (or strut spacing), ρ is the radius of curvature at the crown junctions, and f is the axial amplitude.

The stent models were deployed in models of healthy circular cylindrical arteries. The effects of stent design on the stress field in the artery wall, radial displacement of the artery, and cyclic deflection of the artery were assessed. Designs that induced the greatest stresses in the artery wall, a characteristic considered unfavorable, also achieved the most favorable radial displacements. Conversely, designs that induced the lowest stresses in the

artery wall produced the smallest radial displacements. Timmins et al. [56] provided an optimization scheme to reconcile the mutually exclusive nature of the low stress vs high radial displacement relationship. In the interest of advancing modeling techniques, it is important to address the use of cylindrical, healthy artery models.

While stents are not typically deployed in healthy arteries, the use of healthy artery models is purposeful in comparative studies aimed at elucidating the effects of varying specific design parameters, without additional complicating factors. Incorporation of disease elements, i.e. stenoses, is potentially convoluting. Like vessel geometry, material properties of atherosclerotic lesions vary greatly, from soft lipid pools to stiff calcified plaques. In a comparative study of the effects of stent design, the use of a specific geometry and combination of mechanical properties from one patient may not provide generally applicable results. In addition, animal studies can be carried out to verify results. A healthy artery model would be most similar to the animal model used to validate computational results. Further justification arises from the contact between the stent and healthy arterial tissue at the edges of the stented region, as stents are generally longer than the diseased region to ensure proper radial support. As restenosis commonly develops at this site, examination of the biomechanical environment in this region has a major clinical significance.

However, it has been acknowledged that to improve clinical relevance the effects of the stenosis must ultimately be addressed. Moreover, arteries in regions of the vasculature that are particularly vulnerable to disease typically vary in diameter along the axial direction, i.e. taper. Tapered vessels present unique challenges to stent therapy. Though not yet commonly utilized, stents incorporating a tapered design are available, e.g. Protégé RX

(EV3, Plymouth, MN), designed for deployment in carotid arteries. In this case, the tapered form is intended to provide a more appropriate fit in the transition at the carotid bifurcation between the common carotid and smaller internal carotid artery. While rarely examined, coronary arteries also exhibit a degree of taper. Angiographic data suggested that left anterior descending (LAD) and right coronary arteries (RCA) taper approximately 14% and 9%, respectively, along their lengths in both men and women [57]. Even with the emergence of some tapered designs, the use of non-tapered stent designs in tapered vessels remains standard. The implications of this practice are the focus of the present investigation. Herein, we aim to employ the modeling techniques previously outlined [36] to investigate the effects of specific stent design parameters on wall stresses and radial displacements in healthy tapered vessels.

Methods

In order to examine the effects of stent design on tapered vessels, the finite element method was employed to determine final lumen diameter, as well as estimate stresses in the artery wall of the elastic stent/artery system in mechanical contact. The two stent models investigated, selected from the two extreme designs identified in Bedoya et al. [36], are intended to represent designs that have high (1Z1) and low (2B3) radial rigidity (Table 3.1). The artery wall model features non-linear, strain-stiffening mechanical properties, along with geometrical dimensions that agree with general observations of large tapered arteries.

Model Geometry. The 3D stent geometries investigated in this study have been previously identified [36]. Briefly, generic stent models were developed by varying three

specific design parameters – strut spacing (h), radius of curvature at the crown junctions (ρ) and axial amplitude (f) (Figure 3.1). From the aforementioned investigation two stent designs were selected, representing the extreme cases (based on evaluation of the stresses induced in the artery wall) of the stent designs investigated. Stent 1Z1 is characterized by a tight strut spacing, zero radius of curvature, and low amplitude, while stent 2B3 incorporates a large strut spacing, large radius of curvature and large axial amplitude. Both designs have a constant strut thickness and width of 100 μm and an outer radius of 2.475 mm, which is approximately 10% larger than the systolic inner radius of the artery at the proximal end of the stented region. Since the biomechanical interest in stenting tapered arteries is at the regions where diameter differences are largest (i.e. edges of the stented region), stent models have been scaled accordingly to ensure proper investigation, but yet still be computationally feasible. Thus, only a portion (approximately 9 mm in length) of a typical full length stent was modeled. The stent material was modeled as 316L stainless steel (E = 200 GPa, v = 0.3).

Table 3.1: Stent designs and parameter values.

Stent	Strut spacing, h (mm)	Radius of curvature, ρ (mm)	Axial amplitude, f (mm)
 **1Z1**	1.2	0	0.6
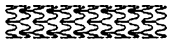 **2B3**	2.4	0.3	1.8

The tapered artery was modeled as an idealized, healthy, cylindrical vessel with proximal and distal radii values or 2.133 mm and 1.920 mm, respectively, at diastolic

pressure. These radii values correspond to a 10% taper, by diameter, or a taper angle of 0.43°, both of which agree with values taken from angiographic data of large arteries [58, 59]. The artery model was initially 18 mm in length under no axial load; with the stented region being the centermost 9 mm section. The artery material properties used in the computational models have been previously utilized [36], and were based on data obtained from pressure-diameter and force-elongation testing of porcine carotid arteries using a modified version of the Computer Aided Vascular Experimentation (CAVE) device described in Humphrey et al. [48] Data from the mechanical testing was used to determine the constants for the constitutive relation, which took the form:

$$W = C_{10} \cdot (I_1 - 3) + C_{01} \cdot (I_2 - 3) + C_{11} \cdot (I_1 - 3) \cdot (I_2 - 3) + C_{20} \cdot (I_1 - 3)^2 + C_{30} \cdot (I_1 - 3)^3$$

where, C_{10} = 25,466 Pa, C_{01} = -11,577 Pa, C_{11} = -506 Pa, C_{20} = 1703 Pa, and C_{30} = 1650 Pa. Ultimately, the artery model employed herein was characterized as a straight homogeneous tapered cylinder with isotropic non-linear hyperelastic mechanical properties.

FEM Simulations. The stent and artery models used in this study were developed with MSC.Patran; MSC.Marc was employed as the non-linear solver (MSC Software, Santa Ana, CA). The element and nodal numbers for the simulations varied slightly due to differences in stent design. All tapered vessel models consisted of 15232 elements (74657 nodes). The more rigid 1Z1 stent design was comprised of 922 elements (8928 nodes), while the model incorporating the more compliant 2B3 design was represented by 938 elements

(9036 nodes). The boundary conditions utilized included displacement boundary conditions, pressure and contact, and were applied in multiple stages. Initially an axial stretch ratio of 1.59 was applied to the vessel, simulating the axial tethering that was measured in vivo during carotid vessel harvesting. The vessel was then inflated by applying a pressure (35 kPa) sufficient to dilate the artery such that the oversized stent could be "implanted"; i.e. the stent was originally positioned outside the artery and then translated in the axial direction such that the stent and artery mid-points along that direction coincided. Pressure was then reduced to systolic levels and subsequently, to diastolic levels. Displacement boundary conditions only allowing in-plane deformations for the stent struts and vessel symmetry edges were imposed on these quarter models. An analytical contact boundary condition restricting the motion of nodes in contact with the opposite body was enforced. This contact condition ("glue" option in MSC.Marc) enforces multipoint constraint equations that restrict the motion of the contacting body to be strictly in the normal direction. Displacements were interpolated using quadratic Lagrange functions, while the spherical stress was interpolated with a linear function. The contact bodies were defined by C^2-continuous Non-Uniform Rational B-Splines surfaces (NURBS).

The computer cluster used to solve this boundary value problem consists of a head node with dual 2.8 Ghz 32-bit processors, 4GB of RAM. The slave nodes (15) consisted of single 2.8 GHz 32-bit processors, 2GB of RAM. The operating system of the computer cluster was RedHat 9. The version of Patran was 2005 release 2, and Marc 2005 release 1.

Evaluation Methods. The model results are all oriented such that the vessel tapers from left to right, i.e. the diameter at the right end of the stented portion is 10% smaller than

the diameter at the left end of the stented portion. As a measure of the stent ability to prop the vessel open adequately, the final radial position achieved by each design was assessed. Further, it is hypothesized that the development of neointimal hyperplasia following stent implantation is mediated by the anomalous stresses induced in the artery wall by the stent. Herein the circumferential (hoop) stresses are presented since they are most likely to cause disruption of the internal elastic lamina; a phenomenon that has been directly linked with restenosis formation [60, 61]. We have previously shown that circumferential stresses constitute the major contribution to the maximum principal stresses [36]. For reference purposes, the average circumferential stresses at the proximal and distal ends of the stented region are estimated using the Law of Laplace as 34 kPa at diastolic pressure. While this formula is not strictly applicable to this situation, because it is not valid for thick walled tubes, the values serve as a general guideline to provide an indication of the degree to which stent implantation affects stress in the artery wall relative to the unstented case. Averaging nodal circumferential stress values through the vessel thickness at the proximal and distal ends of the stented region of the tapered artery models results in values of approximately 50 kPa at diastolic pressure.

Nodal values of radial displacement and circumferential stress values on the intimal surface of each tapered artery model were obtained at diastolic pressure. Radial displacement values were used to determine final radial positions after stent deployment. To assess the impact of the stent along the tapered vessel, these values were averaged and plotted against the undeformed axial position. Nodal values were averaged along the azimuth angle (circumference) of the quarter vessel at identical undeformed axial locations along the artery.

This procedure was a convenient method to examine differences amongst stent designs, as well as compare against the unstented artery. Nodal circumferential stress values were also plotted as a colormap of the model for quantitative analysis. Both approaches are used herein to provide a more complete conception of the biomechanical impact of stent design on a tapered artery.

Convergence Criteria. Mesh convergence was evaluated as described in Bedoya et al. [36] Briefly, the mesh convergence study consisted of a three-step process. The first step was to perform mesh refinements in the model of the artery alone – with no contact – observing the variation of maximum principal (i.e. circumferential) stress distributions. The criterion used was that the maximum principal Cauchy stress field in the lumen and adventitia of the artery had to vary by less than 1%. The second step was to perform refinements in stents themselves by applying a pressure load on the outside of the stent and observing changes in displacements. The mesh was deemed converged when changes in displacement were less than 1% in radial displacement, which corresponded to stents with an element edge length of 0.10 mm. The third phase of the mesh convergence was to run stented artery models while increasing the mesh density of the artery to minimize variance in the circumferential stresses in the artery. Convergence was assumed when hoop stress and radial displacement values differed by $<4.5\%$ and $<<1\%$, respectively, with increases in mesh density.

To optimize computational resources a non-uniform mesh of the vessel was constructed. The artery was divided into three regions in the axial direction (proximal and distal non-stented segments, central stented region). The mesh within the stented region was twice as dense as the non-stented region, thus allowing for a high mesh density only within

the area of interest. The models were constructed incorporating 20-node hexahedral elements. Due to axisymmetry, only a quarter of the circumference of the artery and stent were modeled to save computational resources.

Results

The stiffer 1Z1 design produced radial displacements that increased in the direction of taper. The net effect is that the vessel assumes the shape of the stent, i.e. the taper is no longer evident in the stented segment. This is illustrated in Figure 3.2, which gives the final radial position of the intima averaged over the azimuth angle (θ-averaged) versus axial position at diastolic pressure. In comparing the radial position plots of the 1Z1 design with the unstented vessel, it can be seen that the increase in radius ranged from over 20% at the proximal (wide) end to near 25% at the distal (narrow) end of the stented region. With the more compliant 2B3 design, radial displacements were similar at both ends of the stent, with gains in radius near 15%; the greatest displacement occurred in the central portion of the stented region, where the increase in radius was greater than 18% (Figure 3.2). Thus, the gradual transition in compliance from stent to artery, a sign of "compliance matching" [37] is evident near the ends of the stent. Differences between stent designs were small in the central stented region, where the stiffer 1Z1 design achieved displacements that were less than 3% greater than those achieved by the more compliant 2B3 design; and large at the distal end of the stented region, where the 1Z1 design achieved displacements that were more than 5% greater than those attained by the 2B3 design. Note that the stent over-sizing of 10% is determined at systolic pressure at the proximal end of the stented segment, while

the aforementioned evaluation is conducted at diastolic pressure - as this would represent a "worst" case scenario, wherein the load bearing on the stent is at a maximum.

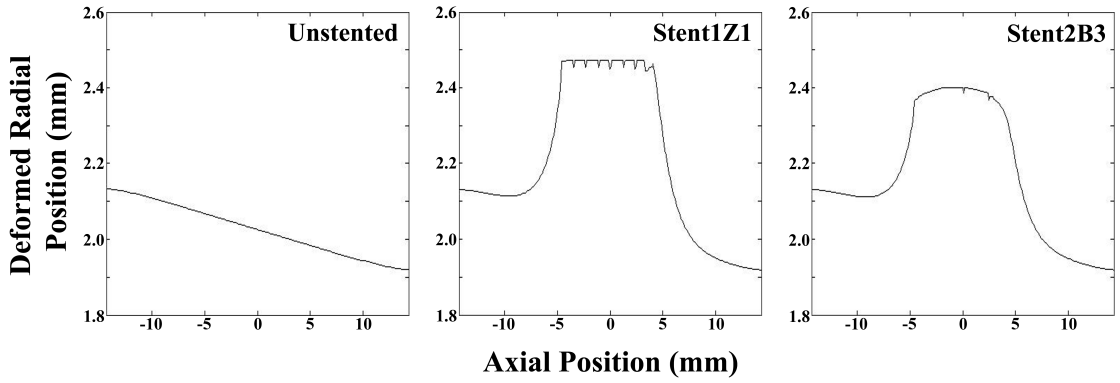

Figure 3.2: Final Radial Position. Deformed radial position values were averaged around the circumference of the vessel at diastolic pressure. With the stiff 1Z1 stent design, the vessel essentially assumes the shape of the stent, i.e. the taper of the vessel is no longer evident through the stented region. With the more compliant 2B3 design a gradual transition in compliance from stent to artery is evident near the ends of the stent.

Examination of the tensile circumferential stresses imposed on the inner surface of the tapered artery model at diastolic pressure reveal that the highly rigid 1Z1 design induced diffuse stresses that covered a broad range. Peak stress values of approximately 700 kPa (>4X larger than the unstented vessel) were observed at the most distal strut (i.e. the narrowest section of the artery), with values >600 kPa covering more than 50% of the stented region (Figure 3.3). The average circumferential stress for all nodal values over the intima of the stented region was approximately 630 kPa for this design. Conversely, stent 2B3 induced stresses that were generally much lower throughout the stented region, with nodal hoop stress values averaging under 530 kPa. High stresses in the 2B3 design were

more focal, localized at areas of mechanical contact between the stent struts and the artery (Figure 3.3). The peak stress for the 2B3 design was approximately 600 kPa (>3.5X larger than the unstented vessel) and was measured on the crowns of the most distal strut. Stress values >600 kPa, covered <<1% of the stented region. Following an approach similar to that described above, intimal circumferential stress values were averaged about the circumference and plotted versus axial location at diastolic pressure (Figure 3.4). Here it is evident that the stresses induced by the stiffer 1Z1 stent increase in a quasi-linear fashion in the direction of taper. While the stresses are not as high with the 2B3 design, stress concentrations and high stress gradients near the stent struts are evident. Stresses associated with the 1Z1 design were 3-4 times higher than those associated with the unstented artery. Stresses associated with the 2B3 design were also high compared to the unstented artery but remained 100 – 200 kPa lower than those associated with the 1Z1 design.

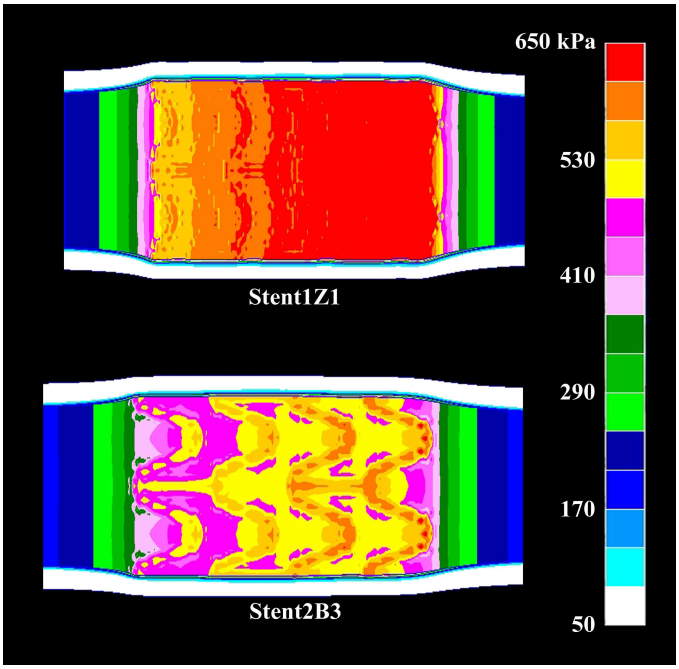

Figure 3.3: Circumferential Stress Distribution. Stent 1Z1 imposed high stresses (> 600 kPa) across larger portions of the artery, whereas stent 2B3 (less rigid) only imposed such high stresses in the most narrow part of the artery. Overall, the 2B3 design imposed stress values that were 100 – 200 kPa lower than the 1Z1 design.

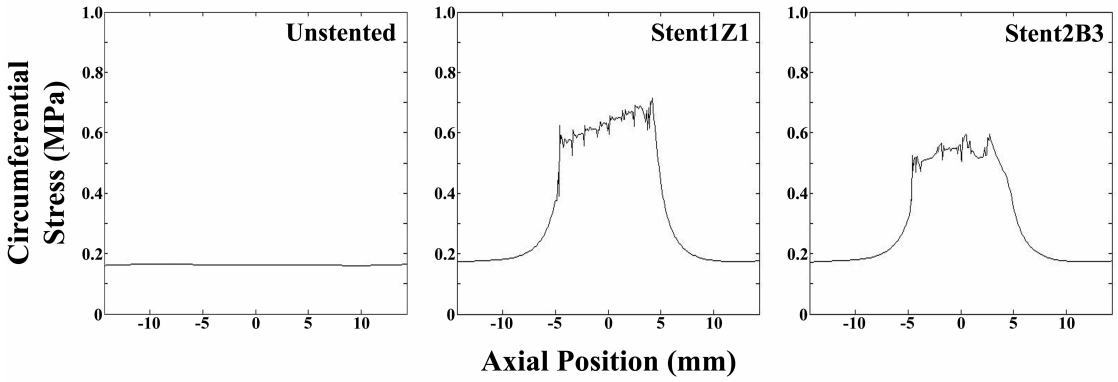

Figure 3.4: Average Circumferential Stress. Intimal artery wall circumferential stress (averaged over the circumference) versus axial position plots reveal the dominance of the 1Z1 stent over the taper resulting in high stresses at the distal end. The less stiff 2B3 stent more naturally follows the arterial taper, resulting in lower stresses. Note circumferential stress values at the intimal are most likely to affect the internal elastic lamina, and restenosis rates have been linked to the disruption of this structure [60, 61].

For both designs there are high stress gradients present in the regions in between ring segments, as well as at the end of the stented regions. For the 1Z1 design, circumferential stress values vary abruptly by 50 – 75 kPa over distances of < 0.1 mm. The 2B3 design has larger differences, but over greater lengths, with stress variations of 80 – 90 kPa over distances of approximately 1 mm. The difference between average stress values at the proximal and distal regions (averaged over 1 mm in length) of the stents, were approximately 90 and 20 kPa for the 1Z1 and 2B3 design, respectively.

Discussion

Improving the biomechanical interaction between implanted devices and the surrounding tissues has the potential to reduce clinical failures. This reduction can be accomplished through implant design changes, as long as the desirable criteria are known. Given the extensive history of human implants of stents, this technology provides an opportunity to establish such criteria. The challenge in this case is to construct appropriate biomechanical models of a wide variety of in vivo conditions in a way that elucidates the important design criteria. The present study focused on the effects of vessel taper on stent/artery interaction.

Based on a previous study in non-tapered, healthy vessels [36], a relatively stiff stent design (1Z1) and a relatively flexible design (2B3) were selected for the present investigation. The stiffer design featured closely spaced rings with small crown amplitudes, while the more flexible design had a larger ring spacing and larger amplitude. In the non-tapered vessels, the stiffer design propped the artery open to a greater degree, but provoked

much higher stresses throughout the artery wall. The more flexible stent also propped the artery open to a clinically successful (although smaller) final diameter, with much lower artery wall stress. The use of finite deformation contact mechanics was crucial, as assuming a perfectly rigid stent would not have given similar results. Furthermore, modeling of truly tapered arteries provides a more complete representation, relative to modeling several non-tapered stented arteries at different degrees of diameter mismatch. That is, while one could perhaps get some idea of the stress field in a tapered artery by constructing two straight artery models whose diameters correspond to the proximal and distal diameters of the tapered artery, the direct effects of tapering on the final stent/artery configuration (e.g. axial dependence of displacement) would remain unknown. Such a strategy would also require a greater number of computational cases to be run. In addition, the stented tapered arteries would have to be modeled to verify that the use of varying degrees of diameter mismatch is an appropriate representation.

Simulating the implantation of these stents in tapered vessels provides further indications that stiffer stents dominate over the artery wall in determining the final geometry and thus the artery wall stress field. The stiffer stent in this case resulted in a nearly constant final lumen diameter in the stented region, despite the natural taper of the artery by 10% along the length of the stent. Given the non-linear, strain stiffening behavior of the artery, the stent had to apply a much greater outward force on the distal end of the tapered vessel, resulting in particularly high artery wall stresses at this region. By contrast, the more flexible stent design followed the natural contour of the artery, with the final deformed geometry still exhibiting some degree of taper. As a result, the stresses at the distal end were much lower.

While there is no known explicit stress level which can lead to an adverse biological response (inflammation, intimal hyperplasia, etc.), design characteristics which minimize stent induced stresses, possibly preventing post procedural complications, should be considered. Currently there are tapered stent designs on the market (e.g. Protégé RX; EV3, Plymouth, MN), but placement of these stents requires an additional degree of accuracy with regard to stent choice to ensure a correct geometric match with the artery wall. Based on our findings, a more flexible stent design can still achieve a clinically successfully final lumen diameter, while reducing the stress induced on the artery wall. This could possibly reduce the chance of post-procedural complications that can be associated with stent deployment. Furthermore, a unique solid mechanical environment occurs in tapered regions of the vasculature that are commonly stented (i.e. carotid, coronary, femoral). These regions see large deformations that result from pulse pressure, myocardial contraction, and limb movements such as hip and knee flexion [62, 63]. Thus, a more flexible stent design would assist in preventing strut fracture, a common cause of clinical failure in stent therapy. It would also be plausible to develop an algorithm, similar to the optimization scheme developed by Timmins et al. [56],to allow for the prediction of the biomechanical environment after stent implantation based on stent design and patient specific vessel geometry. For example, if given adequate input data (i.e. sufficient computational models which encompass the range of parameters of interests), an algorithm that examined parameters such as stent length, stent diameter, and degree of stent or artery tapering could be developed. Such a scheme could provide clinicians with optimal stent designs when tapered geometries are encountered.

From a clinical standpoint, the results presented provide general guidelines for appropriate stent designs that can be used to treat tapered arteries. As most sites of stent deployment (e.g. coronary, carotid, femoral) experience a significant degree of taper, implantation of an unfavorable stent design could cause unnecessary trauma to the artery wall. Such injury could increase the risk of restenosis development or other major cardiac events; with a judicious choice of stent design such complications could be avoided. For example, our results indicate that if confronted with an artery with a high degree of taper, the clinician should choose a stent design that is more compliant and can conform to the natural taper of the artery. This will minimize the stress induced on the artery wall, with the possibility of increasing the success rate of the clinical procedure. The use of a more compliant stent could then serve the intended purpose of a tapered stent, without having to make the additional choice of the appropriate degree of taper for a particular artery.

Limitations associated with this study include the use of axisymmetric artery wall models without a simulated diseased segment. The use of a specific diseased geometry would have limited the applicability of the results. It would have also been more difficult to compare the results from the two different stent designs, as local differences in stress would have been created simply by some portion of the plaque being covered by struts from one design and not another. It was our desire to generate results that have the widest degree of applicability, along with the capability of directly comparing the two stent designs. This comparison is most effectively done with the non-diseased tapered model used here. While residual stresses were not incorporated into the models, the stent induced changes in stress are at least an order of magnitude larger than those associated with residual stress. Therefore,

any influence that this would have on the values presented would likely not affect the relative comparison amongst the two stent designs. The use of relatively short stents is a minor limitation, in that it is not likely that the use of longer stents (with equivalent degrees of tapering in the arteries) would have resulted in any new information. It should also be noted that enforcement of the "glue" contact boundary prevented the stent from translating after "implantation". Due to the high radial displacements achieved by both stent designs, the stents were essentially embedded in the artery, as they would be during balloon inflation, and sliding, if any, would be minimal. Our previous investigations with non-tapered arteries showed that changing the contact condition to allow the stent to slide freely in the artery has a minimal effect on the stress environment [64].

In summary, we have modeled the mechanical interaction of two different stents (one less stiff than the other) with tapered arteries. The rigidity of the stent was found to be an important determinant of final artery wall diameter and stress. More compliant stents should be considered in cases where significant arterial tapering is found.

CHAPTER IV

EFFECTS OF STENT DESIGN AND ATHEROSCLEROTIC PLAQUE COMPOSITION ON ARTERIAL WALL BIOMECHANICS*

Overview

The deployment of vascular stents alters the mechanical environment in the artery, subjecting the artery to extremely high, non-physiologic stresses. These stresses require the artery to adapt and are most likely the cause of the development of neointimal tissue, ultimately resulting in restenosis. The primary goal of this investigation was to examine the solid mechanical effects of varying stent design and atherosclerotic plaque stiffness on the biomechanical environment induced in a diseased artery wall model. Computational modeling techniques were employed to investigate the final radius of the lumen and artery wall stresses after stent implantation. Two stent designs were investigated (one stiff and one less stiff). The stenotic artery was modeled as an axisymmetric, diseased vessel with a 20% stenosis by diameter. The material properties of the diseased tissue in the artery models varied. Atherosclerotic plaques half as stiff (0.5X), of equal stiffness (1.0X) or twice as stiff (2.0X) as the artery wall were investigated. Results revealed that final radial position was dependent on stent design, and that the stiffer stent deformed the artery to approximately a 10% greater radial position than the more compliant design. Alternatively, circumferential

* Reprinted from Journal of Endovascular Therapy, Vol. 15(6), L.H. Timmins, C.A. Meyer, M.R. Moreno, J.E. Moore, Jr., Effects of Stent Design and Atherosclerotic Plaque Composition on Arterial Wall Biomechanics, pp. 643-654, 2008 with permission from the Journal of Endovascular Therapy.

stress levels were shown to be dependent on both stent design and plaque material properties. Overall, the stiffer stent subjected the artery wall to much higher stress values than the more compliant design, with differences in peak values of 0.50, 0.31, and 0.09 MPa for the 2.0X, 1.0X, and 0.5X stiff plaques, respectively. Evidence suggests that a judicious choice of stent design can minimize stress while maintaining a patent lumen in stenotic arteries. If confronted with a rigid, calcified plaque, stent design is more important, as design differences can impose dramatically different stress fields, while still providing arterial patency. Alternatively, stent design is not as much of an issue when treating a soft, lipid-laden plaque, as stress fields do not vary significantly amongst stent designs.

Introduction

The implantation of a balloon expandable stent to treat stenotic atherosclerotic disease imposes very high, non-physiologic stresses on the artery wall. The initial acute injury is caused by balloon dilatation, which is performed at pressures approaching two orders of magnitude higher than normal physiologic pressure. Initial injuries and responses thereto include endothelial denudation, thrombus deposition, and monocyte aggregation [27]. Further chronic injury provokes the processes associated with restenosis (i.e. inflammation, smooth muscle cell/fibroblast proliferation, and matrix protein deposition). In cases where the artery is unable to adapt or remodel successfully to this newly imposed biomechanical situation, restenosis results.

Clinical studies have indicated the potential importance of stent design in triggering the restenotic process. Kastrati et al. [29] reported binary restenosis rates varying from 20%

to nearly 40% among balloon-expandable stainless steel designs. More recently, in-stent restenosis rates of bare metal versions of modern drug-eluting stents have been shown to vary from 36.3% for the Bx Velocity stent (Cordis) in the SIRIUS clinical trial to 26.6% for the EXPRESS stent (Boston Scientific) in the TAXUS-IV clinical trial [21]. These clinical studies indicate the importance of stent design, but provide little information that can be used to improve stent design and the biomechanical environment that they impose. In addition, the recent advancements of anti-restenotic strategies such as drug-eluting stents aim to counteract the negative effects of the high wall stresses imposed on the artery. However, complications such as late thrombosis [65] and the lack of long term success in peripheral arteries [66] still limit this technology. A further investigation into the artery wall stresses induced by stent implantation, and the pursuit of strategies to minimize them could reduce restenosis rates for both bare metal and drug-eluting stents.

The geometric configuration of the stent struts is a principal determinant of the subsequent chronic stresses in the artery wall. Since stresses cannot be directly measured even in ideal circumstances (they are inferred from separate measurements of force and area), researchers have turned to computational modeling, such as the finite element method (FEM), to estimate the artery wall stresses induced by different designs. In the construction of such models, one must carefully consider the nature of the artery wall model, as modeling is limited by the material models used to characterize arterial and stenotic tissues. Using high-resolution imaging and digital reconstruction techniques, it is possible to model diseased segments of specific patients. Such imaging methods have been utilized to investigate the effects of commercially available stent designs on the mechanical

environment within diseased iliac arteries comprised of numerous different vascular tissues, each with unique mechanical properties [44, 67]. These studies indicate that specific stent designs can be assessed to determine their mechanical performance on "virtual" patients before implantation. While such studies demonstrate the importance of stent design, they are somewhat limited to that particular patient's lesion geometry and its composition. Further advancement in imaging techniques – optical coherence tomography, intravascular ultrasound, magnetic resonance imaging – have allowed better characterization of the histological components of atherosclerotic plaques and have considerable potential to better assist in the development of patient specific modeling [68].

An alternate strategy is to construct more "generic" models of the artery wall that are more suitable for delineating differences between stent designs. Generic models of the artery wall (with or without diseased segments), while appearing less relevant to the clinical application, have some advantages in the investigation of the effects of stent design. The applicability of the findings extends beyond a single patient, and one can test stent design variations without having to vary deployment parameters such as the rotational position of the stent relative to the specific plaque geometry. Lally et al. [45] analyzed the biomechanical interaction between both the S7 (Medtronic) and the NIR (Boston Scientific) stent designs in an idealized stenosed coronary artery. Artery and plaque material properties varied and were determined by curve fitting data from the mechanical testing of human femoral artery and calcified plaque tissue, respectively. Results concluded that the S7 stent design induced lower stresses on the artery wall as compared to the NIR design, which correlates well with observed clinical restenosis rates. Bedoya et al. [36] used a straight, non-

diseased model of the artery wall to investigate the effects of varying the design parameters of a ring segment stent on artery wall stress and radial support. It was found that stents with large axial spacings and ring amplitudes imposed less stress on the artery wall. The final lumen diameter was approximately the same for the different designs.

The inclusion of more realistic geometric features such as diseased segments would improve the clinical relevance of these studies. However, there are some key issues that arise in this pursuit. First, one must specify the mechanical properties of the plaque. Histological examination has demonstrated the heterogeneity of atherosclerotic plaques. In addition, mechanical testing has shown that the mechanical properties of the various tissue components (fatty streaks, lipid pool, fibrous cap, and calcium deposits) span orders of magnitude [69]. In particular, one investigation that examined the stress-relaxation response of various atherosclerotic plaque specimens (i.e. highly calcified, fibrotic, lipid-laden specimens) reported elastic moduli values ranging from 40 to 3300 kPa [70]. Generally, atherosclerotic plaques are considered to be either less stiff than a typical artery wall, as would be the case in lipid-laden plaques, or much stiffer than the artery wall, as occurs with increased calcification. As Hayashi [71] reported in a review of experimental studies of the material stiffness of diseased arterial tissue, 36% of the studies showed in an increase in elastic modulus, 29% showed a decrease, and 36% showed no significant chance when compared to non-diseased tissue. Such variations in tissue material properties are likely to affect the biomechanical environment (wall stresses, radial deformation) induced by the implanted stent. Additional issues include the choice of plaque geometry (i.e. concentric, axisymmetric). Choosing to vary both plaque material properties and geometry in addition to

varying the stent design is not feasible, as the number of simulations required to cover the physiologic parameter space quickly becomes overwhelming.

The goal of this study is to determine the effects of varying stent design parameters on the final radial position achieved and the stress induced in a diseased, axisymmetric artery wall models. The focus in interpreting the results has been placed on the effects of varying the mechanical properties of the plaque, since this is most likely to impact the predicted stresses, as well as the final lumen diameter. Thus, we have chosen to investigate plaques that are less stiff (0.5X), of equal stiffness (1.0X), or stiffer (2.0X) than the artery wall. The results of this study and others in the literature provide a variety of bases for improving stent design overall, and perhaps more importantly, provide guidance for lesion-specific stenting.

Methods

A computational approach was employed to determine the biomechanical impact of varying stent design in stenotic vessels whose atherosclerotic plaques ranged in material stiffness. The two stent models, selected from the extreme designs identified in Bedoya et al. [36], are intended to represent designs that have high and low radial rigidity. The multiple step computational simulations began with over-expansion of the stenotic vessel, followed by translation of the stent into the diseased region, and finally reduction of the vessel internal pressure to systolic, followed by diastolic. The mechanics of contact between the two elastic bodies (stent and vessel) was modeled, which determined the final geometric configuration of the combined structure. The stent geometry was specified in the already expanded state with uniform mechanical properties and no internal stresses. The artery wall model features

non-linear, strain-stiffening properties, and the plaque is specified as being stiffer, less stiff, or having the same stiffness of the artery wall in separate models.

Model Geometry. The 3D stent geometries investigated in this study have been previously reported [36]. Briefly, stent models were defined by three parameters: strut **S**pacing, **R**adius of curvature, and axial **A**mplitude (**SRA**). The two stent designs modeled were those that imposed the highest (stent 1Z1) and lowest (stent 2B3) values of circumferential stress and radial displacement in the aforementioned investigation. Stent 1Z1 is characterized by a strut spacing of 1.2 mm, radius of curvature of 0 mm, and amplitude of 0.6 mm, while stent 2B3 is described by parameter values of 2.4 mm, 0.3 mm, and 1.8 mm, respectively (Figure 4.1). Stent designs had a deployed outer radius of 2.475 mm, approximately 10% larger (1.1 to 1.0 stent-to-artery ratio) than the intimal radius of a healthy region (white region in Figure 4.2) of the vessel at systole, and a constant strut thickness of 100 μm. These geometrical values agree with manufacturers' recommendations and common stenting practice [47]. Due to the repeating nature of ring segments in stent designs, and the fact that any edge effects have dissipated within the first ring segment, the biomechanical environment within the middle section of the stent model is equivalent to that of any two inner rings of a full length stent. Thus, only a portion (9 mm in length) of a full length was modeled; 8 ring segments for stent 1Z1 and 4 ring segments for stent 2B3. The near-periodic pattern of the resulting stresses near the middle rings supports the validity of this assumption. The material of the stent was modeled as 316L stainless steel (Young's Modulus (E) = 200 GPa, Poisson's Ratio (v) = 0.3).

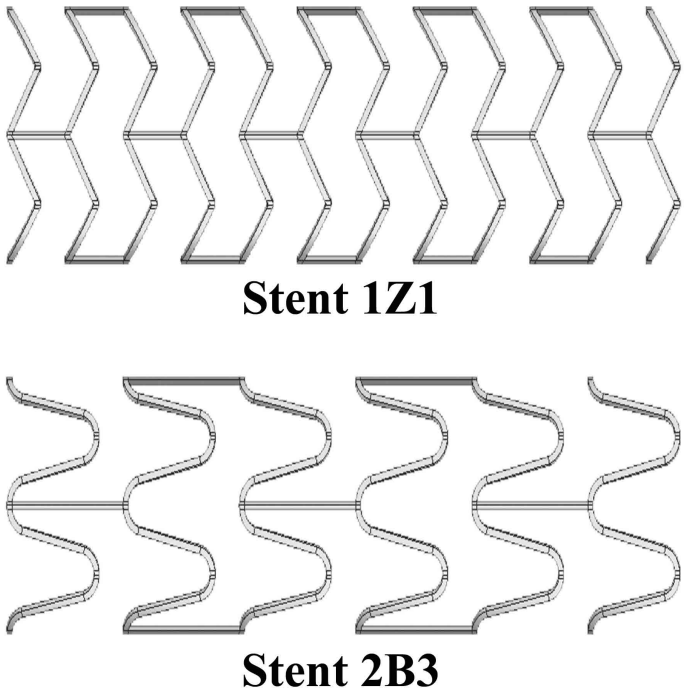

Figure 4.1: Stent Design Geometries. Illustrations of the stent designs employed in this investigation. The 1Z1 design has a high radial stiffness, and induces high radial displacement and stress on the artery wall. The 2B3 design has a lower radial stiffness and places less radial displacement and stress on the artery wall [36].

The diseased artery was modeled as a generalized, stenotic vessel characterized by a 18 mm long cylinder with a localized, concentric atherosclerotic plaque (Figure 4.2). The plaque was designed to be a maximum stenosis of approximately 20% by diameter at diastolic pressure (i.e. equivalent to a residual plaque burden of 20% after stent implantation). The model is representative of a tighter stenosis that has been balloon-expanded and fractured, and agrees with angiographic results from post-dilation of clinically significant stenoses [72]. Note that this investigation is focused on the biomechanical environment after the balloon has been deflated and retracted leaving the stent at its

expanded diameter (i.e. focus is placed on the chronic stent induced stress). Thus, further complexities associated with the plastic deformation of the stent and possible plaque fracture during expansion are avoided. Also, the requirement to have the stenoses hold approximately the same shape at physiologic axial stretch and diastolic pressure meant that each had a different unloaded geometry (Figure 4.3).

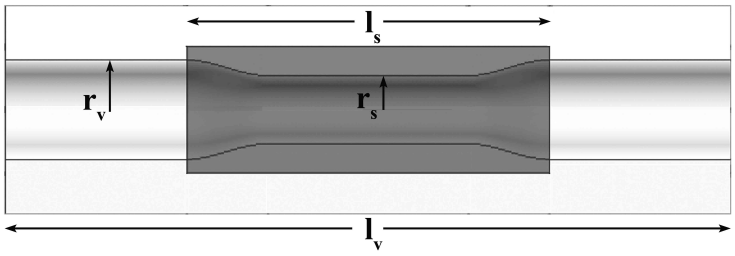

Figure 4.2: Stenotic Artery Geometry. Undeformed geometry of the diseased models used in this investigation; vessel radius (r_v), stenosis radius (r_s), vessel length (l_v), stenosis length, (l_s). The white region denotes healthy arterial tissue and the dark region denotes the atherosclerotic plaque. The stent was "deployed" only in the diseased region.

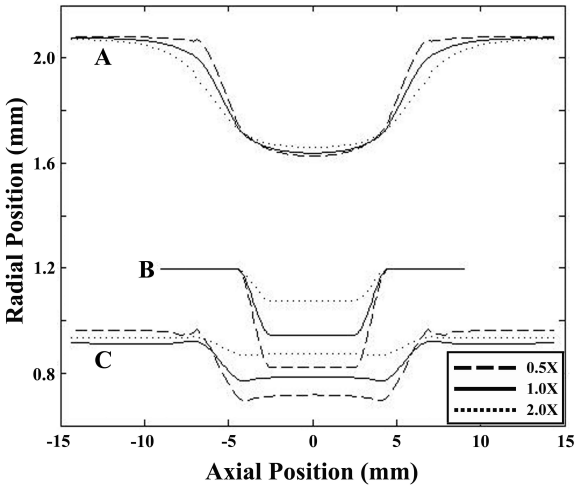

Figure 4.3: Unloaded Stenosis Geometries. Due to the variation in plaque material properties, the unloaded geometries of the stenosed arteries varied – unloaded (B), stretched (C), stretched and pressurized (80 mmHg, A) – to ensure that each model had the same radial dimensions at diastolic pressure (~20% stenosis by diameter). 0.5X – dashed, 1.0X – solid, 2.0X – dotted.

The material properties of the artery have been previously utilized in computational models [36, 56]. The same form of the strain energy function (SEF) was used to describe the plaque material properties. The plaque stiffness was adjusted by scaling the constants in the SEF. Atherosclerotic plaques 0.5, 1.0, and 2.0 times as stiff as the vessel were modeled in this investigation. The effect of scaling the constants in the SEF is seen in Figure 4.4. The range of plaque of mechanical properties investigated fall within that of experimental data for atherosclerotic tissue [69], and other computational studies of stented diseased vessels [73].

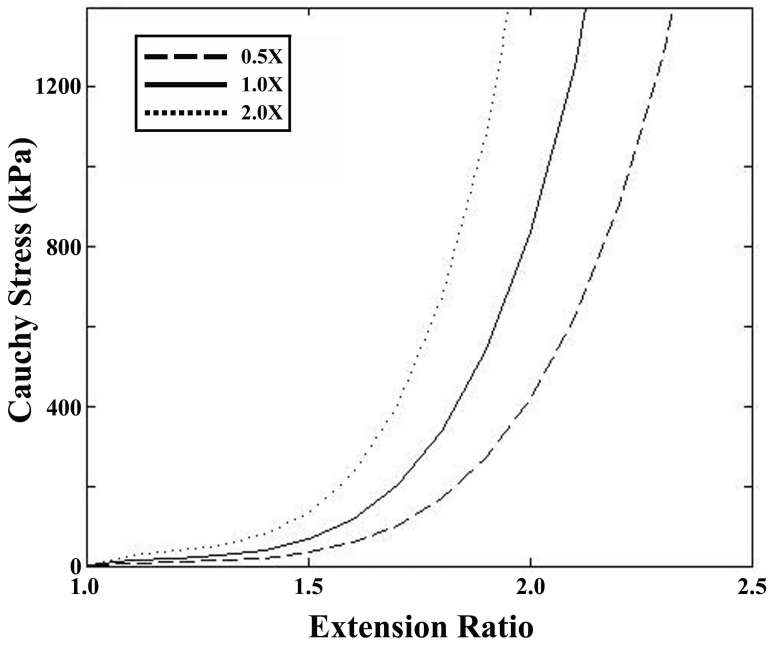

Figure 4.4: Artery Wall and Plaque Material Responses. Material responses used to describe the arterial wall and atherosclerotic plaque. The SEF constants were scaled to model plaques that were half as stiff (0.5X, dashed), of equal stiffness (1.0X, solid), or twice as stiff (2.0X, dotted) as the artery wall.

FEM Simulations. The 3D FEM models were constructed using MSC.Patran 2005 r2, while MSC.Marc 2005 v1 was employed as the non-linear solver (MSC Software, Santa Ana, CA). Displacement, pressure, and contact boundary conditions were applied in multiple stages (fixed load increments). Initially an axial stretch ratio of 1.59 was applied to the vessel to simulate in vivo longitudinal tethering. A pressure was then applied to the inner surface of the vessel (varied between 660 – 1000 mmHg depending on plaque material properties), inflating the inner radius to a position larger than the outer radius of the over-sized stent. Note that these over inflation pressures are not directly related to balloon expansion, but rather were required to ensure proper apposition of the strut to the artery wall. The stent was then translated in the axial direction until the midpoints of the stent and artery overlapped. The inner pressure was then reduced to systolic value (120 mmHg), and finally diastolic (80 mmHg). Throughout the simulation constraints were applied to both the artery and stent symmetry edges to restrict rotation and only allow in-plane deformations.

To optimize computational resources, only a quarter of the circumference of the stent and artery were modeled. Furthermore, a non-uniform mesh of the vessel was constructed in which the stented region was twice as dense as the non-stented region. The models are discretized using 20-node hexahedral elements, with total element numbers of 922, 938, and 19,320 for stents 1Z1, 2B3, and the vessel, respectively. Displacements were interpolated using quadratic Lagrange functions and contacting bodies were defined with C^2-continuous Non-Uniform Rational B-Splines surface (NURBS). The mesh was considered converged when circumferential wall stress and deformed radial position values at diastolic pressure

differed by <2% and <1.25%, respectively, while doubling the mesh density of the stented region in all principal directions (r, θ, z).

Evaluation Methods. To examine differences amongst stent designs, as well as the material properties of the plaques, the biomechanical (radial displacement, wall stress) impact of stent deployment in stenotic arteries was analyzed. From a clinical standpoint, radial position is of utmost importance for stenting procedures, as sufficient displacement is required to restore blood flow to downstream tissues. As a measure of each stent design's ability to maintain a patent lumen, the deformed radial position achieved by each design on the various plaque properties was evaluated. As studies have shown that arteries remodel in response to increased levels of blood pressure (i.e. hypertension) [74] and arterial cellular components respond to varying levels of cyclic stretch [75], it is thought that changes in the normal physiologic mechanical environment result in a biological response that aims to restore mechanical values (wall stress, fluid shear stress) to homeostatic levels. Thus, it is hypothesized that neointimal growth is a direct result of the extremely high, non-physiologic stresses induced by the stent onto the artery wall. Circumferential (hoop) stress values in the artery wall were compared to two representative measures of wall stress. Using analytical techniques (described below) values at the original location of the intima were examined, as it is a preferred location to detect biomechanical differences that may be related to restenosis due to its immediate proximity to the internal elastic lamina (IEL). Disruption of the IEL has been shown to greatly increase the risk of restenosis development [60, 61]. Average stress values through the thickness were also analyzed; such values can be compared to Law of

Laplace values, to examine the impact of stent deployment on the averaged stresses induced on the artery wall.

Results from the FEM simulations are reported as nodal values corresponding to radial displacement and circumferential stress at diastolic pressure. These values were used for post-processing calculations. Radial displacement values were used along with undeformed radial locations to determine final lumen position after "implantation" of the stent. Deformed radial position values of the intimal surface were averaged around the circumference (θ-averaged) along the length of the deformed artery. Circumferential stress fields, from each FEM simulation, consisted of average circumferential stress plots at the location of the IEL. Circumferential stress values at the IEL were determined by quadratic interpolation from nearby nodal values (i.e. nodes shared the same undeformed circumferential and axial location). As described above, the interpolated values were averaged around the circumference along the length of the deformed artery.

Results

The final inner radius of the stented artery was found to depend strongly on the stent design, but very weakly on the plaque properties. Deployment of the stiffer stent (1Z1) resulted in a final inner radius of approximately 2.47 mm in the stented region for all plaque material properties, while deployment of the more compliant stent (2B3) resulted in a final radius of approximately 2.27 mm (Figure 4.5). The inner radius of the unstented artery outside the plaque is 2.07 mm at diastolic pressure, so both stents would be considered clinically successful. Recall that both stents were sized to be 10% larger than the systolic radius of the artery outside the plaque. Note also that there was a slight inward motion near the edges of the stent with the stiffest plaque and more compliant stent. This occurs due to the stiff plaque pushing inward at the edges of the stent; the part of the structure with the least radial strength. The final radius in the stiffer stent was nearly uniform along the length of the stent, with sharp drop-offs at the ends. In the more compliant stent, the final radius tapered off more gradually at the ends.

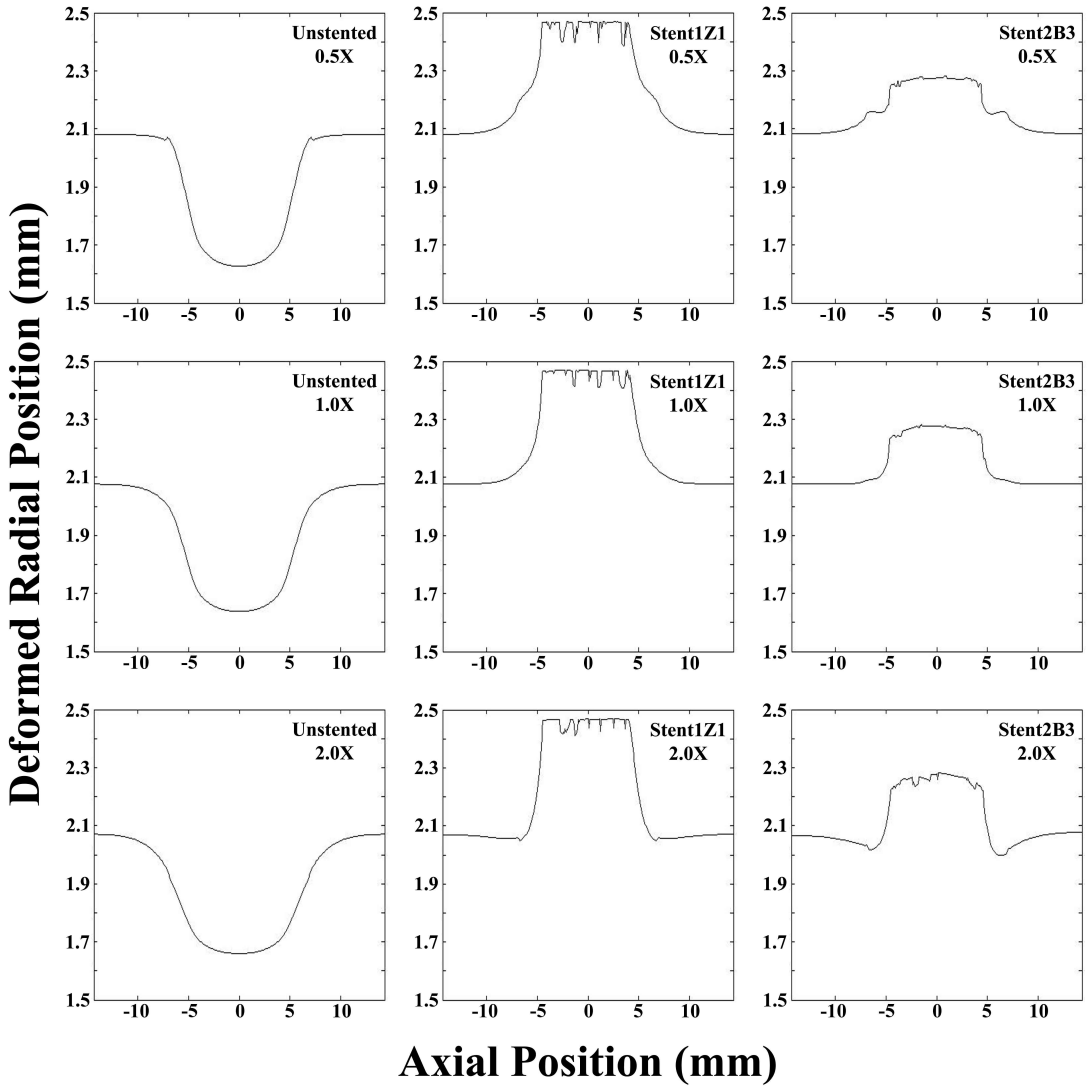

Figure 4.5: Final Inner Radial Positions. Deformed radial position values were determined by averaging around the circumference of the vessel at diastolic pressure along the vessel axis. It was determined that final radial position was only dependent on stent design and not plaque material properties. The stiffer (1Z1) and more compliant (2B3) stent designs propped the artery open to approximately 2.47 mm and 2.27 mm, respectively, despite the change in plaque material properties.

Circumferential stress values at the original arterial intima, representative of the location of the IEL, were higher in the presence of a stiffer plaque and were dependent on stent design. Examination of the peak stress values (θ-average) in the stented region revealed that the largest differences in circumferential stress attributable to stent design were observed with the stiffest plaque. The peak circumferential stress value in the stented region was 1310 kPa with the 2.0X plaque and the stiffer stent (1Z1), while it was 803 kPa with the more compliant stent (2B3) and the same plaque (Figure 4.6). With the 1.0X plaque, the peak circumferential stress was 750 kPa with the stiffer stent (1Z1) and 443 kPa with the more compliant stent (2B3). The smallest differences between stent designs were observed with the 0.5X plaque. In this case, the peak circumferential stress was 262 kPa with the stiffer stent (1Z1) and 158 kPa with the more compliant stent (2B3). As with radial displacement, the circumferential stress field was more uniform along the length of the stiffer stent, while it tapered off more gradually at the edges of the more compliant stent.

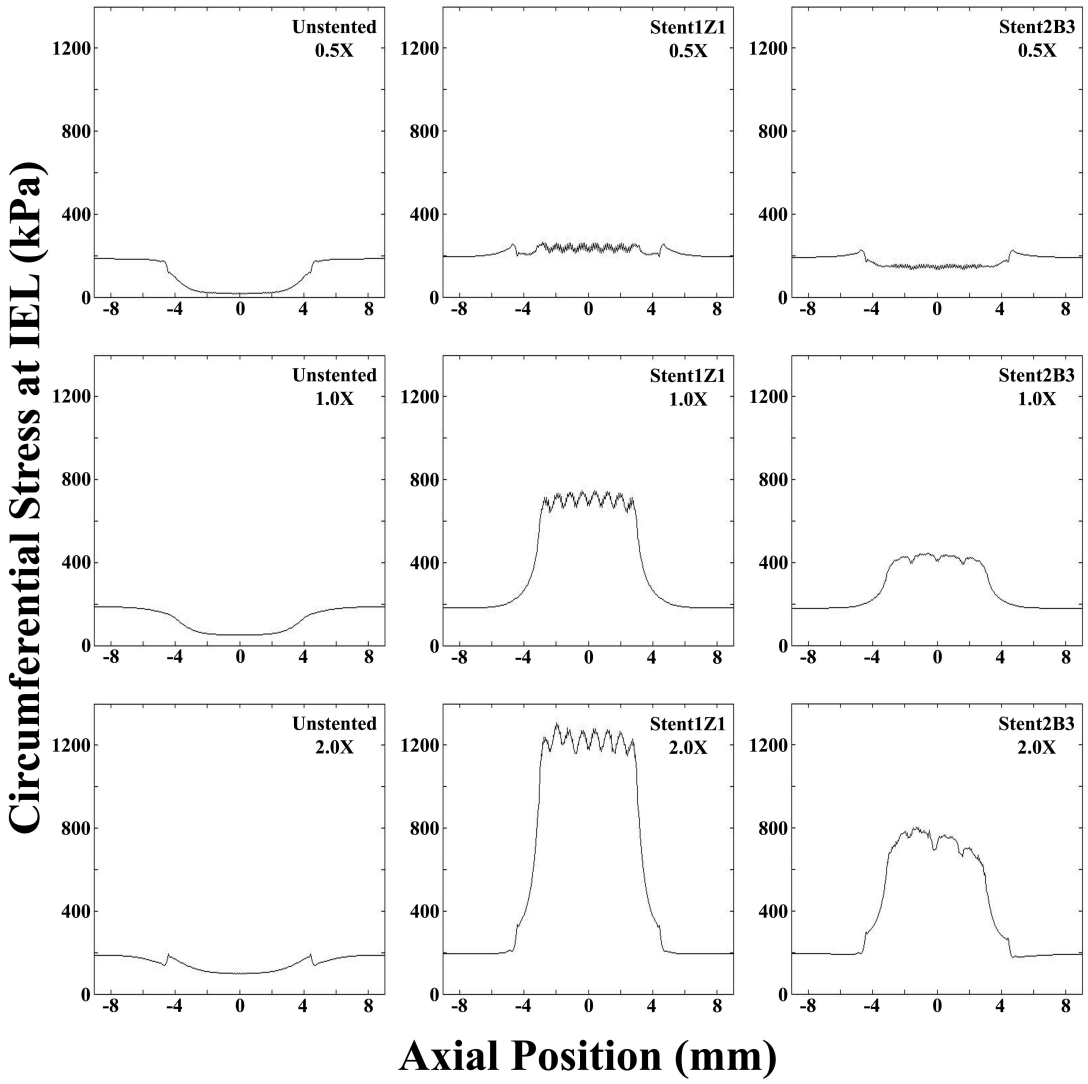

Figure 4.6: Average Circumferential Stress at Location of Internal Elastic Lamina (IEL). Artery wall hoop stress values (averaged over the circumference) at the IEL were dependent on both stent design and plaque material properties. Highest stress values were observed for the stiffest plaque (2.0X) and most rigid stent (1Z1), while the smallest values were seen for the least stiff plaque and more compliant stent design (2B3). Note high circumferential stress values at the IEL are most likely to disrupt this structure, provoking neointimal growth, leading to restenosis [60, 61].

Mean (averaged through the thickness) circumferential artery wall stress were substantially higher for the more rigid stent (1Z1) design, and were an order of magnitude

higher than that predicted by Law of Laplace for an unstented artery (both healthy and diseased). As a reference, Law of Laplace predicts a mean stress value of 35.5 kPa for the healthy region of the vessel, whereas a value of 22.0 kPa was calculated for the stenotic region, both at diastolic pressure. In the presence of the more rigid stent (1Z1), mean stress values in the middle 50% of the stent (i.e. the region where the ring segments would repeat in a full length stent) were 465, 425, and 411 kPa, for the 2.0X, 1.0X, and 0.5X plaque stiffnesses, respectively. The more compliant stent (2B3) design induced considerably lower mean stress values, with values of 283, 255, and 257 kPa for the plaque stiffnesses of 2.0X, 1.0X, and 0.5X, respectively.

The range of circumferential stress experienced by the IEL around the central portion of the stented plaques was much higher with the stiffer plaques, and depended on stent design. The maximum circumferential stress typically occurred adjacent at the point where the struts contacted the plaque, while the minimum circumferential stress occurred at points removed from the strut locations. Within the middle 50% of the stented length, circumferential stress values ranged from 1160 to 1310 kPa, with an average value of 1230 kPa, for the more rigid stent (1Z1) and stiffest 2.0X plaque (Figure 4.6). In the case of the more compliant stent (2B3) design in the 2.0X plaque, the stress values ranged from 663 to 803 kPa, with an average of 746 kPa. Decreasing the plaque stiffness resulted in decreases in both the range of circumferential stresses and the average induced at the location of the IEL. With the 1.0X plaque stiffness, circumferential stress values of 662, 749, and 708 kPa corresponding to the minimum, maximum, and average stress values, respectively, were observed for the 1Z1 stent design. The corresponding values for the 2B3 design in the 1.0X

plaque stiffness were 390, 443, and 425 kPa, respectively. For the least stiff plaque (0.5X) models, both the range of circumferential stresses induced, and the average were lower and more similar between the two stent designs. Stress values of 209, 262, and 237 kPa for the minimum, maximum, and average values, respectively, were found for the rigid (1Z1) design, whereas values of 132, 158, and 147 kPa were observed for the more compliant stent (2B3) design.

Examination of the stent edges revealed very abrupt changes in circumferential stress over small distances (i.e. high stress gradients). For the case of the stiffest plaque (2.0X) and stent (1Z1), average circumferential stress values varied rapidly by approximately 748 kPa over distances of <1.0 mm. For the same plaque stiffness, the more compliant stent (2B3) design had stress changes of approximately 341 kPa over the same distance. The same trend held for the 1.0X case, where the stiff stent had larger changes (407 kPa) than the more compliant design (154 kPa) over a distance of <1.0 mm. The least stiff plaque (0.5X) saw the smallest difference between designs, with circumferential stress changes of 57.6 and 4.45 kPa for the stiffer (1Z1) and more compliant (2B3) designs, respectively, over <1.0 mm distances.

Discussion

The biomechanical implications of stent implantation include dramatic changes in artery wall stress and flow patterns. While these effects in general are consequences of the clinical need to prop open the artery, there are strategies that designers and clinicians can undertake to minimize the deleterious role biomechanics can play in the restenosis process.

Studying the effects of stent design on artery wall stress, followed by an informed choice of the most appropriate stent design for a particular plaque, is one such strategy. We have investigated the effects of stent design on stresses in the walls of arteries with plaques representative of the variety encountered clinically (less stiff, equal stiffness, or more stiff than the artery wall). In order to preserve the general applicability of the results, the plaque geometries were rather "generic" in nature (i.e. axisymmetric). The results indicate that stent design and plaque composition combine to determine stress at the location of the IEL, and that a judicious choice of stent design can minimize stress at this location while maintaining arterial patency.

In all cases studied here, the stents were successful in establishing a patent lumen, as values of final percent stenosis after the implantation agree with clinical data [76]. The degree to which the artery was propped open was approximately constant for a given stent design, with a negligible degree of dependence on the plaque properties. The stiffer stent resulted in a larger final diameter than the more compliant stent, but the differences were small and not likely to result in a clinically significant difference in acute blood flow restoration. In the case of the stiffest plaque and most compliant stent, there was a slight inward motion of tissue at the edges of the stent. This highlights the importance of insuring that the stent is of a sufficient length.

In contrast to the results for deformed radial position, the stress in the artery wall depended on both stent design and plaque properties, with the differences between stents being more pronounced for the stiffer plaques. It should be noted that there is no explicit stress level (value) known to lead to an adverse biological response (inflammation,

neointimal hyperplasia, etc.). Stress values at the level of the IEL, at diastolic pressure, were as much as 1310 kPa (1Z1 design, 2.0X plaque stiffness), or approximately 6.72 times the stress at the IEL in the normal artery wall. Peak stresses at the IEL were much lower for the softest plaque (0.5X), and both peak and average stress values only differed by 104 and 90.1 kPa, respectively. Thus for a relatively soft, lipid-laden plaque, the more rigid stent design would be more preferable to implant, as there is not a considerable difference in the stress subjected onto the artery compared to the other design and a much larger radial displacement. Alternatively, for a rigid, calcified plaque the more compliant stent design would be preferred, as it would still provide sufficient radial support, while greatly reducing chronic injury to the artery wall. In all cases with the stiffer stent, the entire stented region was subjected to a relatively uniform high stress. With the more compliant stent, the stress tapered off at the ends (a sign of "compliance matching," see Berry et al. [37]), and there was a greater degree of heterogeneity around the circumference at a given axial location. While it is certainly likely that the value of the maximum stress is the principal determinant of IEL rupture, chronic average stress values in the stented region could also lead to adverse biological responses. Whether maximum of average stress values are more important in the development of neointimal tissue remains to be elucidated. It is also possible that local gradients in stress trigger cellular proliferation to a degree that influences restenosis.

We have limited the presentation of stress results to the approximate location of the IEL because the disruption of this structure has been linked to a greater risk for restenosis [60, 61]. In general, stress varies from very high values at the inner wall to much lower values at the outer wall. This is due to two factors. First, the expansion of an incompressible

cylindrical structure results in a higher strain at the inner wall than at the outer wall, with the difference related to the local wall thickness. Second, the non-linear (strain stiffening) behavior of the artery wall material essentially amplifies the strain difference, so that the stresses at the inner wall are higher than those at the outer wall by a greater degree of proportionality than with strain. On the surface of the plaque, where wall thickness is highest, extremely high circumferential stresses (on the order of 2.5 MPa) were predicted in our model, but not reported in the results. Such high stresses are likely to result in plaque fracture, and this is indeed a common observation in plaques that have been subjected to balloon angioplasty alone [77].

As with any modeling study, there are a number of limitations that should be recognized in the application of these results. The most obvious is the assumed symmetry and homogeneity of the plaque and artery. Any effort to model a plaque with a more realistic geometry must address the basic question, “which plaque?” There is of course a tremendous variety of plaque geometries, just as there is a tremendous variety of plaque mechanical properties. Therefore, we have chosen to study variations in plaque mechanical properties, sacrificing specificity in geometry in favor of more generality in the applicability of the results. Further studies of the effects of plaque geometry are certainly warranted, but inherently much more computationally demanding than the work presented here in terms of numbers of models required and the need to model a full circumference of stent and artery. It was assumed that only elastic deformation occurred in all structures (artery, plaque, and stent). Therefore, we have chosen not to include plaque fracture or damage in our models, so the stresses predicted in the plaque itself may not be reliable (i.e. fracture would likely occur

at much lower stress values). While there are studies that have investigated atherosclerotic plaque fracture [78], it is an event that is highly dependent on plaque geometry and composition and thus highly patient specific.

We have also limited our study of plaque properties to a range indicative of 0.5X to 2.0X the native artery stiffness. It is likely that, when assessed with appropriate finite deformation models, a wider range of plaque properties could be identified, yet the stiffness values examined are within the range of available experimental data [41], as well as other computational studies [73]. The range of stent designs could also be extended. In both cases, it is likely that the general trends exhibited here (higher stress with stiffer plaques, stiffer stents, etc.) would hold.

In addition, the stent expansion process was not modeled, so any material inhomogeneities that could result from plastic deformation are not taken into account (i.e. it is assumed that the homogeneous material properties of the stents are identical upon initiation of contact with the artery wall), although it is also not likely to change the trends. It should also be noted that vascular stenting causes non-laminar flow patterns to develop within a stented artery, as both computational and experimental studies have shown [42, 43, 79]. While only the solid mechanical environment was investigated in this study, both solid and fluid mechanical factors should be considered when optimizing stent design and improving the long-term patency of these devices.

Conclusion

In this study, variations in stent design were investigated to determine their impact on the biomechanical environment in diseased vessels with varying plaque material properties. It was determined that the position of the lumen after stent deployment was only dependent on stent design, with the stiffer stent (1Z1) propping the artery open to a larger radial value. Also, the displacement field was much more uniform with the stiffer stent, whereas the more compliant design (2B3) revealed inward motion at its edges. Alternatively, the circumferential stress values were dependent on both stent design and plaque material properties. Higher stresses were observed with the stiffer plaque, while comparison amongst designs showed the stiffer stent inducing higher stress values than the more compliant design across all plaque material properties. The smallest difference between stent designs occurred with the least stiff plaque. Furthermore, abrupt changes in stress values were observed at the stent edges, with larger changes being observed with the stiffer stent.

It is thought that regions of high artery stress are the most susceptible to an adverse biologic response. Thus, any chance to minimize such stresses, while still maintaining arterial patency, should be strongly considered. In the case of rigid, calcium-rich atherosclerotic plaques, the more compliant stent design (i.e. large strut spacing (h), radius of curvature (ρ), and axial amplitude (f)) would be preferable in order to reduce unnecessary chronic trauma to the artery wall and still provide adequate radial rigidity to restore blood flow. When approached with softer, lipid-laden plaques, a more rigid stent design (i.e. small strut spacing (h), radius of curvature (ρ), and axial amplitude (f) could be implanted, since either design induces a similar stress field. Such “general” design guidelines can be applied

to interventional procedures with commercially available designs. Further advancements in imaging modalities and a more thorough investigation of the mechanical properties of diseased tissue will assist in designing stents for individual patients (i.e. lesion specific stenting).

CHAPTER V

INCREASED ARTERY WALL STRESS POST-STENTING LEADS TO GREATER INTIMAL THICKENING

Overview

Since the first human procedure in the late 1980's, vascular stent implantation has been accepted as a standard form of treatment of atherosclerosis. Despite their tremendous success, these medical devices are not without their problems, as excessive neointimal hyperplasia can result in the formation of a new blockage (termed restenosis). Clinical data have suggested that stent design is a key factor in the development of restenosis. In addition, computational studies have indicated that the biomechanical environment is strongly dependent on the geometrical configuration of the stent, and therefore possibly involved in the development of restenosis. In particular, we hypothesize that stents that induce higher stresses on the artery wall lead to a more aggressive pathobiologic response, as determined by the amount of neointimal hyperplasia. Therefore, the aim of this investigation was to examine the role of solid biomechanics in the development of restenosis. A combination of computational modeling techniques and in vivo analysis was employed to investigate the pathobiologic response to two stent designs that impose greater or lesser levels of stress on the artery wall. Stent designs were implanted in a porcine model for approximately 28 days and novel integrative pathology techniques were utilized to quantify the pathobiologic response. Concomitantly, computational methods were used to quantify the mechanical loads that the two stent designs place on the artery. Results reveal a strong correlation between the

stress values induced on the artery wall and the pathobiologic response; the stent that subjected the artery to the higher stresses had significantly more neointimal thickening at stent struts (high stress stent: 0.197 ± 0.020 mm vs. low-stress stent: 0.071 ± 0.016 mm). Therefore, we conclude that the pathobiologic differences are a direct result of the solid biomechanical environment, confirming the hypothesis that stents that impose higher wall stresses will provoke a more aggressive pathobiological response.

Introduction

Despite the technological advances since the first human implantation of a vascular stent, the development of neointimal tissue following implantation of these devices still remains an incessant problem for the treatment of atherosclerosis. Neointimal hyperplasia can ultimately lead to device failure due to the development of a new blockage in the stented region, termed restenosis. Clinical data has indicated the significance of stent design in the formation of neointimal tissue. Restenosis rates in coronary arteries ranging from approximately 20 – 40% for bare metal stents (BMS) have been reported, with the BMS only differing by their geometrical configuration [21, 29]. While drug-eluting stents (DES) have decreased restenosis rates to <10% in coronary applications [21], numerous problems [e.g. late stent thrombosis [65], impaired reendothelialization [65], lack of success in peripheral arteries [66], hypersensitivity reactions [32] and high cost have raised concerns over their exclusive use. Regardless of the failure rates of these devices, in 2006 alone, more than 650,000 percutaneous coronary interventions coupled with stent implantation were performed [5]; this number does not include the number of stent implantations in other areas

of the vasculature (e.g. carotid, renal, femoral). Thus, as vascular stenting is a standard for treatment of occlusive artery disease, and their use is likely to increase, there is an imperative need to increase the success rate of this therapy.

The etiology and biological mechanisms that result from the introduction of a stent into the vasculature have been well documented both in humans and animal models. Edelman and Rogers [27] defined the vascular response to stenting as a four-phase process (thrombosis, inflammation, proliferation, and remodeling) that may or may not result in restenosis development. Previous investigations have indicated that biomechanics plays a key role in each of these pathobiologic stages. Moreover, the biomechanical impact of stents is largely governed by their exact design configuration.

The first phase in the response of the artery wall to stent implantation is thrombus formation. This involves the delivery of platelets to the largely denuded artery wall and stent struts, both of which can be highly thrombogenic surfaces. The degree to which platelets adhere to these surfaces depends primarily on whether or not the local flow field is directed toward or away from the wall [80]. Higher degrees of platelet accumulation have been noted in regions where instantaneous streamlines point toward the wall. One result of this behavior is that in areas where stent struts are very closely packed, and the mainstream of the flow "skims over" the top of the stagnant area in between, platelet adhesion is lowest [81]. Presumably, the delivery of blood-borne inflammatory cells follows similar patterns. Platelets and inflammatory cells can also be triggered into their activated states by stagnant flow patterns [82, 83]. The altered solid mechanical environment following stent deployment also governs the inflammatory and remodeling response. In vivo and in vitro studies have

demonstrated that arterial adventitial fibroblasts migrate to the neointima where they differentiate into myofibroblast and secrete various extracellular matrix proteins [84, 85]. This migratory response is a direct result of the mechanical forces induced on the artery wall following stent implantation. Computational studies have shown that the solid mechanical environment is strongly dependent on stent design. In particular stents that are characterized by a large strut spacing and axial amplitude impose considerably less stress on healthy [36], tapered [86], and diseased artery models [87]. Thus, there is a tremendous body of evidence indicating that stent design plays a significant role in the altered fluid and solid mechanical environments following their deployment, and it is reasonable to expect that the overall mechanical environment affects the long-term patency of these devices. Further information on the effects of specific stent design parameters on in vivo responses and especially the eventual development of intimal hyperplasia would be of benefit in designing more successful implantable devices.

There is a clear role of biomechanics in the improvement of currently available vascular stents and in their future development. It is interesting to note that many DES essentially employ the same design configuration as their BMS counterparts with a drug-loaded polymer coating on the underlying metallic surface (e.g. Cypher and Bx Velocity, Cordis, Johnson & Johnson, Miami Lakes, FL, USA; TAXUS and NIR, Boston Scientific Corp., Natick, MS, USA). These similarities have lead to some concern over the long-term effect of DES following complete elution of the drug. Recently the PAINT trial compared the effectiveness of three geometrically identical stents, two of which were covered with a biodegradable-polymer carrier releasing either paclitaxel or sirolimus [88]. While results

revealed a significant difference in restenosis rates between the two DES when compared to the BMS, there was no significant difference between the two DES. These findings indicate that the difference in clinical restenosis rates observed between commercially available stents [89] might not be a result of the pharmaceutical agents eluted, but rather the differences in their stent designs.

As a means of correlating the biomechanical environment and resulting pathobiological response following stent implantation of various designs, we employed a combination of computational modeling techniques and in vivo analysis to directly assess the role of biomechanics in the development of restenosis. In particular, our objective in this study was to quantify both the solid biomechanical environment and in vivo arterial response of two stent designs that have been shown to impose considerably different mechanical stresses and strains on the arterial wall. Thus, we tested the hypothesis that stents that induce a non-favorable biomechanical environment (i.e. subject the artery to higher non-physiologic stresses) provoke a more aggressive pathobiological response of the artery wall, resulting in a higher degree of neointimal hyperplasia. The results from this investigation will provide insight into the design of vascular stents that reduce the mechanical trauma on the artery wall, and thereby reduce the neointima hyperplasia and increase the success rates of future stent design iterations.

Methods

In order to examine the pathobiologic response to vascular stent designs that induce extremely different biomechanical environments, two stent designs were deployed in a

healthy porcine model. Similar stent designs to those employed in this study were previously investigated using the finite element (FE) method [36, 86, 87] and shown to induce either extremely high or low stresses on the arterial wall; herein, the two designs investigated are denoted as the high-stress and low-stress stent designs, respectively (Fig. 5.1). Computational modeling techniques were used to examine the mechanical loads induced by the two stent designs on a 3-dimensional (3D), healthy, thick-walled, non-linear model of the artery wall. In addition, qualitative evaluation of the pathobiologic response was achieved by utilization of integrative pathology techniques (quantitative micro-CT, histology).

Computational Modeling. The computational modeling techniques have been employed and discussed in detail elsewhere [36, 56, 86, 87]. Briefly, the computer-aided design drawings provided to Laserage Technology Corporation (Waukegan, IL, USA) for cutting of the stents were imported into MSC.Patran (MSC Software, Santa Ana, CA, USA) to create 3D finite element models of the stented arteries. Stent designs had a constant strut thickness of 100 μm and a deployed outer radius of 2.5 mm (as designed by manufacturer; Fig. 5.1). The material of the stent was modeled as 316L stainless steel (E = 200 GPa, ν = 0.3). The artery was modeled as a straight homogenous cylinder with isotropic nonlinear hyperelastic material properties that were determined from biaxial mechanical testing of porcine arterial tissue as previously described [36]. Dimensions of the artery model were determined from measurements of hematoxylin and eosin (H&E) stained histological sections [inner unloaded radius (ρ_i), outer unloaded radius (ρ_o)] and from angiographic data [loaded inner radius (r_i)] obtained during stent implantation. Assuming that arterial tissue is

an incompressible material, which has been quantified experimentally [90], the loaded outer radius (r_o) value was determined by

$$r_o = \sqrt{r_i^2 + \frac{1}{\lambda_z}(\rho_o^2 - \rho_i^2)}$$

where λ_z is the axial stretch ratio. The axial stretch ratio assumed a value of 1.57, which agrees with experimental measurements obtained from the most distal end of porcine aortas just proximal to the iliac bifurcation [91]. As a result, the inner and outer radii values of the artery model at diastolic pressure were 1.72 (agrees with angiographic data) and 1.94 mm, respectively.

To determine the differences in the mechanical impact of implanting the two stent designs, the biomechanical environment induced on the artery wall was analyzed. In particular, circumferential (hoop) wall stress and radial displacement values on the inner surface of the artery wall were evaluated. Both parameters were examined at diastolic pressure, as it is during this time frame of the cardiac cycle where the impact of stenting is most severe. Circumferential wall stresses were analyzed as they are most likely to disrupt and possibly rupture the internal elastic lamina (IEL), which has been shown experimentally to be directly associated with the development of restenosis [60, 61]. Furthermore, previous analysis in our lab has indicated that circumferential stress constitutes the major contribution in the maximum principal stresses. Thus, only circumferential stress values on the intimal surface of the artery are presented herein. As a reference, the Law of Laplace estimates the

circumferential wall stress in an unstented artery with identical geometric dimensions as approximately 83 kPa at diastolic pressure. While this formula is not appropriate in this situation [i.e. the Law of Laplace is only applicable in determining the circumferential (Cauchy) stress in thin-walled pressurized cylinder], the value serves as a general reference guideline for evaluation of the extremely high non-physiologic, stent induced stress values placed on the artery wall. Radial displacement values on the inner surface of the artery were also analyzed as a means of assessing the ability of the stents to maintain a patent lumen following implantation (i.e. they provide enough radial rigidity to prevent elastic recoil by the artery).

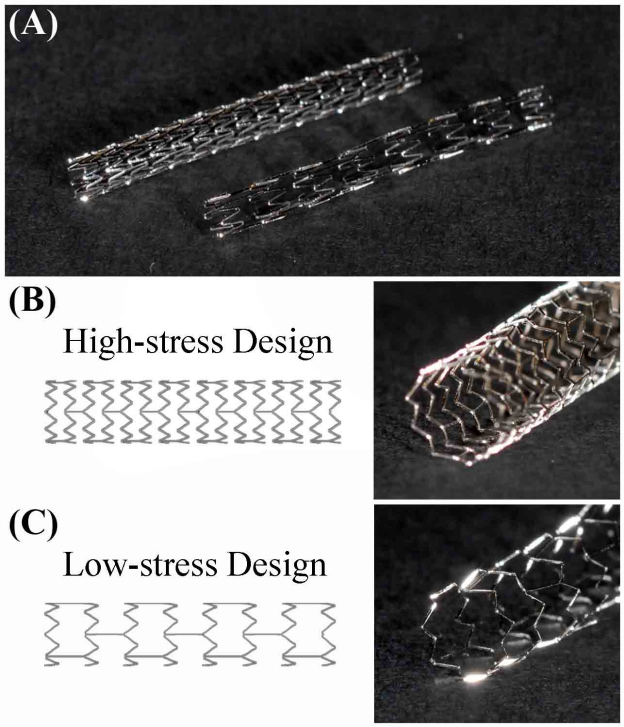

Figure 5.1: Vascular Stent Designs for the In Vivo Study and Computational Modeling. (A) Laser cut stent designs prior to attachment on balloon catheter system for implantation. (B) Deployed high-stress stent (left: finite element model, right: laser cut design) (C) Deployed low-stress stent.

Quantitative analysis of the FE models was achieved by evaluation of nodal values for circumferential stress and radial displacement. The nodal values were either plotted as color maps to assess the stress and displacement fields or exported for further post-processing (e.g. determining average values in the stented regions) in Matlab (MathWorks) subroutines.

Animal Model. All surgeries (n = 8) were performed in the catheterization suite in the Texas A&M Small Animal Clinic (College of Veterinary Medicine, Texas A&M University, College Station, TX). The Institutional Animal Care and Use Committee at Texas A&M University approved animal experimental procedures.

Prior to surgery, an initial pre-operation examination, including deworming and baseline blood work, was carried out on healthy female domestic pigs (n = 8). Seventy-two hours before surgery, the animals were given Aspirin (10 mg/kg, PO) and Plavix (75 mg, PO). Before surgery, an initial intramuscular injection of anesthesia (Buprenorphine, 0.05 mg/kg, IM; Telazol 5.0 mg/kg, IM) and a bolus of Heparin (300 units/kg, IV) were administered. Following intubation, the animals were maintained (Isoflurane, 1-4% MAC, inhaled; LRS drip, 10 mL/lb, IV) with a continuous infusion of Heparin (10 mL/hr, IV). Heart rate (ECG), blood pressure (tail cuff), blood gases (pulse oximeter), and core temperature were continuously monitored. The neck area was prepared for aseptic surgery and draped. An incision was made lateral to the midline overlying the left common carotid artery, which was isolated and controlled with arterial loops. An 8 F catheter sheath was passed into the left carotid artery, and subsequently a guide wire was introduced and guided to the pelvic region under fluoroscopy. Prior to stent implantation, the hind limb vascular

region was visualized to determine vessel diameter and other anatomical features (e.g. branching, taper, etc.). All images and videos were stored digitally. One stent design was deployed in the left common iliac (or common femoral) artery. The procedure was repeated in the contralateral iliac (or femoral) with deployment of the other stent design, such that one of each design was implanted in the left or right iliac (or femoral) artery. In the event that the vasculature allowed for multiple stents to be deployed on each side (i.e. proper vessel diameter along sufficient length), a total of four stents were deployed (1 stent of each design in each side). Angiograms were obtained to document stent post-deployment location, baseline diameter, and proper strut apposition. The implantation sites for the two stent designs were randomized. Animals recovered in singles cages and then returned to social housing. The animals received daily doses of Aspirin (10 mg/kg, PO) and Plavix (75 mg, PO) post-operation.

Approximately 28 days post-implantation, animals were anesthetized as described above and a final angiogram was obtained. The animals were euthanized with a bolus injection of Buthanasia (39 mg/kg) and transported to the necropsy lab for tissue harvesting. After the stented arteries were located, they were flushed with phosphate buffered saline for 10 minutes and fixed in situ by perfusion with 10% neutral buffered formalin for 10 minutes. The stented vessels were isolated, photographed, and transported to the Cardiovascular Pathology Laboratory (Department of Veterinary Pathobiology, College of Veterinary Medicine, Texas A&M University) for processing.

Histopathologic Evaluation. Following tissue harvesting and removal of excess connective tissue, stented artery specimens were prepared for histological analysis. Prior to

micro-CT acquisition, stented arteries were injected with a barium sulfate solution (0.56 g/mL) to ensure adequate contrast between the vessel lumen, stent struts, and surrounding arterial tissue. Barium-injected specimens were then dehydrated through graded alcohols, infiltrated with plastic embedding media (Technovit 7200, EXAKT Technologies, Inc., Oklahoma City, OK, USA), and polymerized.

Once the tissue was processed, micro-CT images of the stented arteries were acquired (HAWK-160XI, X-Tek Group, Inc., Santa Clara, CA, USA). Micro-CT scans were reconstructed (VGStudio MAX, v. 2.0, Volume Graphics, Heidelberg, Germany) for visualization and qualitative evaluation of stent structural integrity. Furthermore, 8-bit image stacks of the micro-CT scans were exported to conduct measurements on the stented arteries (discussed below).

Following micro-CT scan acquisition, histological sections were prepared and analyzed. Briefly, embedded specimens were cut with a diamond-coated band saw (EXAKT 300, EXAKT Technologies Inc.), and two sections from the middle region of each stent were prepared and micro-ground to a thickness of approximately 10 μm (EXAKT 400, EXAKT Technologies Inc.). For each stented artery, one micrograph was stained with H&E to examine cellular type/quantity and fibrin deposition, while the other was stained with Verhoeff van Gieson (VVG) elastin stain for injury scoring. Morphometric analysis was performed to quantify the areas inside the lumen, internal elastic lamina (IEL), and external elastic lamina (EEL), and the neointimal thickness at each stent strut (Image-Pro® Plus, v. 6.3, Media Cybernetics, Inc., Bethesda, MD, USA). Measurements allowed for calculation of intimal area (IEL area – lumen area), medial area (EEL area – IEL area), and percent

stenosis {[1 – (lumen area/IEL area)] x 100}. Furthermore, histologic analysis was carried out to quantify vessel injury [modification from [92-94]], inflammation [modification from [94-96]], residual erythrocyte distribution, residual erythrocyte state, presence of neovascular buds, fibrin deposition, and presence of multinucleated giant cells (MNGC).

Novel quantitative micro-CT techniques were utilized to further assess the pathobiologic response. These techniques allow for measurements of common morphological features of the stented arteries (e.g. lumen area, stented area, neointimal area) without the need for histological processing. As discussed above, image stacks of the micro-CT scans were exported from the reconstruction software and subsequently imported into a custom automated Matlab (MathWorks, Natick, MS, USA) subroutine. Imaging processing techniques (e.g. thresholding, size exclusion) were applied to each micro-CT image (~1400 per scan; resolution ~20 μm) to separate the artery lumen and stents struts. Knowing the resolution of the images allowed for calculation of the lumen area, while the area encompassed by the stent in each image was determined by fitting an ellipse (least-squares fit) to the outer edge of the stent struts. The areas encompassed by the stent and lumen were determined, with the difference between the two denoting the neointimal area.

Following analysis of each image, the micro-CT images corresponding to the prepared histology slides (stained with VVG) from the middle of the stents were visually determined to allow for comparison of the two techniques. Briefly, independently determined morphometric measurements of the lumen areas were compared and a correction coefficient that related the two values was calculated; note that a different correction coefficient was calculated for each specimen; note that a different correction coefficient was

calculated for each specimen, as differences in beam power and focal plane orientation varied amongst CT scans. To verify that the correction coefficient held true for any region of the stented artery, independent morphometric measurements were carried out on the H&E stained histology slide and corresponding micro-CT image. The calculated correction coefficient for a given specimen was applied to the lumen area calculated from the micro-CT image, and the corrected value was then compared to the lumen area measured from the histology slide. For all specimens measured, the average difference between the corrected micro-CT and histology lumen values was 0.24 mm^2 (difference of 2.03%) with a difference never greater than 0.90 mm^2 (figure on page 97). Following calculation and verification of the correction coefficient, analysis could be conducted on any region of the stented artery. In particular, quantitative micro-CT was carried out at the proximal and distal regions of the stented arteries. Micro-CT images approximately 4.3 mm from the stents edges were analyzed and neointimal areas were determined. These specific locations from the stent edges were chosen as they allowed for proper evaluation of these regions, while ensuring that there was no artifact due to tissue prolapse at the edges as a result of harvesting and fixing of the tissue.

Statistical Analysis. Histomorphometric parameter values were calculated at each stent strut within a single micrograph, while morphometric values were determined from three measurements per micrograph (intimal area, medial area) or a measurement at each stent strut (neointimal thickness). Differences between stent groups were determined using the paired Student's *t*-test with $p < 0.05$ deemed statistically significant. All results are reported as mean ± standard error of the mean (SEM).

Results

Examination of the finite element analysis results reveals that the high-stress stent induces considerably larger circumferential stress values on the artery wall than the low-stress stent at diastolic pressure. On average, tensile circumferential stress values on the inner surface of the artery models were approximately 20% larger in the high-stress stent than the low-stress stent in the stented region of the artery (Fig. 5.2). Peak stress values of approximately 2600 kPa (> 11x larger than the unstented vessel at diastole) were observed for both the high-stress and low-stress stent; however, the high-stress stent subjected the artery to such large stress values over relatively diffuse areas of the stented region. Circumferential stress values > 2350 kPa covered > 99% of the artery wall. In contrast, the low-stress stent only induced such high stress at focal regions of the intimal surface that were directly adjacent to stent struts, with stress values > 2350 kPa only covering < 2% of the artery wall.

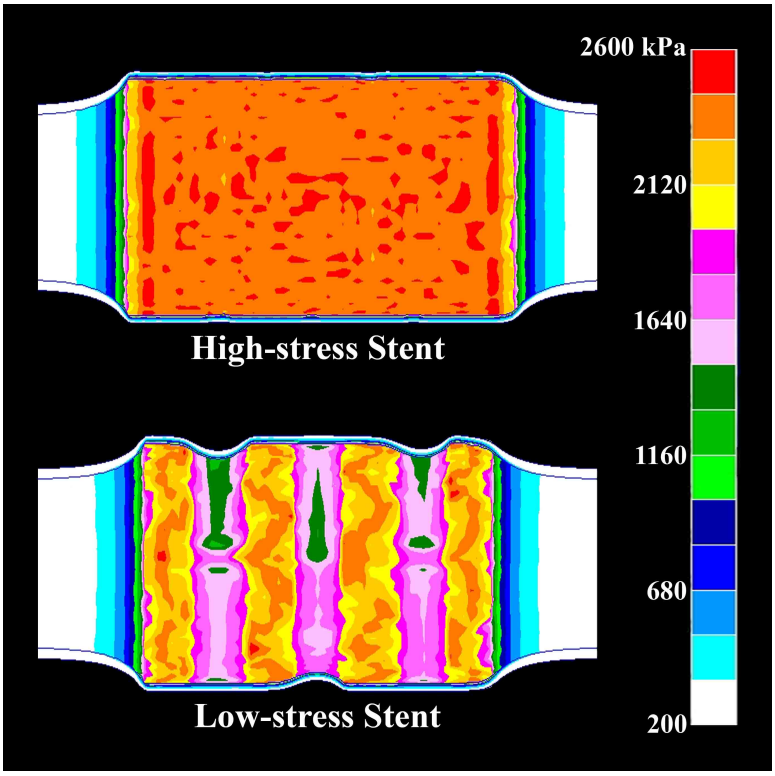

Figure 5.2: Circumferential (hoop) Stress Fields on the Intimal Surface of the Artery Wall at Diastolic Pressure. The high-stress stent imposed extremely high stresses (> 2500 kPa) across large regions of the artery, while the low-stress stent only induced such values at focal regions. On average, the low-stress stent induced stress values that were 400 –500 kPa lower than the high-stress stent design.

In general, regions of high stress were also the sites of the greatest radial displacement in the stented region (i.e. the highest radial displacements occurred where the stent struts contacted the artery wall). Overall, the high-stress stent design displaced the artery to a more uniform radial position than the low-stress stent (Fig. 5.3). At locations where the high-stress stent was in contact with the artery wall, the artery was displaced approximately 0.73 mm in the radial direction. Note, herein, that radial displacements are in reference to the position of the lumen surface at diastolic pressure (i.e. a radial displacement of 0.00 mm indicates that there was no increase in lumen size). Furthermore, radial

displacement values > 0.68 mm occurred over > 98% of the inner surface of the stented region, with an average radial displacement of 1.50 mm. In contrast, the low-stress stent displaced the artery wall > 0.68 mm on only < 3% of the inner surface, with an overall average radial displacement value of 1.43 mm. While there are differences in radial displacement values between the two stent designs, the differences were minimal (average difference ~ 70 μm).

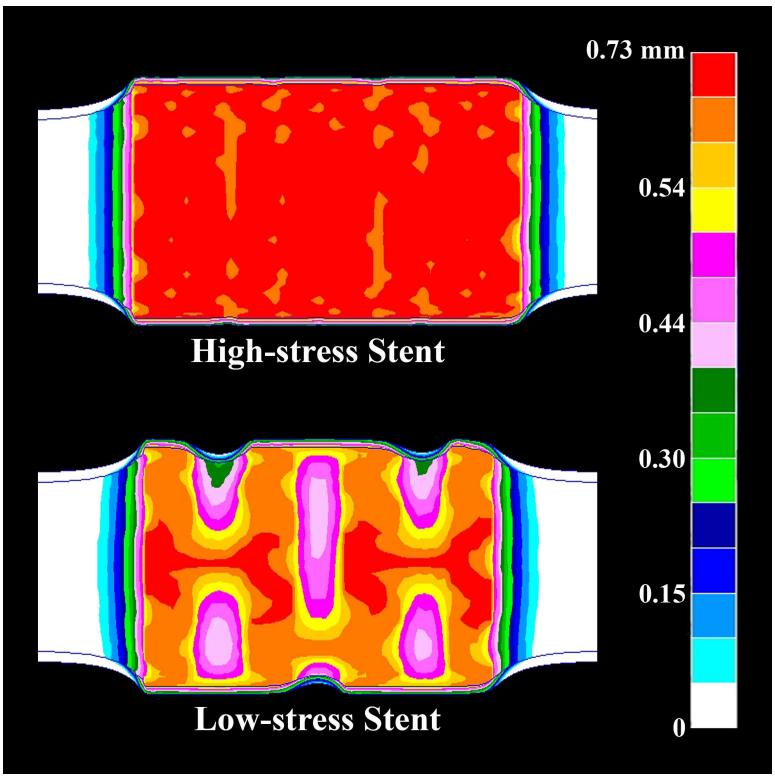

Figure 5.3: Radial Displacement Distributions on the Intimal Surface of the Artery Wall at Diastolic Pressure. As the high-stress stent induced the highest stresses on the artery wall, it also displaced the artery to a greater radial position than the low-stress stent design. Note '0' represents the inner radial position of the artery wall at diastolic pressure when no stent is present.

All animals survived the implantation procedure. In total, 8 non-atherosclerotic pigs were used in this study, with 18 stents deployed (9 of each design; note that in one animal, 4 stents were deployed, as the size and geometry of the vasculature allowed for multiple implantations). There were no episodes of subacute stent thrombosis, and all of the stents remained patent prior to euthanasia, as observed under angiography.

Morphometric measurements showed that intimal area was significantly greater in the high-stress stent group (Fig. 5.4A; $p = 0.00008$). Intimal area values of 4.333 ± 0.303 and 1.599 ± 0.175 mm^2 were observed between the high-stress stent and low-stress stent groups, respectively; however, medial area was not significantly different between the groups (1.569 ± 0.162 vs. 1.349 ± 0.092 mm^2, respectively). Furthermore, the percentage of stenosis was also significantly greater in the high-stress stent group, with values of 23.598 ± 1.697 % and 15.643 ± 2.272 %, respectively (Fig. 5.4B; $p = 0.004$). In addition, examination of the neointimal thickness at each stent strut revealed a significantly greater thickness value for the struts in the high-stress stent group when compared to the low-stress stent group (Fig. 5.4C; $p = 0.0004$). The high-stress stent group had an average neointimal thickness value at each stent strut of 0.197 ± 0.020 mm, while the low-stress stent group had a value of 0.071 ± 0.016 mm. Qualitative analysis of the micrographs further confirmed this observation of greater neointimal thickness in the high-stress stent group (Fig. 5.5).

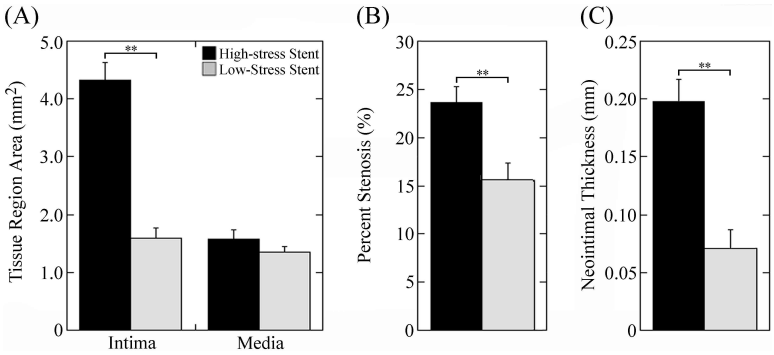

Figure 5.4: Results from Morphometric Analysis. (A) Areas of intimal (IEL area - lumen area) and medial (EEL area – IEL area) regions. (B) Percent stenosis [1 – (lumen area/IEL area) x 100]. (C) Neointimal thickness at stent struts. Data are means ± SEM of 18 tissue samples (9 per stent group). Statistically significant differences ($p < 0.01$) are denoted by double asterisks.

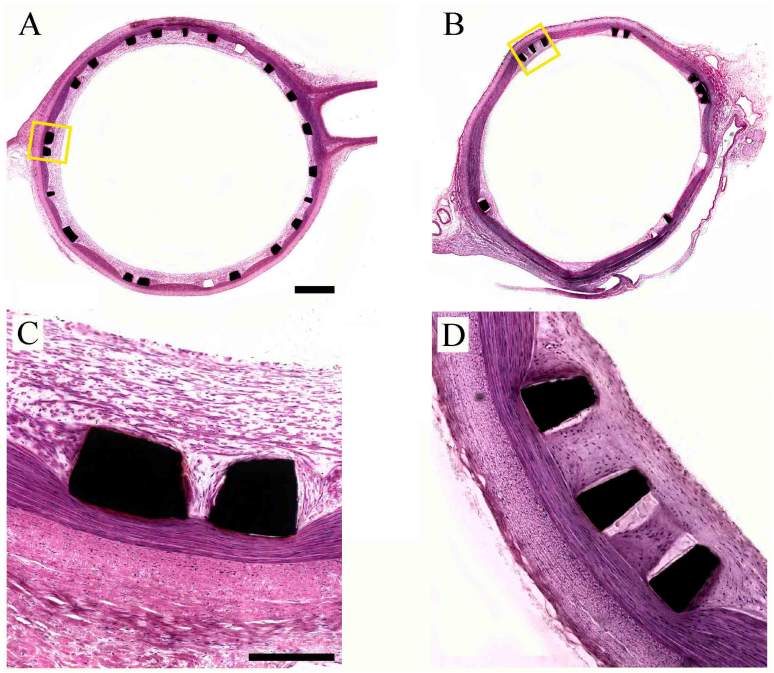

Figure 5.5: Representative Photomicrographs of Plastic Embedded Stented Vascular Cross Sections from the Same Animal Stained with Hematoxylin and Eosin (thickness ~ 10 μm). Significant neointimal growth is observed at the struts of the high-stress stent (A, C; neointimal thickness = 0.107 ± 0.006), while minimal tissue growth is observed on the low-stress stent (B, D; neointimal thickness = 0.039 ± 0.007). Low magnification (A, B; scale bar = 5 mm), high magnification (C, D; scale bar = 250 μm).

The micro-CT techniques provided further quantitative data of differences in the pathobiologic response following implantation of the two stent designs (Fig. 5.6). In particular, it allowed for examination of the amount of neointimal tissue present at the proximal and distal edges of the stents without the need for histological processing. Examination of the micro-CT images at these locations again revealed a significant difference between the stent groups in the amount of neointimal tissue present. At the proximal edge, the high-stress stent group had a neointimal area value of 6.545 ± 0.557 mm^2, whereas the low-stress stent group had a value of 2.864 ± 0.254 mm^2 (Fig. 5.6E; $p = 0.0002$). Furthermore, analysis of the neointimal area at the distal edges of stents showed a significant difference between the stent groups ($p = 0.004$), with values for the high-stress and low-stress stent groups of 6.542 ± 0.578 mm^2 and 3.229 ± 0.694 mm^2, respectively. In addition to differences in the amount of neointimal tissue present between the stent groups, variations in the neointimal area values at various locations (proximal, middle, distal) within a given stent group were observed. For both stent designs, there were significant differences in the neointimal area when comparing the proximal and distal region values to those obtained at the middle regions. However, the results were not significantly different when comparing the amount of neointimal tissue amongst the proximal and distal regions.

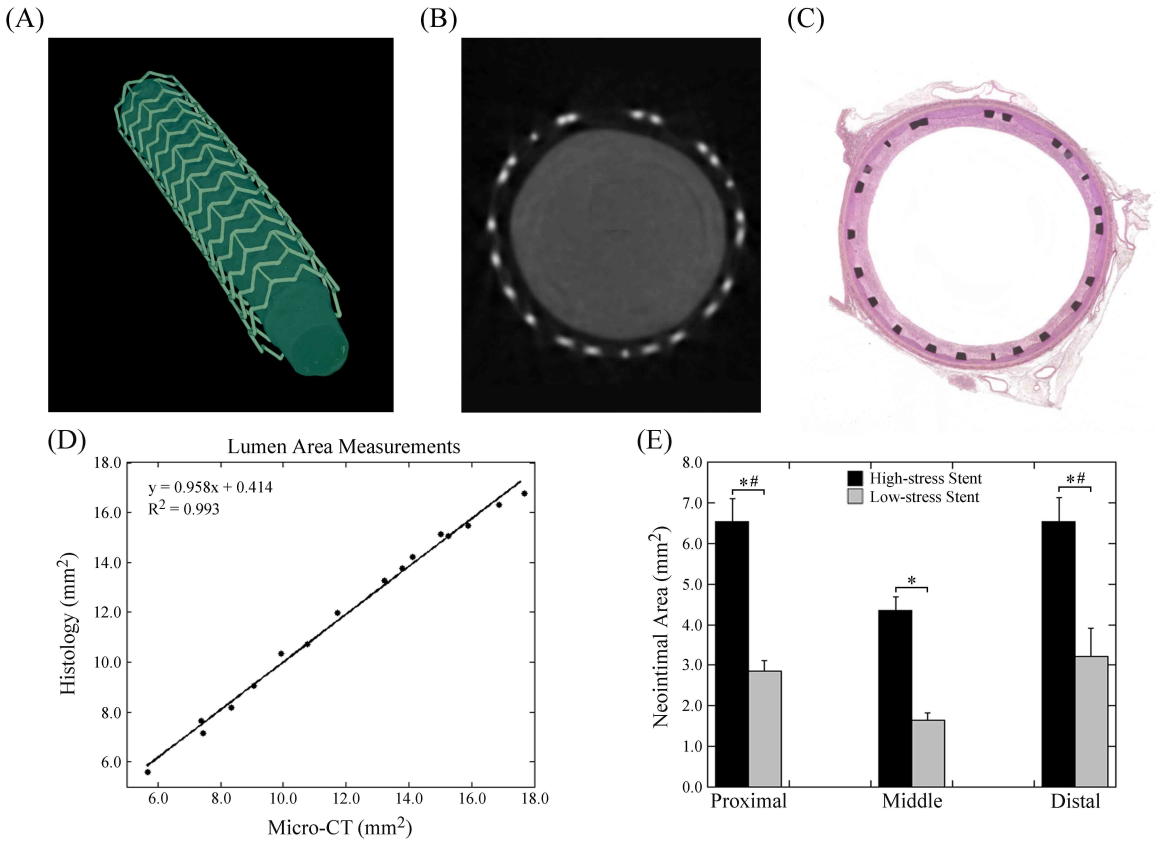

Figure 5.6: Quantitative Micro-CT Analysis Techniques and Results. (A) Representative micro-CT rendering of a stented vessel with barium sulfate solution injected into the lumen. (B, C) Micro-CT axial slice and corresponding H&E stained micrograph from the middle region of the stented artery. (D) Evaluation of the quantitative micro-CT techniques to determine the accuracy of the morphometric data obtained from analyzing the micro-CT images. Note a linear regression line denoted by the equation $y = x$ would indicate an identical agreement between the two techniques. (E) Neointimal area values from the proximal middle and distal regions of the stented arteries. Data are means ± SEM of 16 tissue samples (8 per stent group). Statistically significant differences ($p < 0.01$) between stent groups (high-stress vs. low-stress) are denoted by asterisks, and between locations within a stent group (proximal vs. middle, distal vs. middle) are denoted by hash marks.

Histopathologic analysis revealed minimal difference in the distribution of injury scores between the stent groups (Table 5.1). In most cases, the stent struts were in contact, but not penetrating, the IEL (score equal to 1). Furthermore, inflammation, RBC distribution and state, neovascular bud formation, and presence of MNGC were similar between the

groups. It should be noted that fibrin deposition was greater in the high-stress stent group than in the low-stress stent group, however the difference was not statistically significant.

Table 5.1: Histopathologic analysis of implanted stent designs.

Parameter	High-Stress Stent	Low-Stress Stent
Injury	0.976 ± 0.024	0.901 ± 0.043
Inflammation	1.010 ± 0.007	1.031 ± 0.018
RBC Distribution	0.034 ± 0.016	0.112 ± 0.044
RBC State	0.063 ± 0.032	0.174 ± 0.081
Neovascular Buds	0.000 ± 0.000	0.000 ± 0.000
Fibrin Deposition	1.110 ± 0.096	0.860 ± 0.123
MGNCs	0.192 ± 0.047	0.189 ± 0.058

Discussion

This investigation used both computational and direct in vivo analysis to provide unique information on the role of solid biomechanics in the development of restenosis. Two stent designs (defined as the high and low-stress stents) were implanted in porcine iliac (or femoral) arteries and analyzed using various integrative pathologic techniques. Furthermore, computational methods were utilized to analyze the biomechanical impact of these varying stent designs in an artery model that featured nonlinear strain-stiffening properties. Results indicate that the stent design that induced higher stress values on the artery wall lead to a more significant pathobiologic response as determined by the amount of neointimal hyperplasia.

To our knowledge, the data presented are the first to document stent-induced variations in the solid biomechanical environment with corresponding direct quantitative in

vivo evidence of neointimal tissue growth (i.e. not angiographic clinical data). Both stent designs were constructed of the same material, deployed under the same conditions, and showed no significant difference in histopathologic response (Table 5.1). Differences between the stents where only observed in their biomechanical environments (Fig. 5.2 and 5.3) and associated amounts of neointimal tissue (Figs. 5.4 and 5.5). Thus, we conclude that the resulting pathobiologic differences are a direct result of the mechanical loads placed on the artery wall, confirming the hypothesis that stents that induce a non-favorable biomechanical environment (i.e. subject the artery to higher, non-physiologic stresses) provoke a more aggressive pathobiological response.

Computational analysis has emerged as a valuable analysis and design tool for evaluation of implantable medical devices. Vascular stents have garnered much interest in this area, as the implantation of a stent is a highly complex mechanical process and the biomechanical interaction of the stent and artery is, as shown, important in the long-term success of the therapy. However, while many studies have developed sophisticated numerical methods to investigate stented artery biomechanics, few studies have directly applied their results to experimental or clinical data. As observed in this investigation, other computational studies have also indicated a strong correlation between stent-induced arterial wall stress and clinical angiographic restenosis data. Lally et al. [45] demonstrated that the NIR stent design (Boston Scientific, Maple Grove, MN, USA) induced much higher stresses than the S7 stent design (Medtronic, Minneapolis, MN, USA) on a generalized atherosclerotic artery model. Such results support clinical findings, as 6 month follow-up data of the two designs report restenosis rates of 19.0 and 10.1%, respectively. Berry et al.

[37] evaluated the arterial wall mechanics and resulting short-term (7 days) pathobiologic response in a swine model of a prototype stent that provides a smoother transition in compliance at the edges of the stent [termed compliance matching stent (CMS)]. Comparison of the computational results between the CMS and the commercially available Palmaz-Schatz designs indicated that the CMS reduced the circumferential wall stresses at the ends of the stent. The reduction in stress values was associated with minimal accumulation of thrombus and inflammatory cells when comparing in vivo results for the CMS [37] and Palmaz-Schatz designs [97]. It is interesting to note that in our investigation the highest amount of neointimal tissue was present at the edges of the two stent designs (Fig. 5.6), which agrees with clinical findings [98]. These are the regions where the highest gradients in wall stress were observed (Fig. 5.2), with the largest gradient, or compliance mismatch, occurring in the high-stress stent. This finding provides further evidence that a stent design that reduces the abrupt change in wall stress could reduce the amount of neointimal proliferation.

Explanations for the reasoning behind the differences in the observed pathobiologic response are directed at the alterations in the highly controlled and sensitive native biomechanical loading environment that is disrupted following stent implantation. As experimental studies have indicated, the vasculature adapts to changes in blood flow, sustained increases in blood pressure, and altered axial extension in such as manner as to restore the altered mechanical state (e.g. mean wall shear stress, circumferential and axial wall stress) to homeostatic levels [see review by Humphrey [99]]. Thus, it is reasonable to expect that following stent deployment the artery will remodel in such a way (neointimal

hyperplasia) as to attempt to return the wall stresses to values prior to the interventional therapy. The greater the difference between the stent-induced and homeostatic wall stresses, the more aggressive the biological response, and in the case of this investigation, the higher degree of neointimal tissue. Such a statement is supported by a theoretical model proposed by Rachev et al. [100] that examined the stress-induced thickening of the arterial wall at regions near a stent. Results indicate that local arterial thickening is a remodeling process that occurs due to changes in the biomechanical environment to which the artery adapts. Furthermore, the model predicts that arterial thickening is greatest at regions where stress concentrations are the highest (i.e. where stress concentrations deviate the most from the homeostatic value). Collectively, these data indicate that stent designs that subject the artery wall to lower stress values, or whose induced stress values deviate the least from homeostatic values, will have greater long-term success.

There are several limitations in this study that should be addressed. Firstly, the experimental results in an animal model do not fully capture the mechanisms as they occur in humans. As noted by Farb et al. [96], the pathobiologic response in porcine models closely reflects those observed in humans; however, the healing response in humans takes longer. Regardless, porcine models are readily utilized for evaluation of vascular stents because their vascular anatomy is comparable to that in human, thus allowing for the use of catheters and devices as employed in humans. Furthermore, porcine arteries develop an identical histopathologic response as humans after both balloon injury and stent placement [92, 101], therefore serving as a suitable restenosis models for the evaluation of stent design. Secondly, the stents were implanted in a non-diseased animal model. As this investigation

was focused on evaluating the pathobiologic response between two stent designs that impose strikingly different biomechanical environments, inclusion of heterogeneous atherosclerotic plaques may have confounded direct comparison between stent groups (i.e. plaque morphology and composition would not be constant from animal to animal, or even vessel to vessel). Moreover, the differences in the stenoses would have limited the applicability of the computational analysis to the in vivo results, and would have required complex "patient"-specific computational models to be computed for each animal. Thirdly, our novel micro-CT techniques do not allow for quantitative evaluation of the histopathologic response throughout the entire stented artery. Thus, it is possible that specific pathologic findings might not have been accounted for in analysis. While not presented, histopathologic evaluation was carried out along the entire length of a stented artery specimen (i.e. approximately 25 histology slides) with no significant difference in the analysis parameters as exhibited in Table 5.1. Furthermore, in all histology slides examined (~ 325 stent struts) there was never a presence of large accumulations of macrophages and MNGC, eosinophils, and/or granulomatous tissues. Therefore, in the present study the novel micro-CT techniques provided a valuable and efficient analysis tool. Fourthly, as with any computational modeling study there are limitations in the computational techniques. Briefly, these limitations include characterizing the artery as a homogeneous, isotropic, hyperelastic material, neglecting the effects of residual strain, and not modeling the stent balloon expansion process. Such limitations have been discussed in detail elsewhere [36, 56]. It should be noted that inclusion of these features would have been extremely computationally

demanding and would have not likely affected the relative comparison between the two stent designs (high-stress stent would still impose greater stress values).

Designing the next generation of vascular stents will require collaborative efforts between clinicians, biomechanicians, cellular biologists, polymer chemists, and manufacturing engineers, to name a few. The work presented constitutes a major effort in characterizing the mechanical impact of vascular stenting and offers information on specific design criteria to reduce the pathobiologic response. However, there are other design criteria that are valuable and should be considered. Most recently, application of cytostatic pharmaceutical agents to stents has gained notoriety (DES). Despite their shortcomings [e.g. late stent thrombosis [65], lack of success in peripheral arteries [66]], the technology does offer promise to the interventional therapy. It is likely that the most successful stents of tomorrow will combine intelligent biomechanics with advancements in drug-elution. In addition, advancements in high-resolution imaging techniques (e.g. computed tomography, magnetic resonance imaging intravascular ultrasound, optical coherence tomography) will allow visualization and characterization of the diseased vasculature prior to intervention. Such information will allow for the development of patient-specific computational models that allow for mechanical, durability, and efficacy testing [as discussed for endovascular devices by Zarins and Taylor [102]], and thus ensure that the most optimal stent is implanted (i.e. patient-specific stenting).

In conclusion, this study provides valuable insight into the role that biomechanics can play in the failure of vascular stents. The results not only provide information that is directly applicable to commercially available designs, but also yield information about specific

design criteria and considerations that should be made when designing the next iteration of stents. In addition, the novel integrative pathology techniques presented (e.g. quantitative micro-CT) provide a means of extracting high-detailed quantitative data from the pathobiologic response of vascular stents, and such methods are applicable to examine other implantable medical devices.

CHAPTER VI

STRUCTURAL INHOMOGENEITY AND FIBER AND CELLULAR ORIENTATION IN THE INNER ARTERIAL MEDIA

Overview

The microstructural orientation of vascular wall constituents is of interest to scientists and clinicians, as alterations in their native states are associated with various cardiovascular diseases. In the arterial media, the orientation of these constituents is often described as circumferential. However it has been noted that, just below the endothelial surface, the vascular wall constituents are oriented axially. To further study this reported change in orientation, and resolve previous observations (which were made under conditions of no load), we used nonlinear optical microscopy to examine the orientation of collagen and elastin fibers in the inner medial region of bovine common carotid arteries. Images were obtained from this part of the arterial wall under varying degrees of mechanical strain: 0%, 10% axial, 10% circumferential and 10% biaxial. We observed that close to the endothelium these components are aligned in the axial direction, but abruptly change to a circumferential alignment at depth of approximately 20 μm from the endothelial surface. Application of mechanical loads resulted in a significantly greater degree of fiber alignment in the loading direction, regardless of their initial unloaded orientation. Furthermore, variations in loading conditions resulted in an increase or decrease in the overall degree of fiber alignment in the sub-endothelial layer depending on the direction of the applied strain. This high resolution investigation provides a more detailed description of the complex structure-function

relationships in vascular tissue, which is essential for a better understanding of the patho-physiologic processes resulting from injury, disease progression, and interventional therapies.

Introduction

The microstructure of the normal arterial wall, while varying with species, location, age, and disease, is comprised of three layers: the tunica *intima*, tunica *media*, and tunica *adventitia*. In particular, the medial layer of conduit arteries consists of alternating layers of vascular smooth muscle cells (VSMC) and elastic lamina (termed the *musculo-elastic fascicle*), with collagen fibers interlaced between the elastic lamina (refer to figure 11.A in [103]). Numerous studies have examined the orientation of fibers and VSMC within medial tissue of conduit arteries, yet there has been no conclusive agreement on their preferred orientation. VSMC orientation has been expressed as circumferential [104-107], oblique [107, 108], and helical [107, 109], with similar findings described for collagen and elastin fibers. However, we note that all observations were made on relaxed vascular tissue.

Regardless of such wide variation in findings, notable, yet often overlooked studies have acknowledged a distinct radial variation in fiber and cellular orientation within the medial layer. As first described by Wolkoff [110], the internal elastic lamina (IEL) of human coronary arteries appears to be split into two distinct laminae during growth and development. This process starts in utero by bending and fraying of the IEL, continuing through puberty and into old age. Gross et al. [106] reported similar findings in human coronary arteries in relation to aging. In particular, it was noted that as early as the third

month post-partum, a splitting in the IEL occurs leading to the formation of the “musculo-elastic layer”. During the break in continuity of the IEL, VSMC migrate into the newly formed layer and orient themselves axially, while those in the medial layer are still aligned circumferentially. It should be noted that during this process multiple elastin layers are formed, however, as noted by Gross et al., the outermost elastin layer still represents the border between the intimal and medial layers, and thus is still referred to as the IEL; herein, the term sub-endothelial refers to the region just below the endothelial surface but on the adluminal side of the IEL. IEL splitting and axially aligned fibrils has also been noted in pathological states, such as the formation of intimal pads or cushions and hypertension [111, 112]. An axial orientation of inner medial fibers and VSMCs in the porcine aorta has been described by Clark and Glagov [103], who suggested that it is associated with shear stress from the flowing blood transmitted into the inner layers of the media. A similar arrangement has been seen in human cerebral arteries [113]. Smith [114] described a variation in fiber orientation throughout the media of the rabbit pulmonary trunk, however he noted that this variation was not seen in the aorta. Again, however, all observations were made under conditions of no mechanical load.

Blood vessels contain highly extensible, isotropic elastin fibers and strain-stiffening, anisotropic collagen bundles and have mechanical properties that are strongly dependent on the alignment of the embedded fibrous constituents. Recently, constitutive formulations, which relate the applied stresses/forces to the resulting strains/deformations of biological tissues, have shifted from purely phenomenological descriptions to those that are structurally based. These constitutive relations incorporate fiber alignment into their formulations to

offer a better description of arterial mechanical properties [115, 116]. Therefore microstructural information, such as the density, interaction, and orientation of these vascular wall constituents, is essential if one wishes to accurately capture and model the material response of vascular tissue, both normal and diseased.

Various optical techniques have been utilized to examine fiber orientation [e.g. histological polarized light microscopy [117]; scanning electron microscopy [118-120]]. However, such methods are destructive to the tissue and not suitable for examination of a single tissue sample under multiple experimental conditions. To overcome this limitation, non-destructive methods for analyzing fibrous structures have been developed [e.g. small angle light scattering [121-123]; small angle x-ray scattering [121, 124]]. Nonlinear optical microscopy (NLOM) provides an excellent means of examining the orientation and distribution of constituents within biological tissues. For instance, second harmonic generation [SHG; [125]] and two-photon excited fluorescence [TPF; [126]], both of which are confocal techniques, provide a means of collecting thin optical sections (i.e. images) from within thick specimens. Such attributes are ideal for a quantitative examination of fiber orientation under various experimental conditions, and have been utilized in previous investigations [127, 128].

As a means of further investigating the fiber alignment in the arterial wall, as well as examining of the structure-function relationship in vascular tissue, we have employed NLOM techniques to characterize quantitatively this previously reported sub-endothelial axially aligned fiber region under varying physiologic loading conditions. Our objective in this study was to quantify collagen and elastin fiber orientation in the inner part of the bovine

common carotid artery. In addition, analysis of the fiber alignment in this sub-endothelial layer under loading was performed, as a means of resolving previous observations that were carried out under no loading conditions. The results from this investigation will provide further data on the relationship and interactions between arterial tissue components and thus lead to a better understanding of the structure-function relationship of vascular tissue in general.

Methods

Following the several reports of axially aligned fibers and cells on the abluminal side of the endothelial surface, we used NLOM methods to investigate this sub-endothelial region of the arterial medial layer. Optical sections were acquired radially outward from the endothelial surface with a custom designed NLOM system. The orientations of extracellular matrix fibers were analyzed by application of a subroutine based on a fast Fourier transform (FFT) algorithm and then quantified by a polar coordinate analysis of the filtered power spectrum of each image. The NLOM results were qualitatively verified by comparing them to light microscopic images of histologically stained sections.

Tissue Preparation and Biaxial Testing. Bovine common carotid arteries were collected from a local abattoir and transferred to the laboratory in phosphate buffered saline (18°C). Following removal of loosely adherent perivascular tissue, a ~ 2 cm long segment was removed, opened circumferentially with an axial cut, and attached to a modified version of a biaxial mechanical testing device previously described [127]. The remainder of the artery was set aside for histological evaluation. Briefly, the testing device consisted of four

polycarbonate clamps sliding on stainless steel rods. The clamps and rods were arranged in pairs, and the pairs were oriented at right angles to each other. By moving either or both clamp pairs, independent movement in the x- and y- directions was possible. A square section was cut from the artery for testing, and each edge was attached to a clamp by four equidistant, non-continuous loops of 2-0 silk suture. The device chamber was then filled with phosphate buffered saline (25°C) to completely submerge the tissue prior to imaging on the NLOM system (Fig. 6.1). Note that specimens were positioned such that the intimal surface was nearest the microscope objective (i.e. the first image acquired was of the endothelial surface). Specimen unloaded dimensions (0% strain state) were determined by stretching the tissue sample until it was flat and free of wrinkles. Measurements of the distances between the clamps in each pair were recorded and noted as the unloaded dimensions. Subsequent strain states (10% axial, 10% circumferential, and 10% biaxial) were achieved by sliding the stainless steel arms, thus moving the clamps to measured locations and fixing their positions with set screws. Each pair of arms was moved a similar amount ensuring that the center of the specimen did not move appreciably as it was stretched. All strain measurements were made with vernier calipers to the nearest 100 μm. The testing device, with specimen intact, was then returned to the microscope stage and images were acquired at the central location of the tissue specimen, judged by eye.

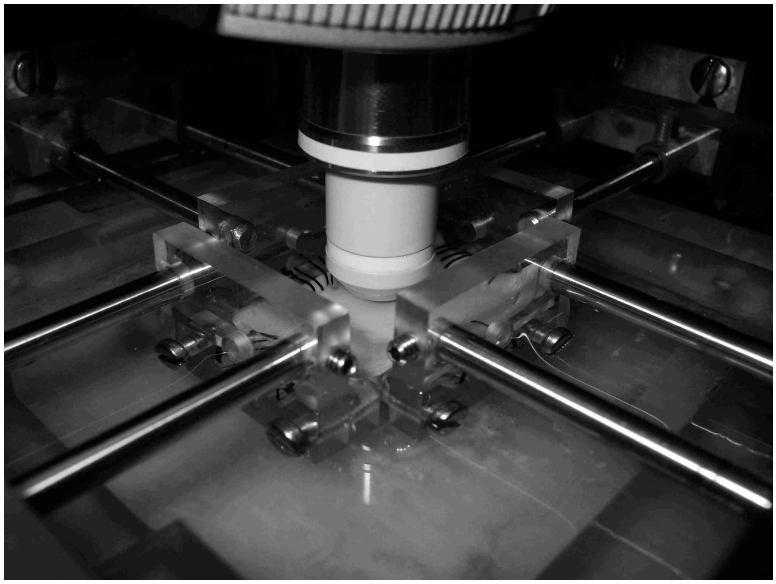

Figure 6.1: Biaxial Mechanical Testing Device on Microscope Stage. Photograph of a specimen (bovine common carotid artery) attached to the four stretching arms within the testing device on the microscope stage. NLOM images were acquired from the central region of the specimen. The intimal side of the specimen was nearest to the microscope objective (i.e. intimal side imaged first).

Nonlinear Optical Microscopy. Our custom built NLOM system has been described in detail previously [127, 129]. Sub-10-fs pulses from a Kerr-lens mode-locked Ti:Al_2O_3 oscillator (Femtosource; Femtolasers, Cambridge, MA) pumped by a frequency-doubled Nd:YVO_4 solid-state laser (Verdi; Coherent, Santa Clara, CA) were coupled into the epifluorescence port of an upright microscope (Axioskop2 MAT; Carl Zeiss, Thornwood, NY) via dual-axis galvanometer driven mirrors (Cambridge Technology, Lexington, MA) mounted on an elevated breadboard. The entire NLOM system was atop a vibration-isolated optical table. The laser beam was directed to the microscope focusing objective (40X Achroplan, N.A. = 0.8, water immersion; Carl Zeiss) by a short-pass dichroic mirror (635dcspxruv3p; Chroma, Rockingham, VT). Nonlinear optical signals were directed by the

objective through one of two accessory ports on the binocular head, to a custom-built dual channel detector that houses two dichroic mirrors and bandpass filters (Chroma), focusing lenses (31 2321; Linos Photonics, Milford, MA), and a pair of photon-counting photomultipliers tubes (R7400P; Hamamatsu, Bridgewater, NJ). SHG and TPF signals were collected by appropriate long-pass dichroic mirrors (430dcxru, 505dcxru, respectively; Chroma), and band-pass filters (HQ405/40, HQ480/40, respectively; Chroma). Photomultiplier tubes were connected to a preamplifier/discriminator (F-100T; Advanced Research Instruments, Golden, CO) that thresholds signal current and converts it to transistor-transistor logic (TTL) pulses for photon counting. Due to the marked differences in spectral characteristics generated by the collagen and other fluorescent tissue components (e.g. elastin), the SHG and TPF signal components were imaged and segmented simultaneously. The result was that SHG and TPF NLOM images (optical sections) of fibrillar collagen type I and elastin in the media, respectively, were acquired in the central region of the specimen. Optical signal to noise ratio was improved by capturing four images at a rate of 0.5 Hz per image and averaging them. Successive averaged images were obtained starting from the intimal surface and moving medially in 0.5 μm steps 200 μm deep into the tissue. They were saved as raw 16-bit data files. Throughout the set of experiments described herein, less than 40 mW of laser power was incident on the scanning mirrors, thus minimizing thermal effects.

Histology. Standard histological techniques were used to process the arterial segments. Briefly, specimens were fixed in formal saline for 24 hrs, embedded in paraffin wax, and transverse and longitudinal sections were cut at 3 μm. Sections were then mounted

on electrostatically charged slides to enhance adhesion of the tissue to the glass (Superfrost Plus, VWR, UK), dried, and stained either with Ehrlich's hematoxylin [130], an adaptation of Miller's elastin stain [131], or picrosirius red [132] for visualization and examination of cell nuclei, elastin, and collagen, respectively.

Image Processing, Analysis, and Evaluation. Prior to image acquisition the focal plane was set just above the surface of the specimen (~5 μm). This setting ensured a clear signal from the luminal surface of the intima as the image plane was moved deeper into the arterial wall (i.e. outward in the radial direction). Following image stack acquisition (SHG and TPF), a Matlab (MathWorks, Natick, Massachusetts) subroutine was developed to determine the location of the intimal surface. Briefly, the average intensity value was determined for each SHG[1] image in the stack, and the image with the maximum average pixel intensity was determined. The innermost image (i.e. closest to the endothelial surface) in the stack that had a mean intensity value approximately 30% of the maximum average pixel intensity was defined as the location of the intimal surface, and data analysis of both SHG and TPF images were carried out from that point. Sensitivity analysis indicated that mean intensity values of approximately 20% and 40% of the maximum average pixel intensity resulted in a 3.5 and 2.5 μm shift, respectively, in the location of the image within the specimen thickness. Compared to the differences in cross-over region location (< 1 μm), this was deemed an acceptable justification of the choice of 30% intensity as the inner wall threshold.

[1] Average pixel intensity and maximum average pixel intensity were also determined for the TPF images in each image stack; however, the differences between the SHG and TPF maximum average pixel intensity locations were small (2.5 ± 1.0 μm) with no noticeable trend. Thus, only the SHG images were used to determine the location of the intimal surface.

Following the location of the intima, images (400 per image stack, maximum depth in the media 200 μm) were analyzed in a modified version of a previously described Matlab (MathWorks) subroutine to analyze collagen and elastin fiber orientation [127]. Raw image data files were *padded* with redundant data to enhance frequency resolution. Padding was achieved by reflecting (mirroring) the original image at 0°, 90°, 180°, and 270° (Fig. 6.2B) and applying a Gaussian decay (SD = 0.25) to the reflected images, such that the pixels bordering the original image had a < 0.04% reduction in the original pixel intensity and those at the edges were reduced to zero (i.e. pixel value of 0; black). The padding increased the size of the image from 237x256 to 512x512 pixels. Note that due to acceleration of the horizontal scanning mirror during the start of each scan line, the first 19 columns of pixels were removed. To reduce edge effects, a two-dimensional Hann window function was applied, followed by transformation of the image to the frequency domain (i.e. power spectrum) using a two-dimensional FFT [Fig. 6.2C; [119]]. High and low-pass Butterworth filters (sixth-order) were applied, removing frequencies greater than 60 Hz and less than 6 Hz. These cut-off frequencies were chosen by examination of the resulting inverse FFT images following filtering. Evaluation of the angular distribution of fibers was done by polar coordinate analysis of the filtered power spectrum image as described by Nishimura et al. [133]. Briefly, the relative intensity (RT) for angles between Θ ± 2° was calculated by

$$RT(\Theta) = \sum_{\theta \geq (\Theta-2)}^{\theta < (\Theta+2)} g(r,\theta) \Big/ \sum_{\theta \geq 0}^{\theta < 180} g(r,\theta),$$

where $g(r,\theta)$ is the pixel intensity value at the polar coordinate in the filtered power spectrum image. An interval of 4° was selected as it allowed for adequate separation

between fiber orientations, while not confounding results with too many data points. From this calculation, the predominant fiber angle (PFA) for each image was determined, as well as the alignment index (AI) as defined by Ng. et al. [Fig. 6.2D; [134]]. Briefly, AI quantifies the fraction of fibers that are aligned within ±20° of the PFA, normalized to the fraction of a random distribution of oriented fibers (= 40°/180°); the higher the AI, the higher the percentage of fibers aligned near the PFA (values range from 1.0 to 4.55). Note, herein, the image (and corresponding radial position) with the lowest AI for an image stack is referred to as the "cross-over region". PFA and AI values were then plotted against tissue depth to determine changes in fiber orientation as a function of radial position in the vessel media. For illustrative purposes, Matlab (MathWorks) and Adobe Photoshop (Adobe Systems Inc., San Jose, CA) were used for post-processing [conversion of files from data (.dat) to tagged image file format (.tiff), auto-contrast, pseudo-color] of the NLOM images.

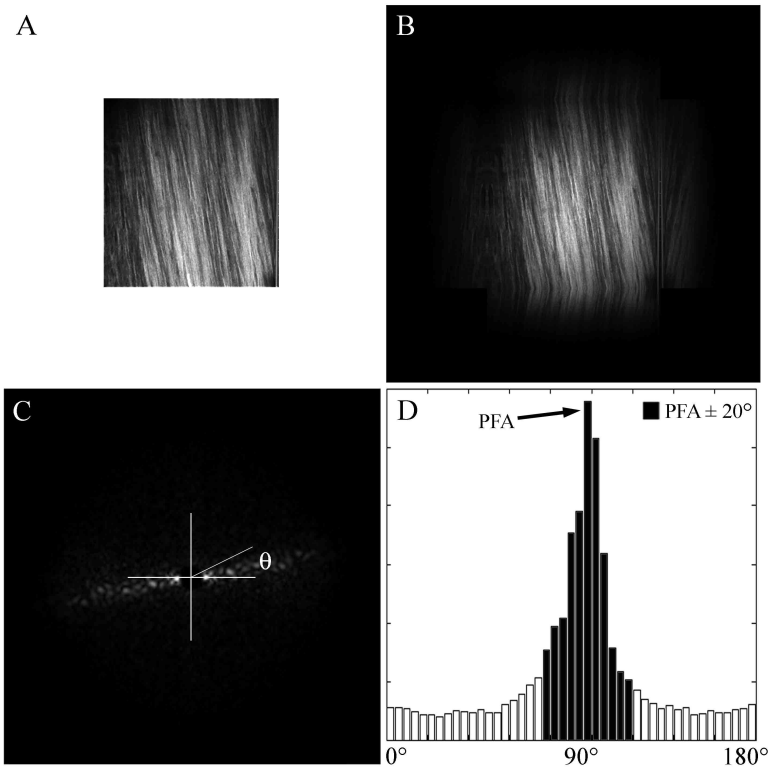

Figure 6.2: Algorithm to Calculate Fiber Angle from NLOM Images. The original NLOM optical section (A) is padded and a windowing function is applied (B). A two-dimensional FFT is then performed to obtain the power spectrum (C), which allows for the generation of the frequency histogram (D) to determine predominant fiber angle (PFA) and calculate alignment index (AI). This algorithm is applied to all images within the optical stacks.

Statistical Analysis. Mean PFAs and AIs were calculated for each specimen (n = 4) under four mechanical loading conditions. Differences between the orientation parameters under each mechanical loading condition were determined using the paired Student's *t*-test, with $p < 0.05$ deemed significant. All results are reported as mean ± standard error of the mean (SEM).

Results

Examination of the NLOM images in the central region of unloaded bovine carotid artery specimens reveals a sudden change in fiber orientation just below the endothelial surface. Both collagen (SHG signal) and elastin (TPF signal) fibers shift from a predominantly axial orientation (90°) to largely circumferential (0°) orientation (Fig. 6.3). Examination of the PFA values for all loading conditions reveals a sharp change in collagen fiber angle[2], from an axial orientation just below the endothelial surface, to a circumferential orientation deeper in the medial layer. Furthermore, this shift in fiber angle may be seen by eye in the NLOM image. It is observed that in the optical sections 5 μm inward from the cross-over region (i.e. 5 μm towards the intimal surface), the fibers are aligned predominantly in the axial direction (vertical), whereas the optical section 5 μm outward from the cross-over region (i.e. 5 μm towards the adventitial surface) reveal fibers aligned predominantly in the circumferential direction (horizontal). Calculations of the collagen fiber orientation in the optical sections 5 μm inward from the cross-over region give PFA values of 83 ± 4.4° (mean ± SEM), 86 ± 2.3°, 77 ± 7.8°, and 85 ± 2.5° for the 0%, 10% axial, 10% circumferential, and 10% biaxial loading conditions, respectively (Fig. 6.4, Table 6.1). PFAs in the region 5 μm outward from the cross-over region significantly differed ($p < 0.01$), with values of 7.0 ± 3.8°, 10 ± 2.8°, 8.0 ± 3.8°, and 4.0 ± 2.0° for the four loading conditions, respectively. A similar trend was observed when examining the elastin fiber orientation, as PFA values of 82 ± 4.3°, 87 ± 1.9°, 75 ± 9.6°, and 80 ± 6.2° were calculated for the optical

[2] Results from SHG (collagen fibers) and TPF (elastin fibers) data were not significantly different, and thus for brevity, only the SHG data are presented in the figures on pages 120, 124, and 126.

sections section 5 μm inward for the four loading conditions, respectively, and optical sections 5 μm outward had statistically significant changes ($p < 0.01$) in PFAs of 8.0 ± 2.0°, 13 ± 4.7°, 3.0 ± 1.0°, and 6.0 ± 1.6° for the four strain states, respectively (Fig. 6.4, Table 6.1). It should be noted that the radial positions of the cross-over regions differed in the SHG and TPF optical sections of each specimen, however the differences were small (5.8 ± 1.5 μm), with no noticeable pattern in the four specimens studied.

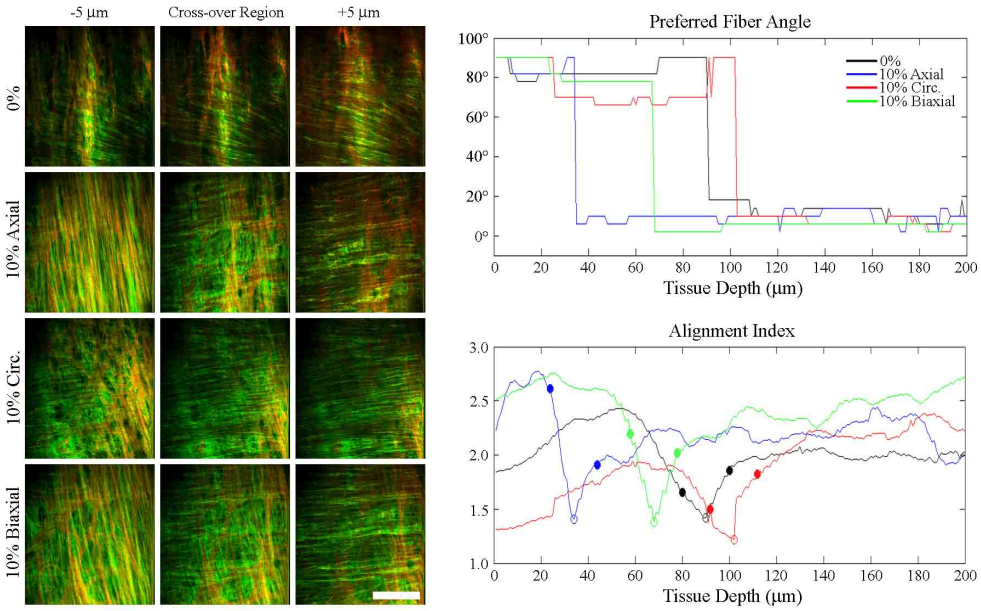

Figure 6.3: Nonlinear Optical Microscopy Images Under Various Strain Conditions. Combined SHG (collagen; green) and TPF (elastin; red) images within a representative arterial specimen from the cross-over region, and ±5 μm from that position, at each of the four strain conditions. (Note: orange/yellow color shows regions giving rise to SHG and TPF signals.) The radial positions of the cross over images are shown by the open circles on the alignment index plots (lower right hand panel); and the solid circles correspond to the positions ±5 μm from the cross over location. It is observed that fibers -5 μm inward from the cross-over region (i.e. towards endothelial surface) are aligned predominantly in the axial direction (vertical, 90°), whereas fibers +5 μm outward from the cross-over region (i.e. towards adventitia) are oriented circumferentially (horizontal, 0°). Such an observation is further supported by evaluation of predominant fiber angle (PFA) as a function of radial position (upper right hand panel). Scale bar represents 50 μm.

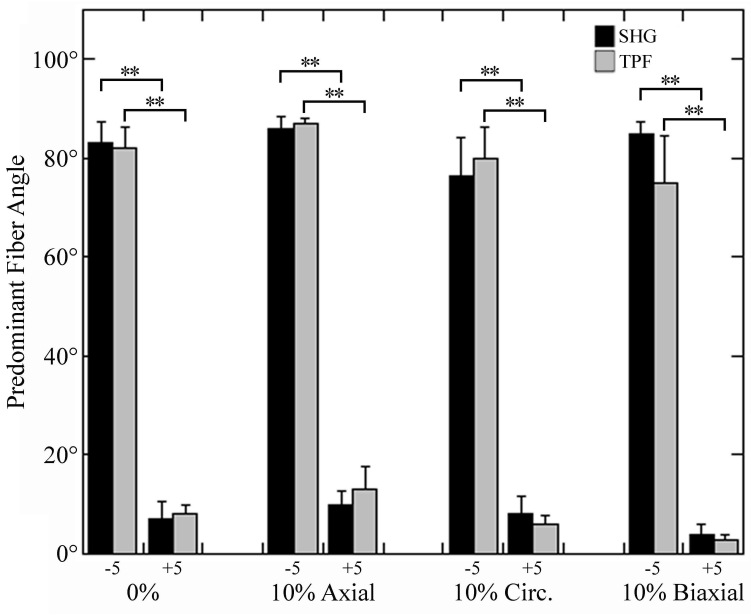

Figure 6.4: Predominant Fiber Angle Near Cross-over Region. The predominant fiber angles were determined ±5 μm from the cross-over region for each optical section (SHG and TPF) at each strain condition. Abrupt changes in fiber angle are observed for all mechanical conditions, with fibers shifting from a predominant axial orientation (90°) to a largely circumferential orientation (0°). Data are means ± SEM of 4 tissue samples. Significant differences ($p < 0.01$) are denoted by double asterisks.

Table 6.1: Collagen and elastin fiber orientations near cross-over region. Data are means ± SEM of 4 tissue samples. SHG: second harmonic generation, TPF: two-photon excited fluorescence, PFA: predominant fiber angle, AI: alignment index.

	0%	10% Axial	10% Circumferential	10% Biaxial
Sub-endothelial Region (-5 μm from cross-over region)				
Collagen (SHG)				
PFA	83 ± 4.4°	86 ± 2.3°	77 ± 7.8°	85 ± 2.5°
AI	1.66 ± 0.03	2.03 ± 0.23	1.44 ± 0.02	1.90 ± 0.25
Elastin (TPF)				
PFA	82 ± 4.3°	87 ± 1.9°	75 ± 9.6°	80 ± 6.2°
AI	1.70 ± 0.06	1.91 ± 0.12	1.48 ± 0.03	2.00 ± 0.09
Inner Medial Region (+5 μm from cross-over region)				
Collagen (SHG)				
PFA	7.0 ± 3.8°	10 ± 2.8°	8.0 ± 3.8°	4.0 ± 2.0°
AI	1.98 ± 0.05	1.77 ± 0.15	1.63 ± 0.13	2.04 ± 0.03
Elastin (TPF)				
PFA	8.0 ± 2.0°	13 ± 4.7°	3.0 ± 1.0°	6.0 ± 1.6°
AI	1.73 ± 0.13	1.77 ± 0.18	1.69 ± 0.12	1.96 ± 0.10

Histological evaluation provided a larger field of view of the arterial specimens and further qualitative evidence that confirms the observations determined from the NLOM images. Transverse and longitudinal sections reveal a region just below the endothelial surface where there is a sharp change in VSMC nuclei orientation that coincides with a change in fiber (collagen and elastin) structural organization in the artery wall (Fig. 6.5). Examination of the micrographs stained with Ehrlich's hematoxylin reveals VSMC nuclei[3] aligned predominantly axially in the sub-endothelial region, followed by an abrupt shift, as the VSMC assume a circumferential orientation deeper in the arterial medial layer (Fig. 6.5; A, D). Note that in transverse histological sections, cell nuclei and fibers appear nearly circular if aligned axially, whereas they are elliptical and elongated if aligned in the circumferential direction. Conversely, in longitudinal sections they are elliptical and elongated if oriented axially and circular if aligned circumferentially. A similar arterial inhomogeneity is observed when examining the elastin fibers (Fig. 6.5; B, E), however, rather than a distinct change in orientation, a change in the structural composition is observed. This is most evident in the longitudinal section (Fig. 5E), as moving outward radially reveals a sudden change in the elastin structure just below the endothelial surface. A similar finding is observed when examining the collagen fibers in the sections stained with picrosirus red (Fig. 6.5; C, F).

[3] Immunohistochemical staining showed that the cells in the sub-endothelial surface expressed markers for smooth muscle actin and desmin, thus confirming that these are VSMC.

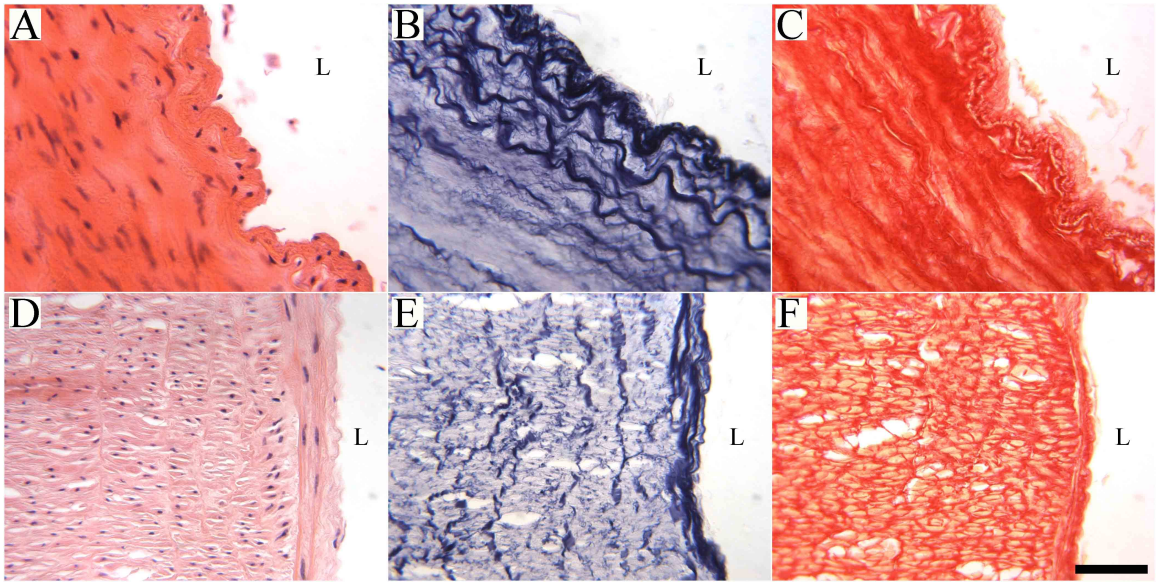

Figure 6.5: Histological Sections of Bovine Common Carotid Artery. Representative micrographs (A – C: transverse; D – E: longitudinal) from a test specimen that were stained with either Ehrlich's hematoxylin [A, D; [130]], an adaptation of Miller's elastin stain [B, E; [131]], or picrosirius red [C, F; [132]], to visualize cell nuclei, elastin, or collagen orientation, respectively. Axially oriented VSMC[6.3] and extracellular matrix fibers are clearly observed just below the intimal surface, with an abrupt shift to a circumferential orientation deeper in the arterial wall. Note that the specimens were fixed in the unloaded condition (0 mmHg). Scale bar denotes 100 μm; L: lumen.

The radial position of the abrupt change in fiber orientation depends strongly on the direction of the applied strain when comparing the four mechanical states (0%, 10% axial, 10% circumferential, 10% biaxial). Applying a 10% axial strain leads to a significant inward shift (i.e. movement closer to the endothelial surface) in the location of the cross-over region when compared to the unloaded case (Fig. 6.3; $p < 0.05$). The fractional change in the distance from the intima to the cross-over region was 0.62 ± 0.13 for collagen (SHG images), and 0.60 ± 0.10 for elastin (TPF images), when normalized to the distance to the cross-over region in the 0% strain state (Fig. 6.6). A 10% biaxial strain also results in a significant inward shift in the radial location of the cross-over region when normalized

against the 0% case (collagen: 0.50 ± 0.08, elastin: 0.57 ± 0.08; $p < 0.01$). In contrast, application of a 10% strain in the circumferential direction revealed a tendency toward an outward shift in the radial location of the cross-over region, however this was not statistically significant (collagen: 1.12 ± 0.26, elastin: 1.54 ± 0.34).

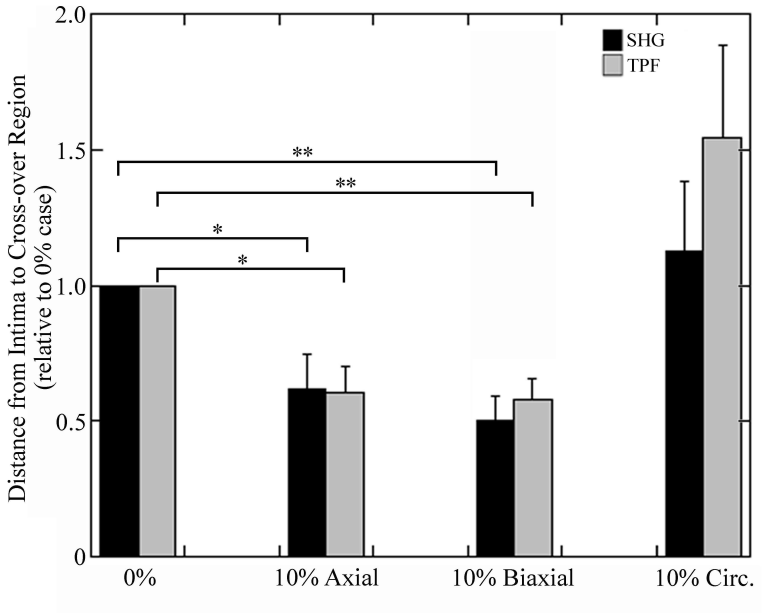

Figure 6.6: Thickness of Axially Oriented Sub-endothelial Region Normalized to Unloaded State. The distance from the intima to the cross-over region was determined for each optical section (SHG and TPF) at each loading condition. Straining the specimens 10% axially or biaxially resulted in a reduction of the thickness of the sub-endothelial region, relative to the unloaded condition. However, applying a 10% circumferential stretch to the specimens resulted in a slight, although not significant, thickening of the region. Data are means ± SEM of 4 tissue samples. Significant differences ($p < 0.05$, $p < 0.01$) are denoted by single and double asterisks, respectively.

Application of the various strain states also leads to substantial changes in the AI for both the axial and circumferentially aligned fiber regions. A general trend of higher alignment in the direction of the load is observed when examining the fiber angle frequency histograms from the SHG optical sections ±5 μm from the cross-over region (Fig. 6.7, Table 6.1). For example, application of a 10% axial strain results in an increase in the AI in the axially aligned region (-5 μm) in comparison to the unloaded state, 2.03 ± 0.23 versus 1.66 ± 0.03, respectively, and an increase in the AI in the region where the fibers are aligned circumferentially (+5 μm), with values of 1.91 ± 0.12 and 1.70 ± 0.06, respectively. Application of a 10% biaxial strain also results in an increase in the AI for the axially aligned region (AI = 1.90 ± 0.25), and furthermore, an increase in the AI for the circumferentially aligned region (AI = 2.00 ± 0.09). However, decreases in the AIs for both the axially and circumferentially aligned regions are observed when a 10% strain in the circumferential direction is applied, with values of 1.44 ± 0.02 and 1.48 ± 0.03, respectively. Similar trends are seen when examining the AI values from the TPF data (Table 6.1).

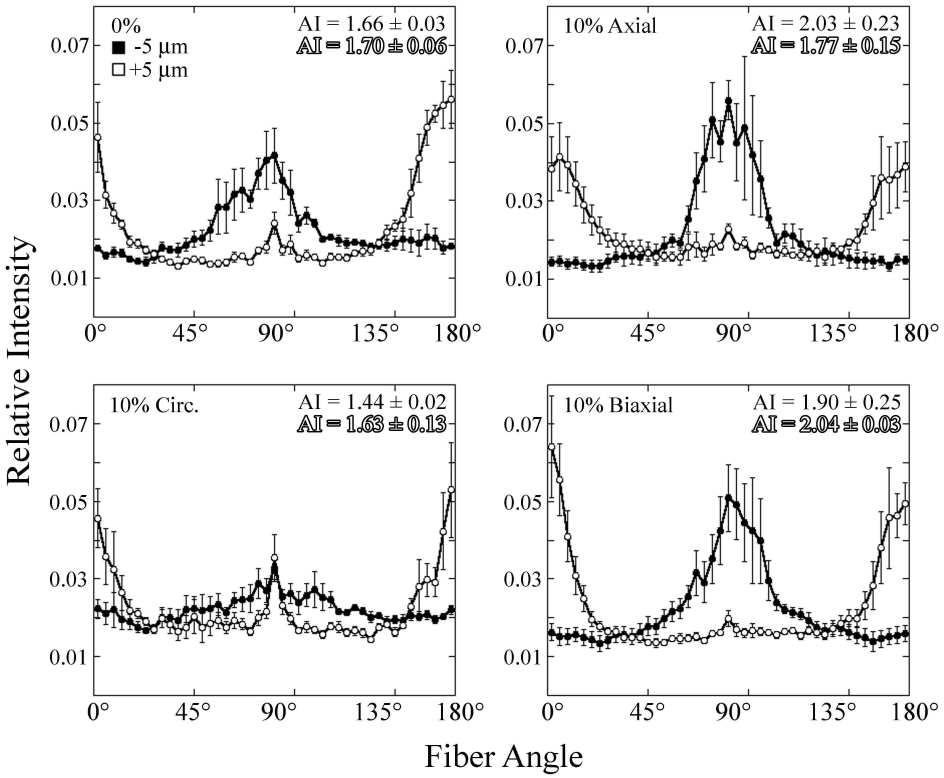

Figure 6.7: Collagen Fiber Alignment Under Various Mechanical Loading Conditions. Analysis of the collagen fiber distribution and alignment indices (AI) from the optical sections -5 μm (black) and +5 μm (white) from the cross-over region reveals the effects of applying varying degrees of strain along orthogonal axes. Applying a 10% axial or biaxial strain resulted in higher AIs for the axially aligned sub-endothelial region (-5 μm) when compared to the 0% strain state (white bars in the two right hand panels). However a 10% strain in the circumferential direction decreased the AI value in that region. The AI values for the circumferentially oriented regions (+5 μm) decreased when a 10% strain was applied in the axial or circumferential direction, yet the value increased when a 10% biaxial strain was applied. Note analysis of the TPF (elastin) images (not shown) shows similar findings; 90° = axial direction and 0°, 180° = circumferential direction. Data are means ± SEM of 4 tissue samples.

Discussion

The purpose of this investigation was to quantify the effects of physiologic loading conditions on fiber alignment in the sub-endothelial axially aligned region. High resolution images were acquired using a custom built NLOM system allowing for analysis of

extracellular matrix fiber orientations in bovine common carotid arteries, under varying levels of strain for, we believe, the first time. The results indicate that the fiber orientation and alignment are highly dependent on the direction of the applied load, and the direction in which the fibers are initially oriented.

Applying mechanical loads to vascular tissue leads to the reorganization of collagen and elastin fibers within the vascular wall, as the constituents bear the applied loads. Our results indicate that higher axial fiber alignment (increased AI values; Fig. 6.7, Table 6.1) is a result of straining the tissue, however only if the load is applied in the axial direction. In contrast, if the load is applied in the circumferential direction, the fibers become less aligned (decreased AI values), an indication that the fibers may be realigning in the direction of the applied load. These results are consistent with previous findings in other soft biological tissue [135, 136]. For example, Lake et al. demonstrated that uniaxial loading of supraspinatus tendon led to significant collagen realignment in the direction of the load, throughout various regions of the tissue [137]. Furthermore, the mechanical response of the tissue was highly dependent on both the unloaded and loaded fiber configurations (e.g. higher initial alignment corresponds to stiffer mechanical response). While mechanical data (stress-strain relationships) were not collected in this investigation, our data suggest that the non-linear, anisotropic mechanical response for vascular tissue is a direct result of fiber orientation [116, 138]. This strongly supports the suggestion of Clark and Glagov [103], that the relatively thin sub-endothelial layer is arranged so as to support loads that are in the axial direction (e.g. axial shear stress from blood flow), while the thicker, predominantly

circumferentially aligned fibers deeper in the vascular wall bear the load of the pulse pressure waves during the cardiac cycle.

There is a strong correlation between the underlying microstructure of a biological tissue and its mechanical properties. For example, it has been shown that tissues are stiffer in the direction that the embedded matrix fibers are aligned [e.g. arteries [116, 138], tendons [137]]. Applied loads lead to local deformations in the microstructure resulting in macroscopic changes (thickening or thinning) of the tissue. For the axial and biaxial strain states, a thinning of the sub-endothelial axial aligned fiber layer was observed, however, a trend towards thickening was noted when a circumferential strain was applied (Fig. 6.6). Such an observation would indicate a negative Poisson's ratio or auxetic behavior, which although not generally accepted for vascular tissue, has been reported [139]. More importantly rather, this result further emphasizes the complex effects of fibers on the mechanical properties of biological tissues. When fibers are oriented in the direction of the applied load, they bear more of the load or are more stressed, resulting in a thinning of the material. However, if the material is multi-layered with fibers not oriented in the direction of the loading, as investigated in this study, then such fibers will bear a minimal proportion of the applied load. Therefore, the stress in this layer(s) is substantially smaller and does not result in a thinning of the layer.

The results further confirm the presence of a sub-endothelial layer of extracellular matrix fibers and VSMC that are aligned longitudinally in vascular tissue. While we have examined only bovine carotid artery, we have seen structural inhomogeneity in the conduit arteries of other species such as the pig [140]. Explanations for the presence of this layer

have been directed toward the complex, in vivo mechanical environment that is imposed on the vasculature. It has been suggested that endothelial cells (EC) on the intimal surface transmit the forces associated with the axial blood flow into the inner medial region [103]. As the axial shear stress in the artery wall decays rapidly with radial position, only a small region of the media is subjected to this component of stress, while the remainder of the media is under circumferential stress due to the cyclic loading of pressure, and resulting circumferential alignment. In human common carotid arteries, typical values of flow-induced axial wall shear stress and pressure-induced circumferential wall stress are approximately 0.7 Pa and 75 kPa, respectively, at systole [141, 142]. Thus, when examining the applied physiologic loads the minimal thickness of the sub-endothelial region in comparison to the thicker circumferentially aligned region of the media is understandable. Furthermore, it might be expected that if the blood flow rate is increased while holding the vessel caliber constant (i.e. increased mean shear stress), then the resulting shear forces would be transmitted more deeply into the medial layer, resulting in a thicker sub-endothelial axially aligned region. Measurements in situations in which mean shear stress is raised, such as downstream from a stenosis or arteriovenous shunt would provide a test for this prediction.

If shear stress is indeed the principle reason for the axial alignment in the components of the inner media, the question arises: why is the transition at its outer edge so abrupt? If it is assumed that the axial tension due to shear stress falls gradually with increasing depth into the media then a similar gradual change in orientation might be expected. On the other hand if a threshold level of stress is necessary to provoke a change in orientation, this could give rise to the sudden change observed. We note that a radial gradient

of circumferential stress may also be present in the inner media despite the existence of residual stresses [which also vary across the arterial wall; [143]]. A definitive test of these speculations would require measurements and or modeling of the balance between pressure induced circumferential stress and flow induced shear stress (both applied and residual) but could provide valuable insight into the mechanisms of mechanotransduction in EC and VSMC both under normal and pathologic conditions.

As the NLOM techniques allowed for simultaneous, independent examination of collagen and elastin fibers, the relationship between these two matrix proteins within the arterial wall could be further investigated. As there was no statistical difference between collagen and elastin fiber orientation data for all strain states, our results support the notion of the interrelated architecture between these two extracellular matrix proteins, as has been described in the main body of the medial layer [103, 144].

We note a number of potential limitations to the study. Firstly, while NLOM provides an excellent means for examining the microstructure of biological tissues, the sub-micron resolution of this technique results in image areas that are quite small (~0.02 mm^2). Thus, it is likely that local heterogeneities within the tissue sample would not be detected. While not presented, analysis of optical sections at various locations on the tissue specimens revealed no significant changes in the depths of the cross-over region, or the PFA, and AI values. Secondly, some variability amongst specimens from different animals was also observed. However, as the error bars in Figure 6.4 (for instance) show, these were acceptably small. Thirdly, it was assumed that images were acquired at the *exact* middle of the specimen following its removal from the microscope stage and subsequent replacement when changing

the strain state. However, as discussed above, the small variation of the measured orientation variables within each specimen ensured that any small deviation from this middle position did not confound the results. Fourthly, in any optical study that analyzes structural orientation, polarization of the incident light may bias the results. In this case, a comparison of values between a tissue sample mounted in the device chamber and orientated normally on the microscope stage and one where the chamber was rotated 90°, both at the same strain state, was performed. Analysis of these results showed no statistical difference in any of the measured variables.

In conclusion, this study provides further insight into structure-function relationships within vascular tissue. The results not only reveal the native fiber and cellular organization, but also their reorganization and realignment under mechanical loading. The methods presented could assist in bridging the gap between the micro- and macro-scales, allowing for a more informed incorporation of microscopic structural information into material models of biological tissues, as described by Sacks [145]. The data presented here may also be of use to enhance the design of tissue-engineered cellular scaffolds for vascular grafts that directly mimic native vessel architecture.

CHAPTER VII

SUMMARY, RECOMMENDATIONS, AND FUTURE DIRECTIONS

The treatment of atherosclerosis has come a long way since Dotter and Grüntzig's seminal works. Technological developments have made considerable advances in treating atherosclerosis; however, it still remains one of the leading, if not the leading cause of death in the United States. Thus, improvements upon current treatments can have a considerable impact on the medical community. The data presented in Chapters II – V present unique information on the role of solid biomechanics in the failure of stents due to restenosis. The findings strongly suggest that the development of neointimal tissue, which can lead to the failure of these devices, is at least partially a result of the high stresses imposed on the artery wall. Alterations in the geometrical design of stents could increase the long-term patency of these implantable medical devices, as this leads to large variations in the biomechanical environment in healthy, tapered, and diseased arteries.

In addition, the results touch on various aspects of this interventional technique (e.g. lesion-specific stenting, patient-specific stenting) that are thought to be the next step for endovascular therapies as a whole. As discussed, the results presented are applicable to the both commercially available stent designs and any future design iterations. In particular, as restenosis usually occurs within 6 months following bare metal stent implantation [29], there is no obvious reason for a permanent prosthesis. Thus, the use of biodegradable materials in manufacturing vascular stents has gained much attention. An effective biodegradable stent would serve to provide enough radial support to restore blood flow to distal tissues, but as

time progresses, it would gradually transfer the load back to the healing artery. Biodegradable materials also serve as excellent reservoirs for the storage of pharmaceutical agents that are currently employed in modern drug-eluting stents. However, prior to their acceptance as a standard treatment option, rigorous computational modeling and experimental testing must be systematically developed and employed to ensure that they can provide enough radial support during cyclic loading, degrade at a controllable and predictable manner to ensure structural integrity, and elute embedded drugs in a controllable and biologically relevant manner. Such comprehensive analysis would then be followed by animal studies (similar to those discussed in Chapter V) to confirm the developed modeling techniques, examine the histopathobiological response (e.g. possible hypersensitivity issues), and, most importantly, their efficacy and safety.

As the characterization of biological tissues is transitioning from purely phenomenological findings to a more structural based analysis, it is imperative to develop proper experimental set-ups to fully capture the tissue microstructure during mechanical loading. The use of nonlinear optical microscopy (NLOM) methods is ideal for such analysis, as it does not require fixation or the application of clearing agents or exogenous dyes to tissue specimens. The data presented in Chapter VI provide high-resolution information on the interrelated architecture between extracellular matrix proteins (collagen and elastin) in bovine carotid artery tissue. Furthermore, the effects of mechanical loading are quantified and provide insight into how these fibrous proteins reorganize in vivo during the cardiac cycle. It should be noted, however, that only a small region of the arterial wall just below the intimal layer was examined. Complete analysis of the microstructure will

require a thorough description of the orientation and organization of the cellular and matrix proteins throughout the thickness of the tissue. Toward this end, the application of developed methods to mechanically remove circumferential layers of a known thickness [143, 146] to this experimental design could yield such information. This would provide critical structural information that could be incorporated into structurally based constitutive models to essentially provide an arterial model that is comprised of *n*-layers. Such models might then serve as better description of the mechanical response of artery tissue and provide a better understanding of the relationship between arterial structure and function.

It has been acknowledged that the use of a homogeneous, nonlinear hyperelastic artery model in the computational studies presented (Chapters II – V) does limit the results. However, it is unlikely that the inclusion of a more complex material model (e.g. heterogeneous, structurally based) would have altered the findings. The stent design that induced higher stresses would likely still induce higher stresses if another arterial material model was employed. Moreover, it would have been extremely computationally demanding. Inclusion of a more complex material model (inclusion of information from Chapter VI) would however change the computed stress and strain values in the artery wall. Such information is extremely valuable for a better understanding of the arterial and cellular response to vascular stenting. Furthermore, it might provide information for the design of future stents or other implantable medical devices and yield quantitative data that could be implemented into theoretical models to better predict tissue adaptations in response to various mechanical stimuli.

The information gained on the arterial pathobiological response to vascular stenting as a result of the solid biomechanical environment is unprecedented, and sets the stage for further studies in stented artery biomechanics. Moreover, the data can be incorporated into future computational models specifically for the purpose of reducing the injury to the arterial following the implantation of stents, and possibly other endovascular devices. Future studies in this area are directed at either the development of novel stent designs or address immediate patient care. In regards to new designs, improvements on current computational models to incorporate various aspects of vascular stenting (e.g. stent design, balloon-expansion, drug elution, biodegradation) need to be developed and integrated. While considerable research efforts have been devoted to each of these aspects individually, incorporation of several aspects with allow for more sophisticated computational models to better predict the outcomes and continual improvements on designs. Direct application to patients focuses on the ideas of "patient-specific" and "lesion-specific" stenting. In particular, the ability to determine the ideal stent design for a given lesion, taking into consideration the vascular and plaque geometry, plaque material constituents, and mechanical loading environment (e.g. hemodynamics, vascular pressure). Thus, the development of clinically functional, computationally based pre-operative planning resources is warranted.

Collectively, these studies provide a multi-modal evaluation of cardiovascular tissue, both healthy and during disease progression. A combination of computational modeling (in silico), experimentation (in vitro), and animal testing (in vivo) were conducted. Such thorough examination is warranted in biomechanics, as it allows for empirical and

measurable evidence of biological phenomena that, in turn, may help form new hypotheses or refine previous ones.

REFERENCES

[1] Chappell, D. C., Varner, S. E., Nerem, R. M., Medford, R. M., and Alexander, R. W., 1998, "Oscillatory shear stress stimulates adhesion molecule expression in cultured human endothelium," Circ Res, **82**(5), pp. 532-539.

[2] LaMack, J. A., Himburg, H. A., Li, X. M., and Friedman, M. H., 2005, "Interaction of wall shear stress magnitude and gradient in the prediction of arterial macromolecular permeability," Ann Biomed Eng, **33**(4), pp. 457-464.

[3] Stary, H. C., Chandler, A. B., Glagov, S., Guyton, J. R., Insull, W., Jr., et al., 1994, "A definition of initial, fatty streak, and intermediate lesions of atherosclerosis. A report from the Committee on Vascular Lesions of the Council on Arteriosclerosis, American Heart Association," Arterioscler Thromb, **14**(5), pp. 840-856.

[4] Stary, H. C., Chandler, A. B., Dinsmore, R. E., Fuster, V., Glagov, S., et al., 1995, "A definition of advanced types of atherosclerotic lesions and a histological classification of atherosclerosis. A report from the Committee on Vascular Lesions of the Council on Arteriosclerosis, American Heart Association," Arterioscler Thromb Vasc Biol, **15**(9), pp. 1512-1531.

[5] Lloyd-Jones, D., Adams, R., Carnethon, M., De Simone, G., Ferguson, T. B., et al., 2009, "Heart disease and stroke statistics--2009 update: a report from the American Heart Association Statistics Committee and Stroke Statistics Subcommittee," Circulation, **119**(3), pp. 480-486.

[6] Booth, J., 1977, "A short history of blood pressure measurement," Proc R Soc Med, **70**(11), pp. 793-799.

[7] Mueller, R. L., and Sanborn, T. A., 1995, "The history of interventional cardiology: cardiac catheterization, angioplasty, and related interventions," Am Heart J, **129**(1), pp. 146-172.

[8] Dotter, C. T., and Judkins, M. P., 1964, "Transluminal treatment of arteriosclerotic obstruction. Description of a new technic and a preliminary report of its application," Circulation, **30**, pp. 654-670.

[9] Newing, A., 1999, *Light, Visible and Invisible, and Its Medical Applications*, Imperial College Press, London.

[10] Gruentzig, A., Myler, R., Hanna, E., and Turina, M., 1977, "Coronary transluminal angioplasty [abstract]," Circulation, **84**, pp. 55-56.

[11] Hurst, J. W., 1986, "The first coronary angioplasty as described by Andreas Gruentzig," Am J Cardiol, **57**(1), pp. 185-186.

[12] Castaneda-Zuniga, W. R., Formanek, A., Tadavarthy, M., Vlodaver, Z., Edwards, J. E., et al., 1980, "The mechanism of balloon angioplasty," Radiology, **135**(3), pp. 565-571.

[13] Dotter, C. T., 1969, "Transluminally-placed coilspring endarterial tube grafts. Long-term patency in canine popliteal artery," Invest Radiol, **4**(5), pp. 329-332.

[14] Payne, M. M., 2001, "Charles Theodore Dotter. The father of intervention," Tex Heart Inst J, **28**(1), pp. 28-38.

[15] Dotter, C. T., Buschmann, R. W., McKinney, M. K., and Rosch, J., 1983, "Transluminal expandable nitinol coil stent grafting: preliminary report," Radiology, **147**(1), pp. 259-260.

[16] Maass, D., Zollikofer, C. L., Largiader, F., and Senning, A., 1984, "Radiological follow-up of transluminally inserted vascular endoprostheses: an experimental study using expanding spirals," Radiology, **152**(3), pp. 659-663.

[17] Charnsangavej, C., Carrasco, C. H., Wallace, S., Wright, K. C., Ogawa, K., et al., 1986, "Stenosis of the vena cava: preliminary assessment of treatment with expandable metallic stents," Radiology, **161**(2), pp. 295-298.

[18] Wright, K. C., Wallace, S., Charnsangavej, C., Carrasco, C. H., and Gianturco, C., 1985, "Percutaneous endovascular stents: an experimental evaluation," Radiology, **156**(1), pp. 69-72.

[19] Palmaz, J. C., Sibbitt, R. R., Reuter, S. R., Tio, F. O., and Rice, W. J., 1985, "Expandable intraluminal graft: a preliminary study. Work in progress," Radiology, **156**(1), pp. 73-77.

[20] Schatz, R. A., Palmaz, J. C., Tio, F. O., Garcia, F., Garcia, O., et al., 1987, "Balloon-expandable intracoronary stents in the adult dog," Circulation, **76**(2), pp. 450-457.

[21] Serruys, P. W., Kutryk, M. J., and Ong, A. T., 2006, "Coronary-artery stents," N Engl J Med, **354**(5), pp. 483-495.

[22] Sigwart, U., Puel, J., Mirkovitch, V., Joffre, F., and Kappenberger, L., 1987, "Intravascular stents to prevent occlusion and restenosis after transluminal angioplasty," N Engl J Med, **316**(12), pp. 701-706.

[23] Schatz, R. A., Baim, D. S., Leon, M., Ellis, S. G., Goldberg, S., et al., 1991, "Clinical experience with the Palmaz-Schatz coronary stent. Initial results of a multicenter study," Circulation, **83**(1), pp. 148-161.

[24] Fischman, D. L., Leon, M. B., Baim, D. S., Schatz, R. A., Savage, M. P., et al., 1994, "A randomized comparison of coronary-stent placement and balloon angioplasty in the treatment of coronary artery disease," N Engl J Med, **331**(8), pp. 496-501.

[25] Macaya, C., Serruys, P. W., Ruygrok, P., Suryapranata, H., Mast, G., et al., 1996, "Continued benefit of coronary stenting versus balloon angioplasty: one-year clinical follow-up of Benestent trial. Benestent Study Group," J Am Coll Cardiol, **27**(2), pp. 255-261.

[26] Thom, T., Haase, N., Rosamond, W., Howard, V. J., Rumsfeld, J., et al., 2006, "Heart disease and stroke statistics--2006 update: a report from the American Heart Association Statistics Committee and Stroke Statistics Subcommittee," Circulation, **113**(6), pp. E85-E151.

[27] Edelman, E. R., and Rogers, C., 1998, "Pathobiologic responses to stenting," Am J Cardiol, **81**(7A), pp. 4E-6E.

[28] Versaci, F., Gaspardone, A., Tomai, F., Crea, F., Chiariello, L., et al., 1997, "A comparison of coronary-artery stenting with angioplasty for isolated stenosis of the proximal left anterior descending coronary artery," N Engl J Med, **336**(12), pp. 817-822.

[29] Kastrati, A., Mehilli, J., Dirschinger, J., Pache, J., Ulm, K., et al., 2001, "Restenosis after coronary placement of various stent types," Am J Cardiol, **87**(1), pp. 34-39.

[30] Kastrati, A., Dibra, A., Eberle, S., Mehilli, J., Suarez de Lezo, J., et al., 2005, "Sirolimus-eluting stents vs paclitaxel-eluting stents in patients with coronary artery disease: meta-analysis of randomized trials," JAMA, **294**(7), pp. 819-825.

[31] Iakovou, I., Schmidt, T., Bonizzoni, E., Ge, L., Sangiorgi, G. M., et al., 2005, "Incidence, predictors, and outcome of thrombosis after successful implantation of drug-eluting stents," JAMA, **293**(17), pp. 2126-2130.

[32] Nebeker, J. R., Virmani, R., Bennett, C. L., Hoffman, J. M., Samore, M. H., et al., 2006, "Hypersensitivity cases associated with drug-eluting coronary stents: a review of available cases from the Research on Adverse Drug Events and Reports (RADAR) project," J Am Coll Cardiol, **47**(1), pp. 175-181.

[33] Virmani, R., Liistro, F., Stankovic, G., Di Mario, C., Montorfano, M., et al., 2002, "Mechanism of late in-stent restenosis after implantation of a paclitaxel derivate-eluting polymer stent system in humans," Circulation, **106**(21), pp. 2649-2651.

[34] Migliavacca, F., Petrini, L., Colombo, M., Auricchio, F., and Pietrabissa, R., 2002, "Mechanical behavior of coronary stents investigated through the finite element method," J Biomech, **35**(6), pp. 803-811.

[35] Schwartz, R. S., Huber, K. C., Murphy, J. G., Edwards, W. D., Camrud, A. R., et al., 1992, "Restenosis and the proportional neointimal response to coronary artery injury: results in a porcine model," J Am Coll Cardiol, **19**(2), pp. 267-274.

[36] Bedoya, J., Meyer, C. A., Timmins, L. H., Moreno, M. R., and Moore, J. E., 2006, "Effects of stent design parameters on normal artery wall mechanics," J Biomech Eng, **128**(5), pp. 757-765.

[37] Berry, J. L., Manoach, E., Mekkaoui, C., Rolland, P. H., Moore, J. E., Jr., et al., 2002, "Hemodynamics and wall mechanics of a compliance matching stent: in vitro and in vivo analysis," J Vasc Interv Radiol, **13**(1), pp. 97-105.

[38] Vorp, D. A., Peters, D. G., and Webster, M. W., 1999, "Gene expression is altered in perfused arterial segments exposed to cyclic flexure ex vivo," Ann Biomed Eng, **27**(3), pp. 366-371.

[39] Sumpio, B. E., and Banes, A. J., 1988, "Prostacyclin synthetic activity in cultured aortic endothelial cells undergoing cyclic mechanical deformation," Surgery, **104**(2), pp. 383-389.

[40] Sumpio, B. E., Banes, A. J., Levin, L. G., and Johnson, G., Jr., 1987, "Mechanical stress stimulates aortic endothelial cells to proliferate," J Vasc Surg, **6**(3), pp. 252-256.

[41] LaDisa, J. F., Jr., Olson, L. E., Molthen, R. C., Hettrick, D. A., Pratt, P. F., et al., 2005, "Alterations in wall shear stress predict sites of neointimal hyperplasia after stent implantation in rabbit iliac arteries," Am J Physiol Heart Circ Physiol, **288**(5), pp. H2465-H2475.

[42] He, Y., Duraiswamy, N., Frank, A. O., and Moore, J. E., Jr., 2005, "Blood flow in stented arteries: a parametric comparison of strut design patterns in three dimensions," J Biomech Eng, **127**(4), pp. 637-647.

[43] Berry, J. L., Santamarina, A., Moore, J. E., Jr., Roychowdhury, S., and Routh, W. D., 2000, "Experimental and computational flow evaluation of coronary stents," Ann Biomed Eng, **28**(4), pp. 386-398.

[44] Holzapfel, G. A., Stadler, M., and Gasser, T. C., 2005, "Changes in the mechanical environment of stenotic arteries during interaction with stents: computational assessment of parametric stent designs," J Biomech Eng, **127**(1), pp. 166-180.

[45] Lally, C., Dolan, F., and Prendergast, P. J., 2005, "Cardiovascular stent design and vessel stresses: a finite element analysis," J Biomech, **38**(8), pp. 1574-1581.

[46] Reddy, J. N., 2006, *An Introduction to the Finite Element Method*, McGraw-Hill, New York.

[47] Higashida, R. T., Meyers, P. M., Phatouros, C. C., Connors, J. J., 3rd, Barr, J. D., et al., 2004, "Reporting standards for carotid artery angioplasty and stent placement," Stroke, **35**(5), pp. E112-E134.

[48] Humphrey, J. D., Kang, T., Sakarda, P., and Anjanappa, M., 1993, "Computer-aided vascular experimentation: a new electromechanical test system," Ann Biomed Eng, **21**(1), pp. 33-43.

[49] Harker, L. A., 1987, "Role of platelets and thrombosis in mechanisms of acute occlusion and restenosis after angioplasty," Am J Cardiol, **60**(3), pp. 20B-28B.

[50] Serruys, P. W., and Kutryk, M. J., 2000, *Handbook of Coronary Stents*, Martin Dunitz Ltd., London.

[51] Rosamond, W., Flegal, K., Friday, G., Furie, K., Go, A., et al., 2007, "Heart disease and stroke statistics--2007 update: a report from the American Heart Association Statistics Committee and Stroke Statistics Subcommittee," Circulation, **115**(5), pp. E69-E171.

[52] Bosiers, M., Deloose, K., Verbist, J. R., and Peeters, P., 2005, "Carotid artery stenting: which stent for which lesion?," Vascular, **13**(4), pp. 205-210.

[53] Rogers, C., Tseng, D. Y., Squire, J. C., and Edelman, E. R., 1999, "Balloon-artery interactions during stent placement: a finite element analysis approach to pressure, compliance, and stent design as contributors to vascular injury," Circulation Research, **84**(4), pp. 378-383**.**

[54] Serruys, P. W., and Kukreja, N., 2006, "Late stent thrombosis in drug-eluting stents: return of the 'VB syndrome'," Nature Clinical Practice Cardiovascular Medicine, **3**(12), p. 637.

[55] Holzapfel, G. A., Stadler, M., and Schulze-Bauer, C. A., 2002, "A layer-specific three-dimensional model for the simulation of balloon angioplasty using magnetic resonance imaging and mechanical testing," Annals of Biomedical Engineering, **30**(6), pp. 753-767.

[56] Timmins, L. H., Moreno, M. R., Meyer, C. A., Criscione, J. C., Rachev, A., et al., 2007, "Stented artery biomechanics and device design optimization," Med Biol Eng Comput, **45**(5), pp. 505-513.

[57] Zubaid, M., Buller, C., and Mancini, G. B., 2002, "Normal angiographic tapering of the coronary arteries," Can J Cardiol, **18**(9), pp. 973-980.

[58] Humphrey, J. D., 2002, *Cardiovascular Solid Mechanics: Cells, Tissues, and Organs*, Springer, New York.

[59] Milnor, W., 1989, *Hemodynamics*, Williams & Wilkins, Baltimore.

[60] Farb, A., Weber, D. K., Kolodgie, F. D., Burke, A. P., and Virmani, R., 2002, "Morphological predictors of restenosis after coronary stenting in humans," Circulation, **105**(25), pp. 2974-2980.

[61] Indolfi, C., Torella, D., Coppola, C., Stabile, E., Esposito, G., et al., 2002, "Rat carotid artery dilation by PTCA balloon catheter induces neointima formation in presence of IEL rupture," Am J Physiol Heart Circ Physiol, **283**(2), pp. H760-H767.

[62] Cheng, C. P., Wilson, N. M., Hallett, R. L., Herfkens, R. J., and Taylor, C. A., 2006, "In vivo MR angiographic quantification of axial and twisting deformations of the superficial femoral artery resulting from maximum hip and knee flexion," J Vasc Interv Radiol, **17**(6), pp. 979-987.

[63] Ding, Z., and Friedman, M. H., 2000, "Quantification of 3-D coronary arterial motion using clinical biplane cineangiograms," Int J Card Imaging, **16**(5), pp. 331-346.

[64] Bedoya, J., 2005, "Stent design and arterial mechanics: parameterization tools using the finite element method," M.S. thesis, Dept. of Biomedical Engineering, Texas A&M University, College Station, TX.

[65] Joner, M., Finn, A. V., Farb, A., Mont, E. K., Kolodgie, F. D., et al., 2006, "Pathology of drug-eluting stents in humans: delayed healing and late thrombotic risk," J Am Coll Cardiol, **48**(1), pp. 193-202.

[66] Duda, S. H., Bosiers, M., Lammer, J., Scheinert, D., Zeller, T., et al., 2006, "Drug-eluting and bare nitinol stents for the treatment of atherosclerotic lesions in the superficial femoral artery: long-term results from the SIROCCO trial," J Endovasc Ther, **13**(6), pp. 701-710.

[67] Kiousis, D. E., Gasser, T. C., and Holzapfel, G. A., 2007, "A numerical model to study the interaction of vascular stents with human atherosclerotic lesions," Ann Biomed Eng, **35**(11), pp. 1857-1869.

[68] Pulido, M. A., Angiolillo, D. J., and Costa, M. A., 2004, "Imaging of atherosclerotic plaque," Int J Cardiovasc Imaging, **20**(6), pp. 553-559.

[69] Holzapfel, G. A., Sommer, G., and Regitnig, P., 2004, "Anisotropic mechanical properties of tissue components in human atherosclerotic plaques," J Biomech Eng, **126**(5), pp. 657-665.

[70] Salunke, N. V., Topoleski, L. D., Humphrey, J. D., and Mergner, W. J., 2001, "Compressive stress-relaxation of human atherosclerotic plaque," J Biomed Mater Res, **55**(2), pp. 236-241.

[71] Hayashi, K., 1993, "Experimental approaches on measuring the mechanical properties and constitutive laws of arterial walls," J Biomech Eng, **115**(4B), pp. 481-488.

[72] Lyon, R. T., Zarins, C. K., Lu, C. T., Yang, C. F., and Glagov, S., 1987, "Vessel, plaque, and lumen morphology after transluminal balloon angioplasty. Quantitative study in distended human arteries," Arteriosclerosis, **7**(3), pp. 306-314.

[73] Migliavacca, F., Petrini, L., Massarotti, P., Schievano, S., Auricchio, F., et al., 2004, "Stainless and shape memory alloy coronary stents: a computational study on the interaction with the vascular wall," Biomech Model Mechanobiol, **2**(4), pp. 205-217.

[74] Matsumoto, T., and Hayashi, K., 1996, "Stress and strain distribution in hypertensive and normotensive rat aorta considering residual strain," J Biomech Eng, **118**(1), pp. 62-73.

[75] Smith, J. D., Davies, N., Willis, A. I., Sumpio, B. E., and Zilla, P., 2001, "Cyclic stretch induces the expression of vascular endothelial growth factor in vascular smooth muscle cells," Endothelium, **8**(1), pp. 41-48.

[76] Colombo, A., Hall, P., Nakamura, S., Almagor, Y., Maiello, L., et al., 1995, "Intracoronary stenting without anticoagulation accomplished with intravascular ultrasound guidance," Circulation, **91**(6), pp. 1676-1688.

[77] Murray, A., Allen, V., and Bennett, M. K., 1998, "Validation of an automated technique for determining the mechanical characteristics of coronary arteries during balloon angioplasty: laboratory assessment with necropsy segments," Heart, **79**(6), pp. 608-612.

[78] Gasser, T. C., and Holzapfel, G. A., 2007, "Modeling plaque fissuring and dissection during balloon angioplasty intervention," Ann Biomed Eng, **35**(5), pp. 711-723.

[79] Duraiswamy, N., Schoephoerster, R. T., Moreno, M. R., and Moore, J. E., Jr., 2007, "Stented artery flow patterns and their effects on the artery wall," Annu Rev of Fluid Mech, **39**, pp. 357-382.

[80] Duraiswamy, N., Jayachandran, B., Byrne, J., Moore, J. E., Jr., and Schoephoerster, R. T., 2005, "Spatial distribution of platelet deposition in stented arterial models under physiologic flow," Ann Biomed Eng, **33**(12), pp. 1767-1777.

[81] Robaina, S., Jayachandran, B., He, Y., Frank, A., Moreno, M. R., et al., 2003, "Platelet adhesion to simulated stented surfaces," J Endovasc Ther, **10**(5), pp. 978-986.

[82] Kroll, M. H., Hellums, J. D., McIntire, L. V., Schafer, A. I., and Moake, J. L., 1996, "Platelets and shear stress," Blood, **88**(5), pp. 1525-1541.

[83] Moazzam, F., DeLano, F. A., Zweifach, B. W., and Schmid-Schonbein, G. W., 1997, "The leukocyte response to fluid stress," Proc Natl Acad Sci U S A, **94**(10), pp. 5338-5343.

[84] Siow, R. C., Mallawaarachchi, C. M., and Weissberg, P. L., 2003, "Migration of adventitial myofibroblasts following vascular balloon injury: insights from in vivo gene transfer to rat carotid arteries," Cardiovasc Res, **59**(1), pp. 212-221.

[85] Li, L., Couse, T. L., Deleon, H., Xu, C. P., Wilcox, J. N., et al., 2002, "Regulation of syndecan-4 expression with mechanical stress during the development of angioplasty-induced intimal thickening," J Vasc Surg, **36**(2), pp. 361-370.

[86] Timmins, L. H., Meyer, C. A., Moreno, M. R., and Moore, J. E., Jr., 2008, "Mechanical modeling of stents deployed in tapered arteries," Ann Biomed Eng, **36**(12), pp. 2042-2050.

[87] Timmins, L. H., Meyer, C. A., Moreno, M. R., and Moore, J. E., 2008, "Effects of stent design and atherosclerotic plaque composition on arterial wall biomechanics," J Endovasc Ther, **15**(6), pp. 643-654.

[88] Lemos, P. A., Moulin, B., Perin, M. A., Oliveira, L. A., Arruda, J. A., et al., 2009, "Randomized evaluation of two drug-eluting stents with identical metallic platform and biodegradable polymer but different agents (paclitaxel or sirolimus) compared against bare stents: 1-year results of the PAINT trial," Catheter Cardiovasc Interv, **74**(5), pp. 665-673.

[89] Schomig, A., Dibra, A., Windecker, S., Mehilli, J., Suarez de Lezo, J., et al., 2007, "A meta-analysis of 16 randomized trials of sirolimus-eluting stents versus paclitaxel-eluting stents in patients with coronary artery disease," J Am Coll Cardiol, **50**(14), pp. 1373-1380.

[90] Chuong, C. J., and Fung, Y. C., 1984, "Compressibility and constitutive equation of arterial wall in radial compression experiments," J Biomech, **17**(1), pp. 35-40.

[91] Han, H. C., and Fung, Y. C., 1995, "Longitudinal strain of canine and porcine aortas," J Biomech, **28**(5), pp. 637-641.

[92] Schwartz, R. S., Edwards, W. D., Bailey, K. R., Camrud, A. R., Jorgenson, M. A., et al., 1994, "Differential neointimal response to coronary artery injury in pigs and dogs. Implications for restenosis models," Arterioscler Thromb, **14**(3), pp. 395-400.

[93] Verheye, S., Salame, M. Y., Robinson, K. A., Post, M. J., Carrozza, J. P., Jr., et al., 1999, "Short- and long-term histopathologic evaluation of stenting using a self-expanding nitinol stent in pig carotid and iliac arteries," Catheter Cardiovasc Interv, **48**(3), pp. 316-323.

[94] Kornowski, R., Hong, M. K., Tio, F. O., Bramwell, O., Wu, H., et al., 1998, "In-stent restenosis: contributions of inflammatory responses and arterial injury to neointimal hyperplasia," J Am Coll Cardiol, **31**(1), pp. 224-230.

[95] Virmani, R., and Farb, A., 1999, "Pathology of in-stent restenosis," Curr Opin Lipidol, **10**(6), pp. 499-506.

[96] Farb, A., Sangiorgi, G., Carter, A. J., Walley, V. M., Edwards, W. D., et al., 1999, "Pathology of acute and chronic coronary stenting in humans," Circulation, **99**(1), pp. 44-52.

[97] Rolland, P. H., Charifi, A. B., Verrier, C., Bodard, H., Friggi, A., et al., 1999, "Hemodynamics and wall mechanics after stent placement in swine iliac arteries: comparative results from six stent designs," Radiology, **213**(1), pp. 229-246.

[98] Hoffmann, R., Mintz, G. S., Dussaillant, G. R., Popma, J. J., Pichard, A. D., et al., 1996, "Patterns and mechanisms of in-stent restenosis. A serial intravascular ultrasound study," Circulation, **94**(6), pp. 1247-1254.

[99] Humphrey, J. D., 2008, "Vascular adaptation and mechanical homeostasis at tissue, cellular, and sub-cellular levels," Cell Biochem Biophys, **50**(2), pp. 53-78.

[100] Rachev, A., Manoach, E., Berry, J., and Moore, J. E., Jr., 2000, "A model of stress-induced geometrical remodeling of vessel segments adjacent to stents and artery/graft anastomoses," J Theor Biol, **206**(3), pp. 429-443.

[101] Schwartz, R. S., Murphy, J. G., Edwards, W. D., Camrud, A. R., Vliestra, R. E., et al., 1990, "Restenosis after balloon angioplasty. A practical proliferative model in porcine coronary arteries," Circulation, **82**(6), pp. 2190-2200.

[102] Zarins, C. K., and Taylor, C. A., 2009, "Endovascular device design in the future: transformation from trial and error to computational design," J Endovasc Ther, **16** Suppl 1, pp. I12-I21.

[103] Clark, J. M., and Glagov, S., 1985, "Transmural organization of the arterial media. The lamellar unit revisited," Arteriosclerosis, **5**(1), pp. 19-34.

[104] Dingemans, K. P., Teeling, P., Lagendijk, J. H., and Becker, A. E., 2000, "Extracellular matrix of the human aortic media: an ultrastructural histochemical and immunohistochemical study of the adult aortic media," Anat Rec, **258**(1), pp. 1-14.

[105] Arner, A., and Uvelius, B., 1982, "Force-velocity characteristics and active tension in relation to content and orientation of smooth muscle cells in aortas from normotensive and spontaneous hypertensive rats," Circ Res, **50**(6), pp. 812-821.

[106] Gross, L., Epstein, E. Z., and Kugel, M. A., 1934, "Histology of coronary arteries and their branches in the human heart," Am J Pathol, **10**, pp. 253-274.

[107] Wolinsky, H., and Glagov, S., 1967, "A lamellar unit of aortic medial structure and function in mammals," Circ Res, **20**(1), pp. 99-111.

[108] Bierring, F., and Kobayasi, T., 1963, "Electron microscopy of the normal rabbit aorta," Acta Pathol Microbiol Scand, **57**, pp. 154-168.

[109] Osborne-Pellegrin, M. J., 1978, "Some ultrastructural characteristics of the renal artery and abdominal aorta in the rat," J Anat, **125**(Pt 3), pp. 641-652.

[110] Wolkoff, K., 1923, "Uber die histologische Struktur der Coronararterien des menschlichen Herzens," Virchows Arch Pathol Anat Physiol, **252**, pp. 208-228.

[111] Stehbens, W. E., 1960, "Focal intimal proliferation in the cerebral arteries," Am J Pathol, **36**, pp. 289-301.

[112] Todd, M. E., and Friedman, S. M., 1972, "The ultrastructure of peripheral arteries during the development of DOCA hypertension in the rat," Z Zellforsch Mikrosk Anat, **128**(4), pp. 538-554.

[113] Shimada, T., Sato, F., Zhang, L., Ina, K., and Kitamura, H., 1993, "Three-dimensional visualization of the aorta and elastic cartilage after removal of extracellular ground substance with a modified NaOH maceration method," J Electron Microsc (Tokyo), **42**(5), pp. 328-333.

[114] Smith, P., 1976, "A comparison of the orientation of elastin fibers in the elastic laminae of the pulmonary trunk and aorta of rabbits using the scanning electron microscope," Lab Invest, **35**(6), pp. 525-529.

[115] Zulliger, M. A., Fridez, P., Hayashi, K., and Stergiopulos, N., 2004, "A strain energy function for arteries accounting for wall composition and structure," J Biomech, **37**(7), pp. 989-1000.

[116] Holzapfel, G. A., and Gasser, T. C., 2000, "A new constitutive framework for arterial wall mechanics and a comparative study of material models," J. Elasticity, **61**, pp. 1-48.

[117] Finlay, H. M., Whittaker, P., and Canham, P. B., 1998, "Collagen organization in the branching region of human brain arteries," Stroke, **29**(8), pp. 1595-1601.

[118] Liu, Z. Q., Rangayyan, R. M., and Frank, C. B., 1991, "Statistical analysis of collagen alignment in ligaments by scale-space analysis," IEEE Trans Biomed Eng, **38**(6), pp. 580-588.

[119] Chaudhuri, S., Nguyen, H., Rangayyan, R. M., Walsh, S., and Frank, C. B., 1987, "A Fourier domain directional filtering method for analysis of collagen alignment in ligaments," IEEE Trans Biomed Eng, **34**(7), pp. 509-518.

[120] Liao, K. X., Frater, R. W., Stevenson-Smith, W., Nikolic, S. D., Macaluso, F., et al., 1991, "Two-dimensional mechanical and ultrastructural correlates of bovine pericardium for prosthetic valves," ASAIO Trans, **37**(3), pp. M349-M351.

[121] Liao, J., Yang, L., Grashow, J., and Sacks, M. S., 2005, "Molecular orientation of collagen in intact planar connective tissues under biaxial stretch," Acta Biomater, **1**(1), pp. 45-54.

[122] Joyce, E. M., Liao, J., Schoen, F. J., Mayer, J. E., Jr., and Sacks, M. S., 2009, "Functional collagen fiber architecture of the pulmonary heart valve cusp," Ann Thorac Surg, **87**(4), pp. 1240-1249.

[123] Sacks, M. S., Smith, D. B., and Hiester, E. D., 1997, "A small angle light scattering device for planar connective tissue microstructural analysis," Ann Biomed Eng, **25**(4), pp. 678-689.

[124] Moger, C. J., Arkill, K. P., Barrett, R., Bleuet, P., Ellis, R. E., et al., 2009, "Cartilage collagen matrix reorientation and displacement in response to surface loading," J Biomech Eng, **131**(3), pp. 031008-1-031008-9.

[125] Campagnola, P. J., and Loew, L. M., 2003, "Second-harmonic imaging microscopy for visualizing biomolecular arrays in cells, tissues and organisms," Nat Biotechnol, **21**(11), pp. 1356-1360.

[126] Zipfel, W. R., Williams, R. M., and Webb, W. W., 2003, "Nonlinear magic: multiphoton microscopy in the biosciences," Nat Biotechnol, **21**(11), pp. 1369-1377.

[127] Hu, J. J., Humphrey, J. D., and Yeh, A. T., 2008, "Characterization of engineered tissue development under biaxial stretch using nonlinear optical microscopy," Tissue Eng Part A, **15**(7), pp. 1553-1564.

[128] Rubbens, M. P., Driessen-Mol, A., Boerboom, R. A., Koppert, M. M., van Assen, H. C., et al., 2009, "Quantification of the temporal evolution of collagen orientation in mechanically conditioned engineered cardiovascular tissues," Ann Biomed Eng, **37**(7), pp. 1263-1272.

[129] Larson, A. M., and Yeh, A. T., 2006, "Ex vivo characterization of sub-10-fs pulses," Opt Lett, **31**(11), pp. 1681-1683.

[130] Gill, G. W., Frost, J. K., and Miller, K. A., 1974, "A new formula for a half-oxidized hematoxylin solution that neither overstains nor requires differentiation," Acta Cytol, **18**(4), pp. 300-311.

[131] Miller, P. J., 1971, "An elastin stain," Med Lab Technol, **28**(2), pp. 148-149.

[132] Sweat, F., Puchtler, H., and Rosenthal, S. I., 1964, "Sirius red f3ba as a stain for connective tissue," Arch Pathol, **78**, pp. 69-72.

[133] Nishimura, T., and Ansell, M. P., 2002, "Fast Fourier transform and filtered image analyses of fiber orientation in OSB," Wood Sci Technol, **36**(4), pp. 287-307.

[134] Ng, C. P., and Swartz, M. A., 2006, "Mechanisms of interstitial flow-induced remodeling of fibroblast-collagen cultures," Ann Biomed Eng, **34**(3), pp. 446-454.

[135] Guerin, H. A., and Elliott, D. M., 2006, "Degeneration affects the fiber reorientation of human annulus fibrosus under tensile load," J Biomech, **39**(8), pp. 1410-1418.

[136] Tower, T. T., Neidert, M. R., and Tranquillo, R. T., 2002, "Fiber alignment imaging during mechanical testing of soft tissues," Ann Biomed Eng, **30**(10), pp. 1221-1233.

[137] Lake, S. P., Miller, K. S., Elliott, D. M., and Soslowsky, L. J., 2009, "Effect of fiber distribution and realignment on the nonlinear and inhomogeneous mechanical properties of human supraspinatus tendon under longitudinal tensile loading," J Orthop Res, **27**(12), pp. 1596-1602.

[138] Gasser, T. C., Ogden, R. W., and Holzapfel, G. A., 2006, "Hyperelastic modelling of arterial layers with distributed collagen fibre orientations," J. R. Soc. Interface, **3**, pp. 15-35.

[139] Tickner, E. G., and Sacks, A. H., 1967, "A theory for the static elastic behavior of blood vessels," Biorheology, **4**(4), pp. 151-168.

[140] Stergiopulos, N., Vulliemoz, S., Rachev, A., Meister, J. J., and Greenwald, S. E., 2001, "Assessing the homogeneity of the elastic properties and composition of the pig aortic media," J Vasc Res, **38**(3), pp. 237-246.

[141] Delfino, A., Stergiopulos, N., Moore, J. E., Jr., and Meister, J. J., 1997, "Residual strain effects on the stress field in a thick wall finite element model of the human carotid bifurcation," J Biomech, **30**(8), pp. 777-786.

[142] Ku, D. N., Giddens, D. P., Zarins, C. K., and Glagov, S., 1985, "Pulsatile flow and atherosclerosis in the human carotid bifurcation. Positive correlation between plaque location and low oscillating shear stress," Arteriosclerosis, **5**(3), pp. 293-302.

[143] Greenwald, S. E., Moore, J. E., Jr., Rachev, A., Kane, T. P., and Meister, J. J., 1997, "Experimental investigation of the distribution of residual strains in the artery wall," J Biomech Eng, **119**(4), pp. 438-444.

[144] O'Connell, M. K., Murthy, S., Phan, S., Xu, C., Buchanan, J., et al., 2008, "The three-dimensional micro- and nanostructure of the aortic medial lamellar unit measured using 3D confocal and electron microscopy imaging," Matrix Biol, **27**(3), pp. 171-181.

[145] Sacks, M. S., 2003, "Incorporation of experimentally-derived fiber orientation into a structural constitutive model for planar collagenous tissues," J Biomech Eng, **125**(2), pp. 280-287.

[146] Timmins, L. H., Evagora, C. A., Moore, J. E., Jr., and Greenwald, S. E., June 2008, "Experimental investigation of mechanical and structural inhomogeneity in bovine carotid arteries," ASME 2008 Summer Bioengineering Conference, Marco Island, Florida, USA.

APPENDIX A

STENT SCORING CRITERIA FOR HISTOPATHOLOGIC EVALUATION[1]

Injury Score[2]

0 – stent strut within neointima but not in contact with the IEL

1 – stent strut in contact with the IEL

2 – stent strut penetrating the IEL and into the media but not contacting the EEL

3 – stent strut penetrating the media and contacting the EEL

4 – stent strut penetrating the EEL

Results are expressed as: 0 = no injury; 1 = minimal injury; 2 = mild injury; 3 = moderate injury; and 4 = severe injury.

Inflammation Score[3]

0 – no inflammatory cells surrounding stent

1 – scattered, noncircumferential lymphohistiocytic aggregates

2 – focal, noncircumferential lymphohistiocytic aggregates or scattered neutrophils and/or eosinophils.

3 – multifocal, noncircumferential lymphohistiocytic, neutrophilic and/or eosinophilic aggregates

4 – diffuse, circumferential lymphohistiocytic, neutrophilic and/or eosinophilic aggregates

---

[1] Provided by the Cardiovascular Pathology Laboratory at Texas A&M University.

[2] Modification from Schwartz et al. (92), Verheye et al. (93), and Kornowski et al. (94)

[3] Modification from Virmani and Farb (95), Farb et al. (96), and Kornowski et al. (94)

Results are expressed as: 0 = no inflammation; 1 = minimal inflammation; 2 = mild inflammation; 3 = moderate inflammation; and 4 = severe inflammation.

Residual Erythrocytes Score (Distribution)

0 – no erythrocytes surrounding stent

1 – scattered, noncircumferential erythrocytes

2 – focal, noncircumferential erythrocytes aggregates

3 – multifocal, noncircumferential erythrocytes aggregates

4 – diffuse, circumferential erythrocytes aggregates

Results are expressed as: 0 = no erythrocyte accumulation; 1 = minimal erythrocyte accumulation; 2 = mild erythrocyte accumulation; 3 = moderate erythrocyte accumulation; and 4 = severe erythrocyte accumulation.

Erythrocyte State Score

0 – no erythrocytes surrounding stent

1 – primarily erythrocytes (discoid morphology)

2 – admixture of erythrocytes (various stages of degeneration) and phagocytized erythrocytes

3 – primarily phagocytized erythrocytes/hemosiderin

4 – hemosiderin laden macrophages

Results are expressed as: 0 = no active or remote erythrocytes; 1 = active erythrocytes; 2 = mix (active and remote) erythrocytes; 3 = phagocytized erythrocytes/hemosiderin; 4 = residual hemosiderin in macrophages.

Vascular Score

0 – no revascularization within a 0.2 mm radius of the strut.

1 – 1, < 25 μm diameter neovascular bud within a 0.2 mm radius of the strut

2 – 2 to 3, < 25 μm diameter neovascular buds within a 0.2 mm radius of the strut

3 – 4 to 5, < 25 μm diameter neovascular buds within a 0.2 mm radius of the strut

4 – ≥ 6, < 25 μm diameter neovascular buds within a 0.2 mm radius of the strut

Results are expressed as: 0 = no revascularization; 1 = minimal neovascularization; 2 = mild neovascularization; 3 = moderate neovascularization; and 4 = severe neovascularization.

Fibrin Score

0 – no fibrin present

1 – deposition of fibrin in adjacent to the strut involving < 10% of the circumference of artery

2 – deposition involving > 10% but < 25% of the circumference of the artery or around stent struts

3 – deposition involving > 25% but < 50% of the circumference of the artery or around stent struts

4 – deposition involving > 50% of the circumference of the artery or around stent struts

Results are expressed as: 0 = no fibrin; 1 = minimal fibrin residual; 2 = mild fibrin residual; 3 = moderate fibrin residual; 4 = severe fibrin residual.

Multinucleated Giant Cells (MNGC) Score

0 – no MNGC present

1 – isolated or 1 cluster/syncytium of MNGC surrounding or adjacent to strut

2 – isolated or 2 clusters/syncytium of MNGC surrounding or adjacent to strut

3 – 3 to 4 clusters/syncytium of MNGC surrounding or adjacent to strut

4 – > 4 clusters/syncytium of MNGC cells surrounding or adjacent to strut

Results are expressed as: 0 = no MNGC present; 1 = minimal MNGC present; 2 = mild MNGC present; 3 = moderate MNGC present; 4 = severe MNGC present.

VITA

Name:	Lucas Howard Timmins
Address:	337 Zachry Engineering Center College Station, TX 77843-3120
Email Address:	lucas-howard-timmins@tamu.edu
Education:	B.S., Biomedical Engineering, Texas A&M University, 2005 Ph.D., Biomedical Engineering, Texas A&M University, 2010